Doctoral Dissertation

Studies on the Ground- and Excited-State Properties of Radical Ions Using Pulse Radiolysis and Laser Flash Photolysis

(パルスラジオリシスとレーザーフラッシュフォトリシス
を用いたラジカルイオンの基底及び
励起状態特性に関する研究)

魯　超 / **LU CHAO**

January 2017

Graduate School of Engineering,
Osaka University

Preface

The studies presented in this dissertation were carried out under the guidance of Professor Tetsuro Majima, Molecular Chemistry Course, Department of Applied Chemistry, Graduate School of Engineering, Osaka University during April 2014 to March 2017.

The object of this dissertation is the studies on the ground- and excited-state properties of radical anions and cations using nanosecond pulse radiolysis and femtosecond laser flash photolysis. The aim of this research is to systematically investigate the novel characteristics and detailed mechanisms of the intermolecular charge recombination and intramolecular electron (or hole) transfer processes initiated by the ground- and excited-state radical ions. The author hopes that the results and conclusions presented in this dissertation contribute to the further understanding for the unique charge transfer behaviors of both n-type and p-type organic semiconductors in various molecular devices.

Chao Lu

Department of Applied Chemistry
Graduate School of Engineering
Osaka University
2017

Contents

General Introduction……1

Chapter 1. Emission from Charge Recombination during the Pulse Radiolysis of Bis(diaryl-amino)dihydro-indenoindene Derivatives……...5

Chapter 2. Intramolecular Electron Transfer from Excited Aromatic Diimide Radical Anion:

Chapter 2-1. Unprecedented Intramolecular Electron Transfer from Excited Perylenediimide Radical Anion…..…….…….23

Chapter 2-2. Dual Character of Excited Radical Anions in Aromatic Diimide Bis(Radical Anion)s…..……..…….……..49

Chapter 3. Photo-Accelerated Hole Transfer in Oligothiophene Assemblies…….…….69

General Conclusion……..95

List of Publications……..97

Acknowledgements……..99

General Introduction

Radical ions generated by the single electron transfer (ET) mechanisms are considered as the important ionic intermediates in photochemistry, electrochemistry, biochemistry, and radiation chemistry, etc.[1] In particular, photo-induced ET, electrochemical ET, chemical redox reaction, and radiolysis processes accompanied with the one-electron reduction and oxidation lead to the formation of radical anion and cation, respectively (Scheme 1a). The typical molecular orbital patterns described for a neutral molecule and its corresponding radical ions are shown in Scheme 1b. The ET step takes place from an electron donor to the lowest unoccupied molecular orbital (LUMO) of a neutral molecule or from the highest occupied molecular orbital (HOMO) of a neutral molecule to an electron acceptor gives the product as radical anion or cation, respectively. Thus, the HOMO (also called singly occupied molecular orbital, SOMO) and HOMO−1 of a radical anion, or the LUMO and SOMO of a radical cation correspond to the LUMO and HOMO of its neutral state, respectively.

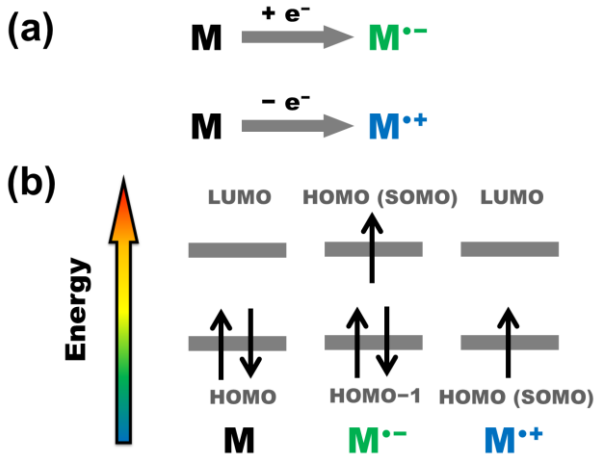

Scheme 1. (a) Generation of radical anion ($M^{\bullet-}$) and cation ($M^{\bullet+}$) from a neutral molecule (M). (b) Molecular orbital patterns for M, $M^{\bullet-}$, and $M^{\bullet+}$.

One of the famous phenomena originated from the unique behaviors of ground-state radical ions is well known as electrochemiluminescence, or electrogenerated chemiluminescence

(ECL).[2,3] A general mechanism of ECL is outlined in Scheme 2. Typically, ECL occurs when an alternate potential is applied to an electrode (e.g., Pt, Au, or glassy carbon), resulting in the radical anion upon cathodic reduction and the radical cation upon anodic oxidation. The electrogenerated radical anion and cation can then react with each other and undergo an annihilation process to obtain the excited state that is capable of emitting light. Various highly efficient ECL molecules have been explored due to their potential application in organic light-emitting diodes (OLEDs), which is one of the most innovative technologies for high-resolution flat panel displays.[4,5] However, the detailed mechanisms relating to the efficient and stable luminescence especially for the newly-designed OLED materials are still not clear due to lack of proper analytical methods.

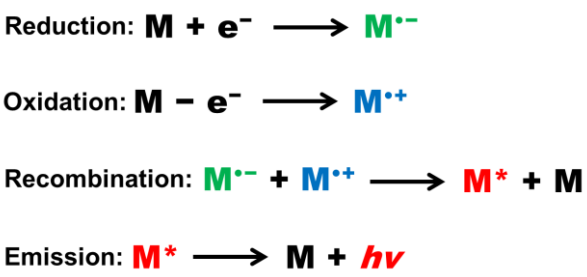

Scheme 2. A general mechanism of ECL (M* represents the excited state of a neutral molecule).

On the other hand, excitation of radical anion and cation by photoirradiation generates excited radical anion and cation, respectively (Scheme 3a).[6,7] Typically, a HOMO−1 → HOMO transition can be expected in the molecular orbitals of a radical ion upon excitation, as shown in Scheme 3b. Radical ions in the excited states are highly reactive intermediates because of their redox reactivity.[8,9] This viewpoint can be elucidated on the basis of the schematic diagram shown in Scheme 4. Ground-state radical anion or cation produced by one-electron reduction or oxidation is generally treated as an electron or hole acceptor. However, excited radial anion or cation, which has a more negative or positive redox potential, is applicable to be a powerful electron or hole donor. Thus, excitation of radical ions should be an attractive process because of its leading to a variety of reactions that are unrealizable from the corresponding ground-states. Furthermore, when considering the roles of charge carriers upon irradiation in n-type or p-type organic semiconductors, the information on excited radical anions and cations is of great importance. In spite of this, the studies on the detailed characteristics (e.g., driving force and

distance dependences, etc) of the ET or hole transfer (HT) processes from excited radical ions are still very limited.

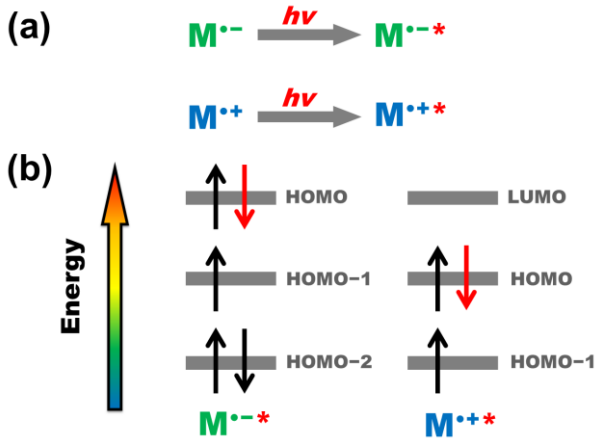

Scheme 3. (a) Generation of excited radical anion ($M^{\bullet-}$*) and cation ($M^{\bullet+}$*) from $M^{\bullet-}$ and $M^{\bullet+}$, respectively. (b) Molecular orbital patterns for $M^{\bullet-}$* and $M^{\bullet+}$*.

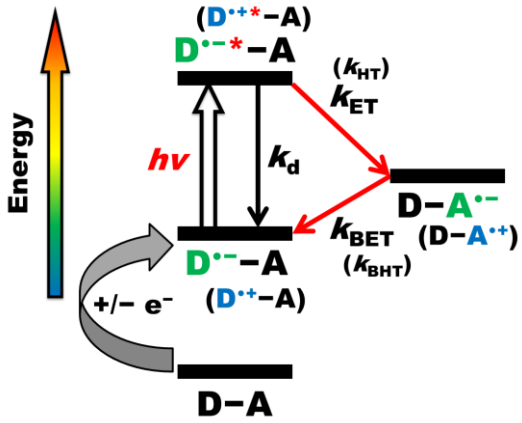

Scheme 4. Schematic diagram for ET and HT from excited radical ions (D and A represent donor and acceptor, respectively; k_d, k_{ET}, k_{BET}, k_{HT}, and k_{BHT} represent rate constants of deactivation, ET, back ET, HT, and back HT processes, respectively).

Thus, in this dissertation, the author aimed to investigate the unique properties of ground- and excited-state radical anions and cations using time-resolved spectroscopies. The contents of this dissertation include two main aspects: (1) study on the intermolecular charge recombination between the ground-state radical anion and cation using nanosecond pulse radiolysis (Chapter 1),

and (2) study on the intramolecular ET or HT initiated by the excited-state radical anion or cation using femtosecond laser flash photolysis (Chapters 2 and 3). Introduction for each chapter is shown as follows:

In Chapter 1, bis(diarylamino)dihydro-indenoindene derivatives (R-DI), a new series of candidate molecules for OLED application, were investigated by nanosecond pulse radiolysis to clarify their emission mechanism relating to the charge recombination of ground-state radical cations and anions ($R\text{-}DI^{\bullet+}$ and $R\text{-}DI^{\bullet-}$).

In Chapter 2-1, the intramolecular ET processes from excited perylenediimide radical anion ($PDI^{\bullet-}$*) were examined for the first time by applying femtosecond laser flash photolysis to the reduced dyads of PDI and acceptors. In Chapter 2-2, the intramolecular ET processes in the excited aromatic diimide bis(radical anion)s ($ADI^{\bullet-}$*-$ADI'^{\bullet-}$) were investigated by applying femtosecond laser flash photolysis to bis(radical anion)s of naphthalenediimide (NDI) and PDI.

In Chapter 3, a new series of mesitylene-linked oligothiophenes (*n*T, *n* is the number of thiophene units), including 2T-M, 3T-M, 4T-M, 4T-M-2T, and 4T-M-3T, was prepared as the target molecules. By applying femtosecond laser flash photolysis to the charged *n*T assemblies, the intramolecular HT from excited radical cation ($4T^{\bullet+}$*) was investigated for the first time.

References

(1) Zhang, N.; Samanta, S. R.; Rosen, B. M.; Percec, V. *Chem. Rev.* **2014**, *114*, 5848.

(2) Richter, M. M. *Chem. Rev.* **2004**, *104*, 3003.

(3) Hu, L.; Xu, G. *Chem. Soc. Rev.* **2010**, *39*, 3275.

(4) Shen, Z.; Burrows, P. E.; Bulovic, V.; Forrest, S. R.; Thompson, M. E. *Science* **1997**, *276*, 2009.

(5) Burn, P. L.; Lo, S. C.; Samuel, I. D. W. *Adv. Mater.* **2007**, *19*, 1675.

(6) Shukla, S. S.; Rusling, J. F. *J. Phys. Chem.* **1985**, *89*, 3353.

(7) Shine, H. J.; Zhao, D. C. *J. Org. Chem.* **1990**, *55*, 4086.

(8) Debreczeny, M. P.; Svec, W. A.; Marsh, E. M.; Wasielewski, M. R. *J. Am. Chem. Soc.* **1996**, *118*, 8174.

(9) Samori, S.; Fujitsuka, M.; Majima, T. *J. Phys. Chem. A* **2008**, *112*, 11312.

Chapter 1. Emission from Charge Recombination during the Pulse Radiolysis of Bis(diarylamino)dihydro-indenoindene Derivatives

Abstract

As a new series of compounds designed for organic light-emitting diodes (OLEDs), dihydro-indenoindenes (DI) substituted by bis(diarylamino) groups (R-DI) including bis(diphenylamino) DI, bis(ditolylamino)DI, and bis(carbazolyl)DI were studied during the nanosecond pulse radiolysis in solvents to measure the transient absorptions of the corresponding radical cations ($R\text{-}DI^{\bullet+}$), radical anions ($R\text{-}DI^{\bullet-}$), and R-DI in the triplet excited states (^{3}R-DI*). The observed spectra and theoretical calculations suggested that the positive charge is mainly localized on the triphenylamine moiety of $R\text{-}DI^{\bullet+}$, whereas the negative charge is localized on the *trans*-stilbene moiety of $R\text{-}DI^{\bullet-}$. All R-DI showed emission during the pulse radiolysis in benzene. It was found that the fluorescence quantum yields and the difference between annihilation enthalpy changes and singlet excited state energies are responsible for the relative emission intensity obtained during the pulse radiolysis. Moreover, based on the observed spectra and thermodynamic calculations, the emission was suggested to be originated from R-DI in the singlet excited states (^{1}R-DI*), which were directly generated from the charge recombination between the ground-state $R\text{-}DI^{\bullet+}$ and $R\text{-}DI^{\bullet-}$.

Introduction

One-electron oxidation and reduction of organic compounds often occur to give the ground-state radical cations and anions, respectively. Investigation of these radical ions is very important in the fundamental research of chemistry, physics, biology, and material science regarding their application. One of them is the well-known electrochemiluminescence or electrogenerated chemiluminescence in which the charge recombination between radical cations and anions generated in the electrolysis of organic compounds occurs to give emission from the excited states.[1-3] The similar mechanism is also found in organic light-emitting diodes (OLEDs), which are considered to have potential application in the next generation flat panel displays because of their broad operating temperature, simple preparation process, low power consumption, thin thickness, light weight, and high color tunability.[4-7]

Typically, OLEDs are composed of electrodes, charge transporting layers, and high emissive R-Y-G-B (red, yellow, green, blue) layers made by organic compounds. Since molecular architecture plays an essential role in OLED materials, many novel organic molecules exhibiting various colors have been designed and synthesized as emitting materials.[8-11] Among them, bis(diarylamino)stilbenes are well known as blue fluorescent materials.[12-14] However, their photo-induced *trans* to *cis* isomerization and interchromophoric contact make the limit of further application to OLEDs, because such properties significantly reduce the emission efficiency.[15,16] In previous works, several *ortho*-linked *cis*-4,4′-bis(diarylamino)stilbenes have been studied.[17] These compounds have a rigid spiral framework, which hinders the intermolecular chromophoric π-π stacking and excimer formation, increasing the thermal stability as evident from the higher glassy transition temperature.[18]

Recently, as another potential candidate for OLEDs, bis(diarylamino)dihydro-indenoindene derivatives (R-DI) with two diarylamino substituents at the 2- and 7- positions of 5,5,10,10-tetraphenyl-5,10-dihydro-[2,1,*a*]-indenoindene (DI) caught researchers' attention because they have a constrained *trans*-stilbene moiety as their core structure.[19-21] R-DI have the highest occupied molecular orbital (HOMO) energies close to the work function of indium tin oxide (ITO), leading to the efficient hole injection and higher hole density. Thus, they have been considered as hole-transporting materials to enhance the electroluminescent brightness and working efficiency of relevant OLEDs.[22] However, the emission mechanism of R-DI is still not

clear due to lack of proper analytical investigation.

It has been established that radical cations of aromatic compounds are selectively produced during the pulse radiolysis in 1,2-dichloroethane (DCE), while radical anions are generated during the pulse radiolysis in *N*,*N*-dimethylformamide (DMF). Moreover, almost coinstantaneous formation of radical cations and anions originated from solute molecules was confirmed during the pulse radiolysis in benzene (Bz).[23,24] Here, DI derivatives substituted by three kinds of diarylamino groups including bis(diphenylamino)DI (P-DI), bis(ditolylamino)DI (T-DI), and bis(carbazolyl)DI (C-DI) were chosen for the systematic study using nanosecond pulse radiolysis to clarify the emission mechanism of these new OLED materials (Scheme 1-1).

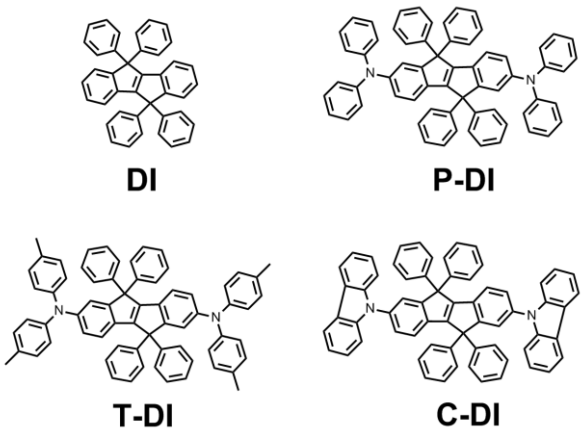

Scheme 1-1. Chemical structures of DI, P-DI, T-DI, and C-DI.

Experimental Section

Materials. DI and R-DI were prepared as described in the previous paper.[19] In the present study, DCE, DMF, and Bz were used as solvents for spectroscopic measurements.

Steady-State Spectral Measurements. UV-vis spectra and fluorescence spectra of DI and R-DI were measured in Bz with a Shimadzu UV-3600 UV-vis-NIR spectrometer and Horiba FluoroMax-4 spectrofluorometer, respectively.

Fluorescence Decay Profiles. The fluorescence decay profiles of DI and R-DI were measured

by the single photon counting method using a streak camera.[25] The ultrashort laser pulse was generated by a Ti:sapphire laser (Spectra-Physics, Tsunami 3941-M1BB). For excitation of the samples, the output of the Ti:sapphire laser was converted to the second harmonic oscillation (360 nm) using a type 1 BBO crystal.

Pulse Radiolysis Measurements. Pulse radiolysis experiments were carried out by using an electron pulse (28 MeV, 8 ns fwhm, 0.3 kGy per pulse) from a linear accelerator at Osaka University. The probe light from a 450 W Xe-lamp (Ushio, UXL-451-0) was detected with a multichannel spectrometer (UNISOKU, TSP-1000) or a photomultiplier (Hamamatsu Photonics, R2949) connected to a digital oscilloscope (Tektronix, TDS580D).

Theoretical Calculations. Optimized structures of the radical ions of molecules in the present study were estimated by using density functional theory (DFT) at the (U)B3LYP/6-31G(d) level. All theoretical calculations were carried out using the Gaussian 09 package.[26] It was confirmed that the estimated structures did not exhibit imaginary frequency.

Results and Discussion

Steady-State Spectral Measurements of DI and R-DI

Figure 1-1 shows the UV-vis absorption and fluorescence spectra of DI and R-DI in Ar-saturated Bz. In general, the observed absorption maxima ($\lambda^{Abs.}_{max}$) of the neutral DI and R-DI are in the range of 336-410 nm, while the fluorescence maxima ($\lambda^{Fl.}_{max}$) with nanosecond lifetimes are in the range of 385-455 nm (Table 1-1). It is notable that both the absorption and fluorescence peaks of R-DI were found to shift to the longer wavelengths in the order of C-DI, P-DI, and T-DI, which is consistent with increasing electron-donating character of diarylamino substituents at the 2- and 7- positions of the DI moiety.[19]

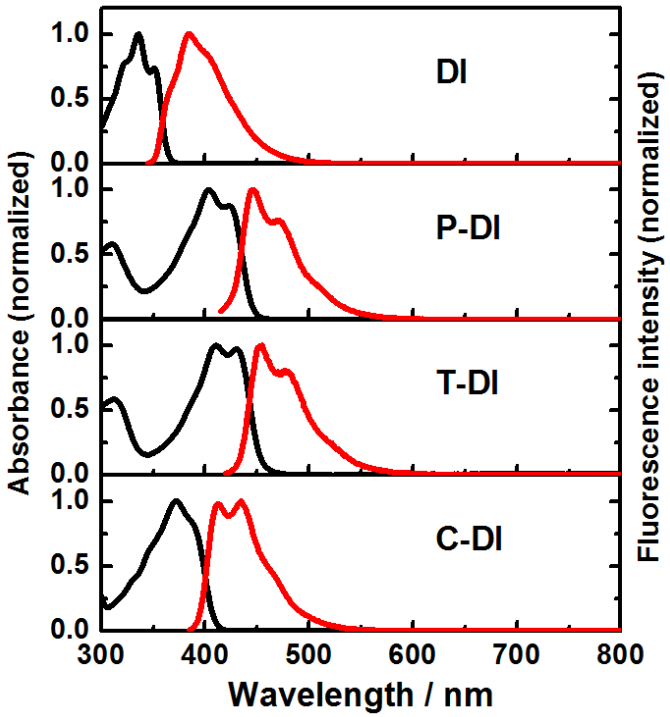

Figure 1-1. Normalized absorption (black line) and fluorescence (red line) spectra of DI and R-DI in Ar-saturated Bz.

Table 1-1. Absorption Maxima ($\lambda^{Abs.}_{max}$), Fluorescence Maxima ($\lambda^{Fl.}_{max}$), and Fluorescence Lifetimes ($\tau_{Fl.}$) of DI and R-DI in Ar-Saturated Bz.

	$\lambda^{Abs.}_{max}$ (nm)	$\lambda^{Fl.}_{max}$ (nm)	$\tau_{Fl.}$ (ns)
DI	336	385	1.9
P-DI	404	447	2.4
T-DI	410	455	2.2
C-DI	372	435	1.9

Transient Absorption Spectra Observed during the Pulse Radiolysis of DI and R-DI

Figure 1-2 shows the transient absorption spectra observed during the pulse radiolysis of DI and R-DI in Ar-saturated DCE. Transient absorption of T-DI was not obtained because of the poor solubility. The peaks observed in the range of 473-640 nm with microsecond half-lifetimes ($\tau_{1/2}$ = 10.9-30.6 μs) are assigned to the radical cations ($DI^{\bullet+}$, $P\text{-}DI^{\bullet+}$, and $C\text{-}DI^{\bullet+}$) (Table 1-2). It

is worth noting that for $DI^{\bullet+}$, the absorption peak was observed at 473 nm, while P-$DI^{\bullet+}$ and C-$DI^{\bullet+}$ showed a broader absorption band in the range of 450-750 nm and 400-700 nm, respectively. Since DI has a constrained *trans*-stilbene in its core, it is expected that $DI^{\bullet+}$ has an absorption peak at around 470 nm similar to that of *trans*-stilbene radical cation,[27] which was clearly observed in the present study. On the other hand, the spectrum of P-$DI^{\bullet+}$ is close to that of triphenylamine radical cation ($TPA^{\bullet+}$), which has a broad band with a maximum at around 650 nm.[28] Moreover, the absorption peaks of P-$DI^{\bullet+}$ and C-$DI^{\bullet+}$ shifted to the longer wavelengths than those of *trans*-stilbene radical cation and $DI^{\bullet+}$ with increasing electron-donating character of diarylamino substituents. Such shift and similar broad bands of P-$DI^{\bullet+}$ and C-$DI^{\bullet+}$ suggested that the positive charge is mainly localized on the TPA moiety of R-$DI^{\bullet+}$.

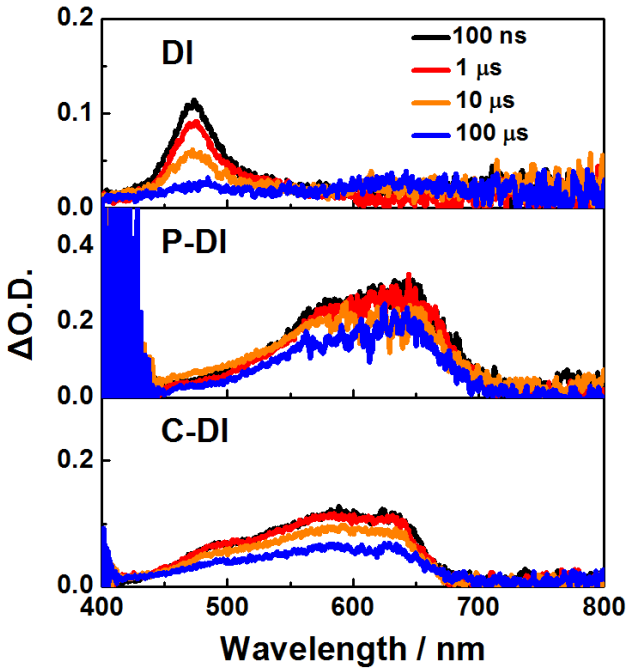

Figure 1-2. Transient absorption spectra observed at t = 100 ns, 1, 10, and 100 μs after an electron pulse during the pulse radiolysis of DI and R-DI (1 mM) in Ar-saturated DCE. No spectra for T-DI because of the poor solubility.

Table 1-2. Transient Absorption Maxima (λ^{TA}_{max}) and Half-Lifetimes ($\tau_{1/2}$) Observed during the Pulse Radiolysis of DI and R-DI in Ar-Saturated DCE, DMF, and Bz.

	in DCE		in DMF		in Bz	
	λ^{TA}_{max} (nm)	$\tau_{1/2}$ (μs)	λ^{TA}_{max} (nm)	$\tau_{1/2}$ (μs)	λ^{TA}_{max} (nm)	$\tau_{1/2}$ (μs)
DI	473	10.9	503	6.8	480	4.6
P-DI	640	30.6	545	5.5	580	3.1
T-DI	-[a]	-[a]	-[a]	-[a]	600	4.3
C-DI	590	13.4	533	12.2	550	10.3

[a]Not obtained.

Figure 1-3 shows the transient absorption spectra observed during the pulse radiolysis of DI and R-DI in Ar-saturated DMF. Here too, T-DI did not give the transient absorption because of the poor solubility. The peaks observed in the range of 503-545 nm with microsecond half-lifetimes ($\tau_{1/2}$ = 5.5-12.2 μs) are assigned to the radical anions ($DI^{\bullet-}$, $P\text{-}DI^{\bullet-}$, and $C\text{-}DI^{\bullet-}$) (Table 1-2). The transient absorption spectrum with a peak at around 500 nm has been assigned to *trans*-stilbene radical anion,[29] which is consistent with that of $DI^{\bullet-}$ obtained here. In the case of radical anion, the changes of peak shape and shift due to the diarylamino substituents were rather small. The absorption peaks of $P\text{-}DI^{\bullet-}$ and $C\text{-}DI^{\bullet-}$ shifted to the longer wavelengths by nearly 30-45 nm with increasing electron-donating character of diarylamino groups, indicating that the negative charge is mainly localized on the *trans*-stilbene moiety of $R\text{-}DI^{\bullet-}$.

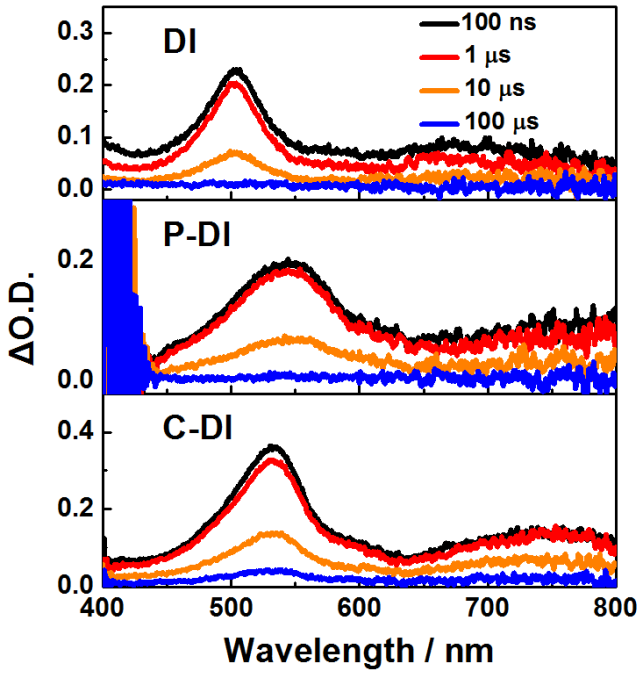

Figure 1-3. Transient absorption spectra observed at t = 100 ns, 1, 10, and 100 μs after an electron pulse during the pulse radiolysis of DI and R-DI (1 mM) in Ar-saturated DMF. No spectra for T-DI because of the poor solubility.

Figure 1-4 shows the transient absorption spectra observed during the pulse radiolysis of DI and R-DI in Ar-saturated Bz. The absorption peaks in the range of 480-600 nm observed immediately after an electron pulse with microsecond half-lifetimes ($\tau_{1/2}$ = 3.1-10.3 μs) are assigned to DI and R-DI in the triplet excited states (^{3}DI* and ^{3}R-DI*) generated from the charge recombination between the corresponding radical cations and radical anions (Table 1-2). The peak position of the triplet-triplet absorption spectrum of *trans*-stilbene during the pulse radiolysis was reported to be 480 nm,[30] which is similar to that of ^{3}DI* obtained here. Additionally, the absorption peaks of ^{3}R-DI* shifted to the longer wavelengths in the order of ^{3}C-DI*, ^{3}P-DI*, and ^{3}T-DI*, which is in agreement with increasing electron-donating character of diarylamino substituents.

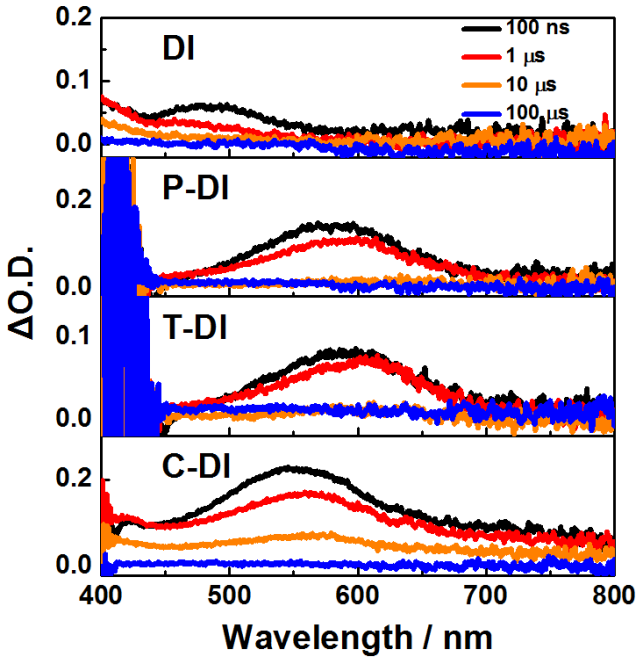

Figure 1-4. Transient absorption spectra observed at t = 100 ns, 1, 10, and 100 μs after an electron pulse during the pulse radiolysis of DI and R-DI (1 mM) in Ar-saturated Bz.

Moreover, in order to obtain the further understanding for the observed transient spectra, the DFT calculations were carried out to estimate the spin density distribution in the radical cations and anions of DI and R-DI. Generally, the spin density distribution reflects the difference between the total α-spin (spin up) and β-spin (spin down) distributions and often leads to positive accumulating in regions where the singly occupied molecular orbital (SOMO) α-spin electron has the major contribution.[31] Therefore, the spatial distribution of the unpaired electron in the open-shell radical ions can be numerically estimated. The results of the calculations are shown in Figure 1-5, in which the major contributions are marked in red. It was found that $DI^{\bullet+}$ and $DI^{\bullet-}$ have the spin density distribution mainly on their *trans*-stilbene skeleton of DI (Figure 1-5a). On the other hand, $P\text{-}DI^{\bullet+}$ has the spin density distribution mainly on the nitrogen atoms of diarylamino substituents, whereas $P\text{-}DI^{\bullet-}$ has the spin density distribution on its *trans*-stilbene moiety (Figure 1-5b). The spin density distribution patterns in the radical ions of T-DI and C-DI (Figures 1-5c,d) are similar to that of P-DI. The results of the theoretical calculations obtained here are in agreement with the observed transient absorption spectra during the pulse radiolysis measurements, supporting the suggestion about the charge localization in the radical ions of DI and R-DI.

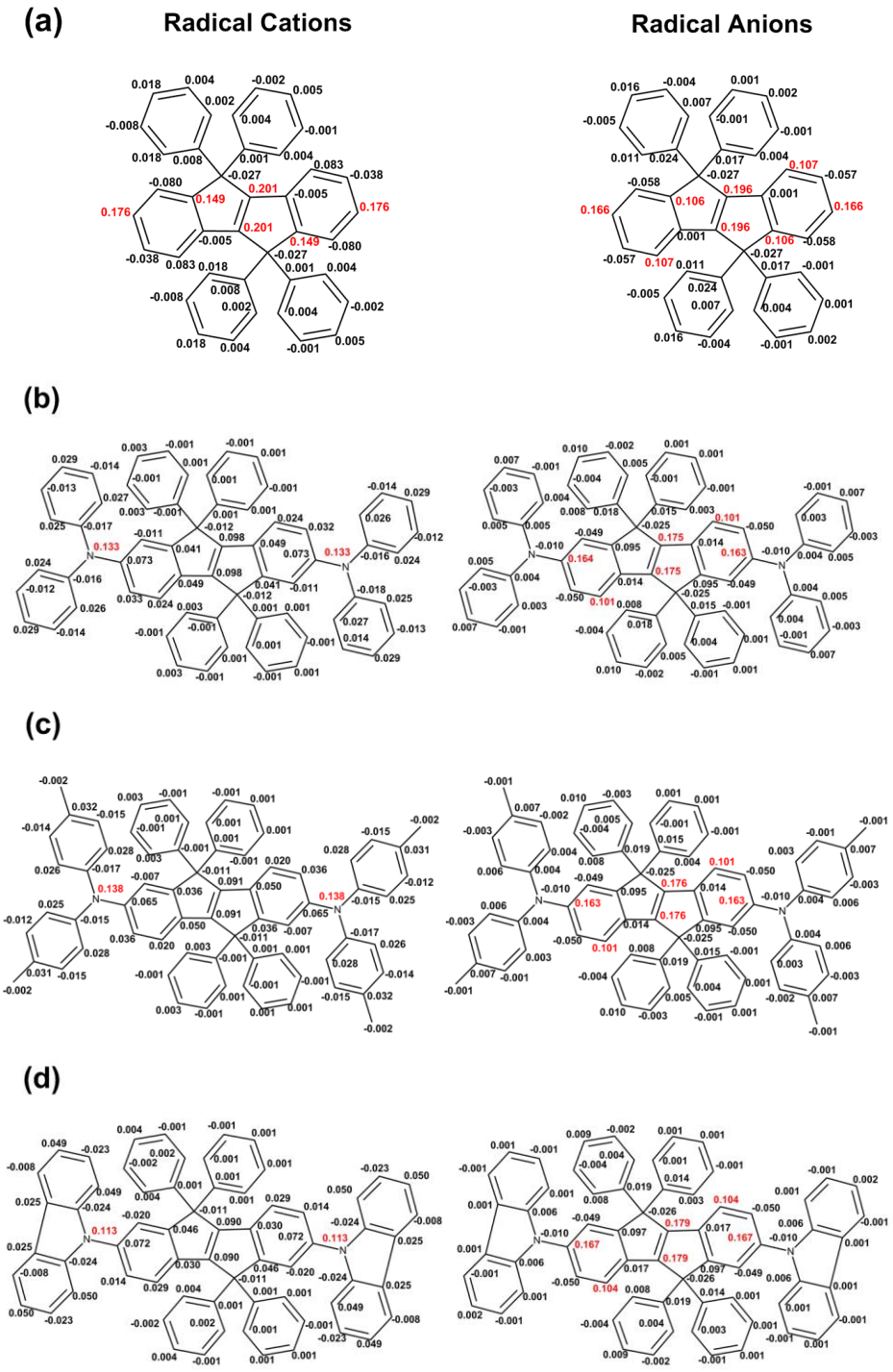

Figure 1-5. Spin density distribution in the radical cations (left) and anions (right) of (a) DI, (b) P-DI, (c) T-DI, and (d) C-DI calculated at the (U)B3LYP/6-31G(d) level. (The major contributions are marked in red.)

Emission Spectra Observed during the Pulse Radiolysis of R-DI in Bz

The time-resolved emission spectra of R-DI were taken after an electron pulse during the pulse radiolysis in Ar-saturated Bz (Figure 1-6). Notably, all these compounds showed emission peaks in the range of 435-457 nm with nanosecond lifetimes ($\tau_{Em.}$ = 11.6-20.6 ns) (Table 1-3). By employing C-DI as a standard (100), the relative emission intensity of P-DI and T-DI is 37 and 11, respectively.

It is worth mentioning that the relative emission intensity observed here is similar to the trend of the fluorescence quantum yields ($\Phi_{Fl.}$) reported in the previous literature,[19] suggesting that $\Phi_{Fl.}$ is one of the important factors determining the emission intensity of R-DI during the pulse radiolysis in Bz. On the other hand, the operational brightness (B) of R-DI observed in OLED devices does not consist with the current results.[19] It is due to the positive charge (hole) is more likely to be trapped by a higher hole injection barrier (HOMO) in solid OLED devices rather than in solutions, which decreases the charge recombination process.

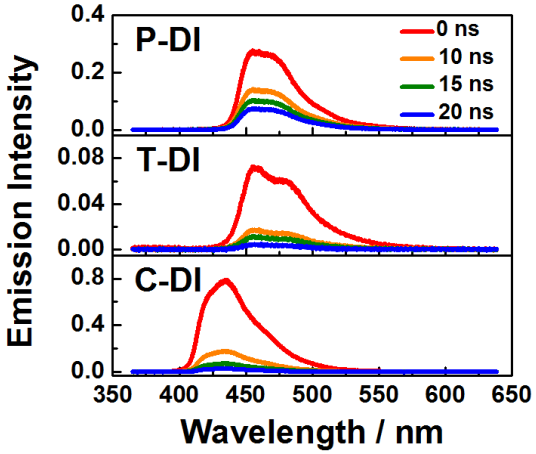

Figure 1-6. Emission spectra observed at t = 0, 10, 15, and 20 ns after an electron pulse during the pulse radiolysis of R-DI (1 mM) in Ar-saturated Bz.

Table 1-3. Emission Maxima ($\lambda^{Em.}_{max}$), Emission Lifetimes ($\tau_{Em.}$), and Relative Emission Intensity (Em.int.$^{rel.}$) of R-DI Observed during the Pulse Radiolysis in Ar-Saturated Bz, Together

with Their Fluorescence Quantum Yields ($\Phi_{Fl.}$), HOMO Energy Levels, and Operational Brightness (B) as OLED Materials.

	$\lambda^{Em.}_{max}$ (nm)	$\tau_{Em.}$ (ns)	Em.int.$^{rel.}$ (%)	$\Phi_{Fl.}{}^{19}$	HOMO (eV)	B^{19} (cd m^{-2})
P-DI	456	20.6	37	0.49	5.01	551
T-DI	457	14.2	11	0.47	4.79	563
C-DI	435	11.6	100	0.80	5.49	347

Annihilation Enthalpy Evaluation and Emission Mechanism

The change of annihilation enthalpy ($-\Delta H°$) for the charge recombination between a given radical cation and anion provides an important insight to understand the nature of excited-state compounds responsible for the observed emission. Here $-\Delta H°$ can be calculated according to the following equation (eq 1-1):

$$-\Delta H° = \Delta E^{\varepsilon_s} - \Delta G_{sol}{}^{\varepsilon_s} - w_{a,u} + T\Delta S° \quad (1\text{-}1)$$

where ΔE represents the difference between the oxidation and reduction potentials of solute molecule. ε_s, ΔG_{sol}, and $w_{a,u}$ represent the static dielectric constant of solvent, the free energy change of solvation, and the work required to bring the radical cation and anion within a possible separation distance, respectively. In Bz, the expression for $-\Delta H°$ can be simplified as eq 1-2:

$$-\Delta H° = E_{ox} - E_{red} + 0.13 \text{ eV} \quad (1\text{-}2)$$

where E_{ox} and E_{red} are the oxidation and reduction potentials, respectively. The $-\Delta H°$ values for R-DI in Bz are shown in Table 1-4 with their singlet excited state energies (E_{S_1}) calculated from the emission maxima obtained during the pulse radiolysis.

Table 1-4. Annihilation Enthalpy Changes ($-\Delta H°$) and Singlet Excited State Energies (E_{S_1}) for R-DI.

	$-\Delta H^\circ$(eV)	E_{S_1} (eV)	$-\Delta H^\circ - E_{S_1}$ (eV)
P-DI	2.88	2.72	0.16
T-DI	2.83	2.71	0.12
C-DI	3.12	2.85	0.27

It is a remarkable fact that $-\Delta H^\circ$ for all R-DI is larger than E_{S_1}, suggesting that the energy available from the charge recombination process is sufficient to generate R-DI in the excited singlet states (^{1}R-DI*). Therefore, the short-lived emission species observed during the pulse radiolysis of R-DI in Bz can be assigned to ^{1}R-DI*. In addition, the energy difference between $-\Delta H^\circ$ and E_{S_1} (from 0.27 eV to 0.12 eV) is in the order of C-DI > P-DI > T-DI, which agrees with the relative emission intensity during the pulse radiolysis, indicating that the difference between $-\Delta H^\circ$ and E_{S_1} also can be considered as another important factor determining the emission intensity.

During the pulse radiolysis of R-DI in DCE or DMF there was no or little observed emission, which implies that R-DI$^{\bullet+}$ or R-DI$^{\bullet-}$ do not emit themselves. That is, both R-DI$^{\bullet+}$ and R-DI$^{\bullet-}$ must be formed simultaneously to realize the emission. No transient absorption spectra of R-DI$^{\bullet+}$ or R-DI$^{\bullet-}$ were detected in Bz after an electron pulse, suggesting that R-DI$^{\bullet+}$ and R-DI$^{\bullet-}$ tend to recombine immediately and give ^{1}R-DI* or ^{3}R-DI*. Thus, the pulse radiolysis-induced emission mechanism of R-DI in Ar-saturated Bz can be summarized in Scheme 1-2. In the initial step, the radiolysis of solvent causes the generation of its radical cation (Bz$^{\bullet+}$) and e$^-$. After that, R-DI$^{\bullet+}$ and R-DI$^{\bullet-}$ are produced by reacting of solute molecules with the generated Bz$^{\bullet+}$ and e$^-$, respectively. Then, the charge recombination between R-DI$^{\bullet+}$ and R-DI$^{\bullet-}$ occurs to give ^{1}R-DI* or ^{3}R-DI*. In which, ^{1}R-DI* relax to the ground states with release of emission (S-route). Moreover, since the energy for the charge recombination is sufficient to directly give ^{1}R-DI* and no any delayed emission was detected during the pulse radiolysis, the possibility of emission caused by triplet-triplet annihilation (T-route) can be ruled out in this mechanism.

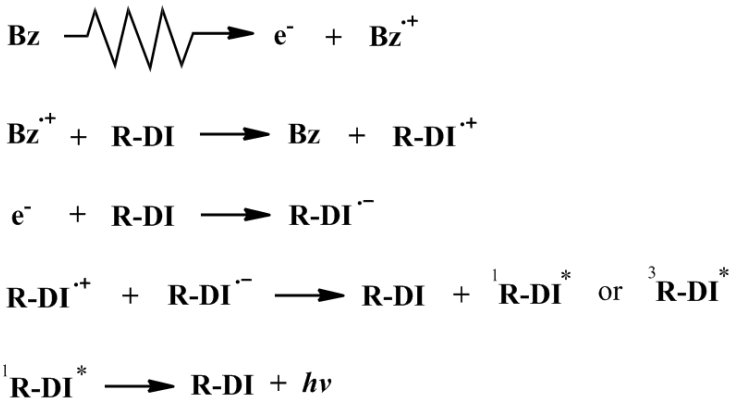

Scheme 1-2. Emission mechanism during the pulse radiolysis of R-DI in Bz.

Moreover, in order to give a detailed elaboration for the charge recombination process proposed above, it is also important to know how the positive and negative charges sustain in the radical ions. Based on the observed transient spectra and theoretical calculations of the spin density distribution in R-DI$^{\bullet+}$ and R-DI$^{\bullet-}$, the positive charge was suggested to be localized on the corresponding TPA moiety (electron acceptor), while the negative charge is localized on the *trans*-stilbene moiety (electron donor). Therefore, the charge recombination between ground-state R-DI$^{\bullet+}$ and R-DI$^{\bullet-}$ through the intermolecular electron transfer (Scheme 1-3) was suggested to occur during the pulse radiolysis in Bz.

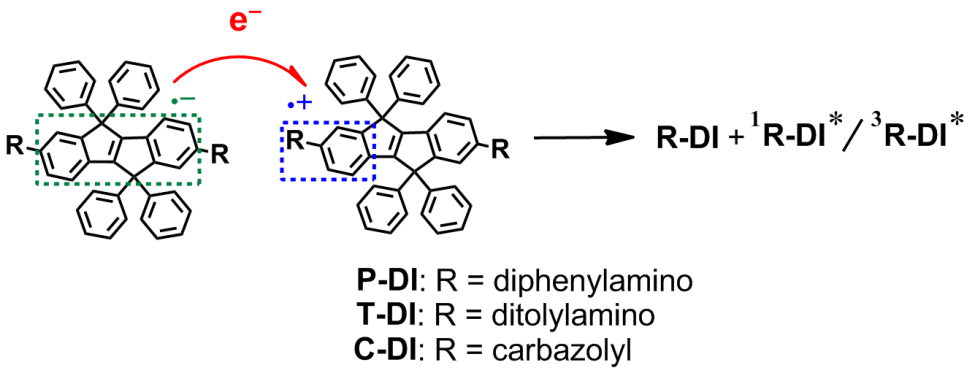

Scheme 1-3. Charge recombination mechanism proposed for R-DI through the intermolecular electron transfer from the radical anion moieties to the radical cation moieties.

As the OLED materials, R-DI discussed here have higher emission efficiency when compared

with the bare stilbene and indenoindene derivatives. The latter showed low fluorescence quantum yields of less than 20%.[32,33] According to the discussion above, several reasons can be considered. Firstly, R-DI have the diarylamino groups and *trans*-stilbene moiety to localize the corresponding radical cations and anions, respectively, which is desirable for the intermolecular electron transfer, leading to the efficient charge recombination.[34] Secondly, with the addition of the perpendicular butterfly-shaped phenyl groups, R-DI have a more bulky structure, leading to the higher thermal stability and emission efficiency.[35] Thirdly, the $\tau_{1/2}$ of each R-DI$^{\bullet+}$ is longer than that of the corresponding R-DI$^{\bullet-}$, which implies all R-DI$^{\bullet+}$ have a slower neutralization process. This phenomenon is beneficial for the hole transport in OLED materials. Furthermore, when compared to the other emissive organic compounds studied by the pulse radiolysis,[23,36-38] the molecular design, especially the non-planar frameworks of R-DI, extremely reduces the possibility of the π-π interaction and excimer formation, resulting in the non-delayed emission.

Conclusions

Three R-DI were investigated by the nanosecond pulse radiolysis to observe the absorption spectra of their corresponding R-DI$^{\bullet+}$, R-DI$^{\bullet-}$, and ^{3}R-DI*. The current results clearly showed that the absorption peaks of R-DI$^{\bullet+}$, R-DI$^{\bullet-}$, and ^{3}R-DI* were red-shifted with increasing electron-donating character of diarylamino groups. Based on the observed spectra and theoretical calculations, it was suggested that the positive charge is mainly localized on the TPA moiety of R-DI$^{\bullet+}$, whereas the negative charge is localized on the *trans*-stilbene moiety of R-DI$^{\bullet-}$. All R-DI showed emission with nanosecond lifetimes during the pulse radiolysis in Bz. It is worth mentioning that the $\Phi_{\mathrm{Fl.}}$ and $(-\Delta H^{\circ} - E_{S_1})$ of R-DI were found to be the important factors determining the relative emission intensity. In addition, the non-delayed emission observed during the pulse radiolysis was considered to be derived from direct ^{1}R-DI* generation by the charge recombination between the ground-state R-DI$^{\bullet+}$ and R-DI$^{\bullet-}$. The emission mechanism provided valuable insights for developing R-DI as potential candidates for OLEDs.

References

(1) Lee, S. K.; Zu, Y.; Herrmann, A.; Geerts, Y.; Müllen, K.; Bard, A. J. *J. Am. Chem. Soc.* **1999**, *121*, 3513.

(2) Richter, M. M. *Chem. Rev.* **2004**, *104*, 3003.

(3) Hu, L.; Xu, G. *Chem. Soc. Rev.* **2010**, *39*, 3275.

(4) Sheats, J. R.; Antoniadis, H.; Hueschen, M.; Leonard, W.; Miller, J.; Moon, R.; Roitman, D.; Stocking, A. *Science* **1996**, *273*, 884.

(5) Shen, Z.; Burrows, P. E.; Bulovic, V.; Forrest, S. R.; Thompson, M. E. *Science* **1997**, *276*, 2009.

(6) Burn, P. L.; Lo, S. C.; Samuel, I. D. W. *Adv. Mater.* **2007**, *19*, 1675.

(7) Kamtekar, K. T.; Monkman, A. P.; Bryce, M. R. 2010; Vol. 22, p 572.

(8) Mitschke, U.; Bäuerle, P. *J. Mater. Chem.* **2000**, *10*, 1471.

(9) Hung, L. S.; Chen, C. H. *Mater. Sci. Eng., R* **2002**, *39*, 143.

(10) White, M. S.; Kaltenbrunner, M.; Głowacki, E. D.; Gutnichenko, K.; Kettlgruber, G.; Graz, I.; Aazou, S.; Ulbricht, C.; Egbe, D. A. M.; Miron, M. C.; Major, Z.; Scharber, M. C.; Sekitani, T.; Someya, T.; Bauer, S.; Sariciftci, N. S. *Nat. Photonics* **2013**, *7*, 811.

(11) Sun, N.; Wang, Q.; Zhao, Y.; Chen, Y.; Yang, D.; Zhao, F.; Chen, J.; Ma, D. *Adv. Mater.* **2014**, *26*, 1617.

(12) Rumi, M.; Ehrlich, J. E.; Heikal, A. A.; Perry, J. W.; Barlow, S.; Hu, Z.; McCord-Maughon, D.; Parker, T. C.; Röckel, H.; Thayumanavan, S.; Marder, S. R.; Beljonne, D.; Brédas, J. *J. Am. Chem. Soc.* **2000**, *122*, 9500.

(13) Sigalov, M.; Ben-Asuly, A.; Shapiro, L.; Ellern, A.; Khodorkovsky, V. *Tetrahedron Lett.* **2000**, *41*, 8573.

(14) Yang, J.; Liau, K.; Wang, C.; Hwang, C. *J. Am. Chem. Soc.* **2004**, *126*, 12325.

(15) Oelgem Ller, M.; Brem, B.; Frank, R.; Schneider, S.; Lenoir, D.; Hertkorn, N.; Origane, Y.; Lemmen, P.; Lex, J.; Inoue, Y. *J. Chem. Soc., Perkin Trans. 2* **2002**, 1760.

(16) Liu, Y.; Ran, X.; Feng, J.; Ren, A.; Zou, L. *Aust. J. Chem.* **2010**, *63*, 125.

(17) Wei, Y.; Chen, C. *J. Am. Chem. Soc.* **2007**, *129*, 7478.

(18) Chen, C.; Wei, Y.; Lin, J.; Moturu, M. V. R. K.; Chao, W.; Tao, Y.; Chien, C. *J. Am. Chem. Soc.* **2006**, *128*, 10992.

(19) Wei, Y.; Wang, W.; Huang, Y.; Wang, B.; Chen, W.; Wu, S.; He, C. *J. Mater. Chem. C* **2014**, *2*, 1779.

(20) Tai, C.; Hsieh, C.; Hsiao, K.; Wang, B.; Wei, Y. *Org. Electron.* **2015**, *16*, 54.

(21) Wei, Y.; Liu, P.; Lee, R.; Chen, C. *RSC Adv.* **2015**, *5*, 7897.

(22) Shen, P. Y.; Wu, S. H.; Huang, Y. T.; Wei, Y. *Res. Chem. Intermed.* **2014**, *40*, 2199.

(23) Samori, S.; Tojo, S.; Fujitsuka, M.; Ryhding, T.; Fix, A. G.; Armstrong, B. M.; Haley, M. M.; Majima, T. *J. Org. Chem.* **2009**, *74*, 3776.

(24) Wei, Y.; Samori, S.; Tojo, S.; Fujitsuka, M.; Lin, J.; Chen, C.; Majima, T. *J. Am. Chem. Soc.* **2009**, *131*, 6698.

(25) Fujitsuka, M.; Okada, A.; Tojo, S.; Takei, F.; Onitsuka, K.; Takahashi, S.; Majima, T. *J. Phys. Chem. B* **2004**, *108*, 11935.

(26) Frisch, M. J.; Trucks, G. W.; Schlegel, H. B.; Scuseria, G. E.; Robb, M. A.; Cheeseman, J. R.; Scalmani, G.; Barone, V.; Mennucci, B.; Petersson, G. A.; Nakatsuji, H.; Caricato, M.; Li, X.; Hratchian, H. P.; Izmaylov, A. F.; Bloino, J.; Zheng, G.; Sonnenberg, J. L.; Hada, M.; Ehara, M.; Toyota, K.; Fukuda, R.; Hasegawa, J.; Ishida, M.; Nakajima, T.; Honda, Y.; Kitao, O.; Nakai, H.; Vreven, T.; Montgomery, J. A., Jr.; Peralta, J. E.; Ogliaro, F.; Bearpark, M.; Heyd, J. J.; Brothers, E.; Kudin, K. N.; Staroverov, V. N.; Kobayashi, R.; Normand, J.; Raghavachari, K.; Rendell, A.; Burant, J. C.; Iyengar, S. S.; Tomasi, J.; Cossi, M.; Rega, N.; Millam, N. J.; Klene, M.; Knox, J. E.; Cross, J. B.; Bakken, V.; Adamo, C.; Jaramillo, J.; Gomperts, R.; Stratmann, R. E.; Yazyev, O.; Austin, A. J.; Cammi, R.; Pomelli, C.; Ochterski, J. W.; Martin, R. L.; Morokuma, K.; Zakrzewski, V. G.; Voth, G. A.; Salvador, P.; Dannenberg, J. J.; Dapprich, S.; Daniels, A. D.; Farkas, Ö.; Foresman, J. B.; Ortiz, J. V.; Cioslowski, J.; Fox, D. J. *Gaussian 09*, Revision C.01; Gaussian, Inc.: Wallingford, CT, 2009.

(27) Lewis, F. D.; Bedell, A. M.; Dykstra, R. E.; Elbert, J. E.; Gould, I. R.; Farid, S. *J. Am. Chem. Soc.* **1990**, *112*, 8055.

(28) Burrows, H. D.; Greatorex, D.; Kemp, T. J. *J. Phys. Chem.* **1972**, *76*, 20.

(29) Langan, J. R.; Salmon, G. A. *J. Chem. Soc., Faraday Trans. 1* **1982**, *78*, 3645.

(30) Dainton, F.; Robinson, E. A.; Salmon, G. A. *J. Phys. Chem.* **1972**, *76*, 3897.

(31) Ruiz, E.; Cirera, J.; Alvarez, S. *Coordin. Chem. Rev.* **2005**, *249*, 2649.

(32) Sharafy, S.; Muszkat, K. A. *J. Am. Chem. Soc.* **1971**, *93*, 4119.

(33) Fukazawa, A.; Yamaguchi, E.; Ito, E.; Yamada, H.; Wang, J.; Irle, S.; Yamaguchi, S. *Organometallics* **2011**, *30*, 3870.

(34) Ge, Z.; Hayakawa, T.; Ando, S.; Ueda, M.; Akiike, T.; Miyamoto, H.; Kajita, T.; Kakimoto,

M. *Adv. Funct. Mater.* **2008**, *18*, 584.

(35) Hellwinkel, D.; Hasselbach, H. J.; Lammerzahl, F. *Angew. Chem. Int. Ed. Engl.* **1984**, *23*, 705.

(36) Samori, S.; Tojo, S.; Fujitsuka, M.; Liang, H.; Ho, T.; Yang, J.; Majima, T. *J. Org. Chem.* **2006**, *71*, 8732.

(37) Samori, S.; Tojo, S.; Fujitsuka, M.; Yang, S.; Elangovan, A.; Ho, T.; Majima, T. *J. Org. Chem.* **2005**, *70*, 6661.

(38) Samori, S.; Tojo, S.; Fujitsuka, M.; Majima, T. *J. Photochem. Photobiol., A* **2009**, *205*, 179.

Chapter 2. Intramolecular Electron Transfer from Excited Aromatic Diimide Radical Anion:

Chapter 2-1. Unprecedented Intramolecular Electron Transfer from Excited Perylenediimide Radical Anion

Abstract

Radical anions in the excited states can be treated as stronger reductants than those in the ground states. In this study, the intramolecular electron transfer (ET) processes from excited perylenediimide radical anion ($PDI^{\bullet-}$*) were examined for the first time by applying femtosecond laser flash photolysis to the reduced dyads of PDI and acceptors (A). Efficient intramolecular ET from $PDI^{\bullet-}$* was detected upon excitation of $PDI^{\bullet-}$-pyromellitimide (PI) and $PDI^{\bullet-}$-naphthalenediimide (NDI) because of the sufficient driving forces. In particular, unprecedented ET processes were confirmed in a PDI-PDI dimer. Excitation of $PDI^{\bullet-}$-PDI gave the shortest $PDI^{\bullet-}$* lifetime due to the fastest intramolecular ET. Surprisingly, an intramolecular disproportionation reaction generating the dianion of PDI and neutral PDI was confirmed upon excitation of $PDI^{\bullet-}$-$PDI^{\bullet-}$. These processes successfully simulated the photocarrier (polaron and bipolaron) generation in PDI-based n-type semiconducting materials for various organic molecular devices. Comparing the $NDI^{\bullet-}$*-A and $PDI^{\bullet-}$*-A dyad systems, the difference found in the intramolecular ET rate constants could be explained by the energy required to form the reduced spacer and the distances between the electron donors and acceptors.

Introduction

Radical ions have been proved to play crucial roles as intermediates in many chemical, physical, and biological processes. Radical ions in the excited states have unique characteristics that are different from those in the ground states. Photoexcitation increases the redox ability of radical ions for driving chemical reactions. Thus, some processes such as electron transfer (ET), bond dissociation, and bond formation, which cannot occur in the ground states, can be expected in the excited states. So far, various theoretical[1-4] and experimental studies[5-18] have been carried out to clarify the characteristics of excited radical ions.

Radical anions in the excited states can be treated as stronger reductants than those in the ground states. Previously, the contributions of the excited radical anions of anthracenes and benzoquinones to some photoelectrochemical reactions were indicated by the product analysis.[19-21] The lifetimes of excited radical anions of quinones, ketones, anthracenes, phenazines, and stilbenes have been indirectly determined using nanosecond transient absorption spectroscopy, fluorescence spectroscopy, and pulse radiolysis-laser flash photolysis.[22-25] Later, the direct detection of the transient absorption spectra of excited radical anions and the ET processes initiated by the excited naphthalene-1,4,5,8-tetracarboxydiimide radical anion ($NDI^{\bullet-}$*) was reported by Wasielewski et al.[26-29] The fast internal conversion from excited radical anions of anthracenes, quinones, and C_{60} was also revealed by several research groups.[30-33] Recently, our group has reported the detailed characteristics and mechanisms of ET processes from $NDI^{\bullet-}$* and $C_{60}^{\bullet-}$* by applying femtosecond laser flash photolysis to the reduced dyad molecules.[34,35] It should be pointed out that excited radical ions can be efficient precursors not only for chemical reactions but also for photocarriers in organic polymeric and crystalline materials, although their generation pathways and dynamics are unknown.

As one of the most famous n-type semiconductor materials, perylene-3,4,9,10-tetracarboxydiimide (PDI) has been extensively used as a core component in organic field-effect transistors (OFETs), organic light emitting diodes (OLEDs), and organic solar cells (OSCs).[36-38] In particular, the radical anion of PDI ($PDI^{\bullet-}$) as a photocarrier often plays an essential role in its electronic and optical performance.[39,40] PDI has a similar or slightly lower reduction potential than NDI.[41,42] $PDI^{\bullet-}$ has stronger absorption bands when compared with those of $NDI^{\bullet-}$ in the

visible and near-infrared (NIR) regions.[43] The molar absorption coefficient maximum (ε_{max}) of $PDI^{\bullet-}$ is reported to be 8.0×10^4 M^{-1} cm^{-1} at 700 nm, which is nearly 3.5 times higher than that of $NDI^{\bullet-}$ (2.3×10^4 M^{-1} cm^{-1} at 474 nm), supporting the more efficient photosensitizing ability of $PDI^{\bullet-}$ due to its larger absorption cross section.[27] Moreover, the excited state properties of $PDI^{\bullet-}$ are also important for the above-mentioned organic molecular devices when considering the role of charge carrier in photoconductivity etc., although the information of excited $PDI^{\bullet-}$ ($PDI^{\bullet-}$*) is extremely scarce.

Thus, in this study, the intramolecular ET processes in the dyad molecules of PDI and acceptors including phthalimide (Ph), 1,8-naphthalimide (NI), pyromellitimide (PI), NDI, and especially PDI itself were investigated to illustrate the electron-donating/photocarrier-generating nature of the excited radical anion, $PDI^{\bullet-}$* for the first time. Scheme 2-1-1 shows the chemical structures of PDI, PDI-Ph, PDI-NI, PDI-PI, PDI-NDI, and PDI-PDI. Tridecan-7-yl or 2-ethylhexyl groups were introduced to the aromatic diimides in order to ensure substantial solubility in organic solvents. Additionally, benzene ring was employed as the spacer realizing a fixed donor-acceptor distance and a minimized π-conjugation with donor or acceptor due to the perpendicular conformation caused by steric effect.

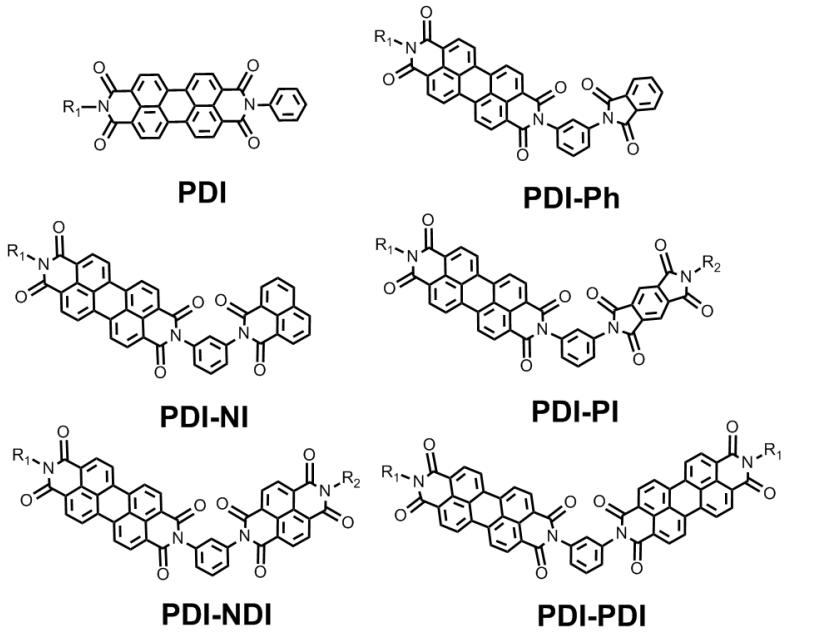

Scheme 2-1-1. Chemical structures of PDI, PDI-Ph, PDI-NI, PDI-PI, PDI-NDI, and PDI-PDI.

Experimental Section

Synthesis.

1-Hexylheptylamine (1)

2.54 g (12.80 mmol) 7-Tridecanone, 9.75 g (126 mmol) NH_4OAc, and 0.57 g (9.08 mmol) $NaBH_3CN$ were dissolved in 30 mL MeOH and stirred at room temperature for 2 d. The mixture was quenched by adding 2 mL of 2M HCl and then concentrated with a rotary evaporator. The resulting white solid was dispersed in 200 mL H_2O, adjusted to pH=10 with KOH, and extracted by 300 mL and then 150 mL of $CHCl_3$. The pale yellow oil **1** (2.34 g, 11.73 mmol, 92%) was obtained by concentrating the $CHCl_3$ fractions.

^{1}H NMR ($CDCl_3$, 400 MHz): δ 0.87 (t, J = 6.4 Hz, 6H), 1.28 (m, 20H), 1.96 (m, 1H), 2.66 (br, 2H).

N,*N*'-Bis(1-hexylheptyl)perylene-3,4,9,10-tetracarboxylbisimide (2)

2.34 g (11.73 mmol) **1** and 6.00 g (15.30 mmol) perylene-3,4,9,10-tetracarboxylic-dianhydride in 15 g imidazole were stirred 2h at 160 ℃. The reaction mixture was cooled to room temperature, dispersed in 100 mL methanol. The dark red precipitate was filled and dried over Na_2SO_4. Further purification was carried by column chromatography (silica gel; chloroform) to obtain the red solid **2** (8.57 g, 11.36 mmol, 97%).

^{1}H NMR ($CDCl_3$, 400 MHz): δ 0.81 (t, J = 6.9 Hz, 12H), 1.21 (m, 32H), 1.82 (m, 4H), 2.20 (m, 4H), 5.15 (m, 2H), 8.64 (m, 8H).

N-(1-Hexylheptyl)perylene-3,4,9,10-tetracarboxyl-3,4-anhydride-9,10-imide (3)

8.57 g (11.36 mmol) **2** was suspended in 250 mL *t*-BuOH and treated with 0.74 g (13.13 mmol) solid KOH. The reaction mixture was heated with stirring to reflux for 2 h. The mixture was cooled to room temperature, treated with 180 mL acetic acid and then 60 mL of 2M HCl and stirred overnight. The precipitate was filtered, washed with distilled water, and dried in a vacuum oven at 90 ℃. Further purification was carried by column chromatography (silica gel; chloroform) to obtain the dark red solid **3** (2.67 g, 4.65 mmol, 41%).

^{1}H NMR ($CDCl_3$, 400 MHz): δ 0.81 (t, J = 6.9 Hz, 6H), 1.23 (m, 12H), 1.84 (m, 4H), 2.20 (m, 4H), 5.15 (m, 1H), 8.57 (m, 8H).

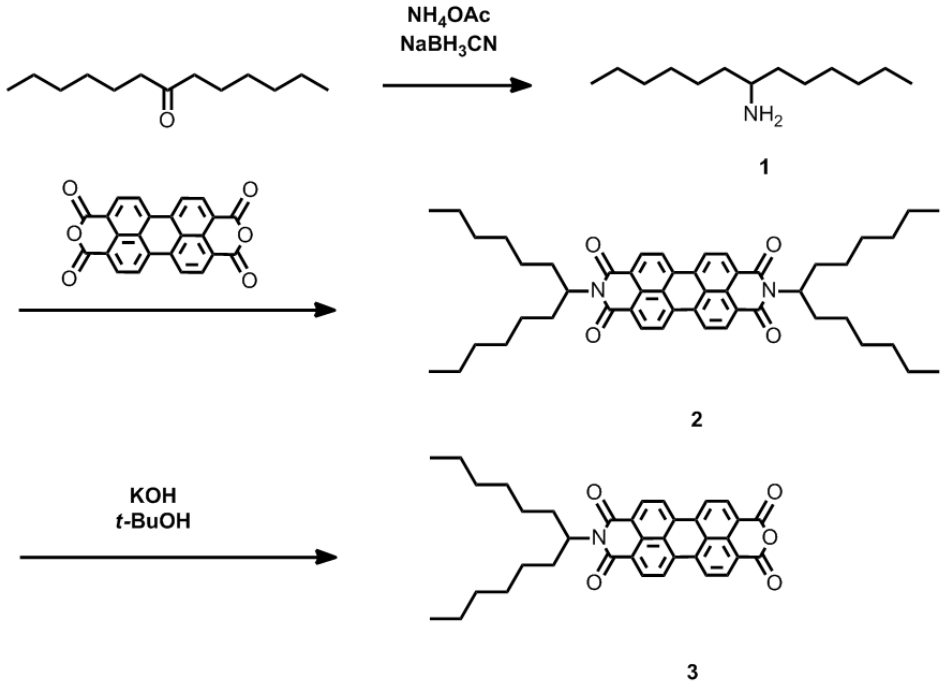

Scheme 2-1-2. Synthesis of **3**.

PDI

3 (0.10 g, 0.17 mmol) and aniline (48 mg, 0.51 mmol) were dissolved in 50 mL of DMF. The reaction mixture was heated with stirring to reflux for 24 h under argon atmosphere. Afterwards the reaction mixture was evaporated in vacuo and further purified by column chromatography (silica gel; chloroform) to obtain the dark red solid **PDI** (44 mg, 0.068 mmol, 40%).

^{1}H NMR ($CDCl_3$, 400 MHz): δ 0.82 (t, J = 7.2 Hz, 6H), 1.21 (m, 12H), 1.84 (m, 4H), 2.22 (m, 4H), 5.17 (m, 1H), 7.36 (d, J = 8.3 Hz, 2H), 7.51 (t, J = 7.6 Hz, 1H), 7.58 (t, J = 7.6 Hz, 2H), 8.68 (m, 8H).

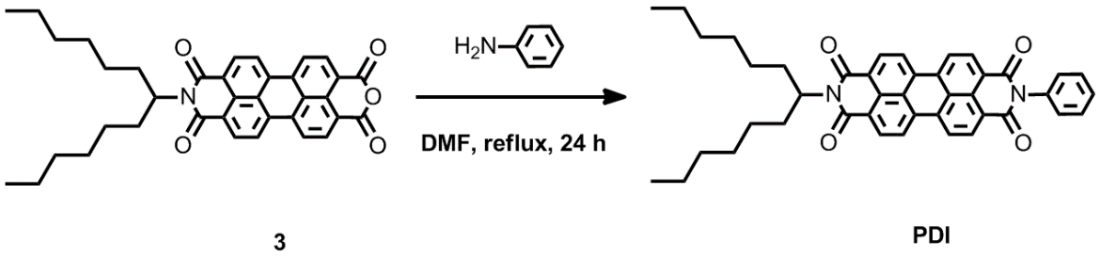

Scheme 2-1-3. Synthesis of **PDI**.

***N*-(3-Aminophenyl)phthalimide (4)**

Phthalic anhydride (3.01 g, 20.32 mmol) and *m*-phenylenediamine (2.19 g, 20.25 mmol) were dissolved in 30 mL of DMF. The reaction mixture was heated with stirring at 110 ℃ for 24 h under argon atmosphere. Afterwards the reaction mixture was evaporated in vacuo and further purified by column chromatography (silica gel; dichloromethane) to obtain the pale yellow solid **4** (1.76 g, 7.39 mmol, 36%).

^{1}H NMR ($CDCl_3$, 400 MHz): δ 3.79 (br, 2H), 6.70 (m, 1H), 6.73 (m, 1H), 6.80 (d, *J* = 7.8 Hz, 1H), 7.25 (t, *J* = 3.9 Hz, 1H), 7.77 (m, 2H), 7.94 (m, 2H).

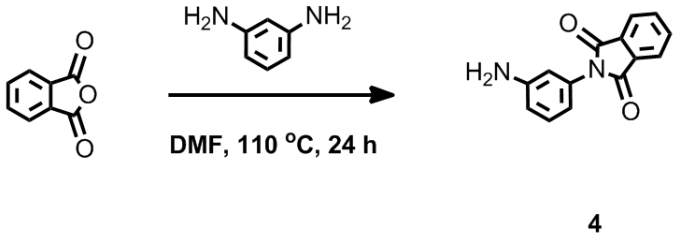

Scheme 2-1-4. Synthesis of **4**.

PDI-Ph

4 (0.20 g, 0.84 mmol) and **3** (0.32 g, 0.56 mmol) were dissolved in 10 mL of DMF. The reaction mixture was heated with stirring to reflux for 24 h under argon atmosphere. Afterwards the reaction mixture was evaporated in vacuo and purified by column chromatography (silica gel; chloroform). Further purification was carried by column chromatography (silica gel; chloroform/ethyl acetate (gradient)) to obtain the dark red solid **PDI-Ph** (48 mg, 0.06 mmol, 11%).

^{1}H NMR ($CDCl_3$, 400 MHz): δ 0.81 (t, *J* = 6.9 Hz, 6H), 1.24 (m, 12H), 1.84 (m, 4H), 2.23 (m, 4H), 5.15 (m, 1H), 7.41 (m, 1H), 7.64 (s,1H), 7.71 (m, 2H), 7.79 (dd, *J* = 5.5, 2.8 Hz, 2H), 7.96 (dd, *J* = 5.5, 3.2 Hz, 2H), 8.64 (m, 8H). FAB MS: calcd. 793.32, found 795 (M+1).

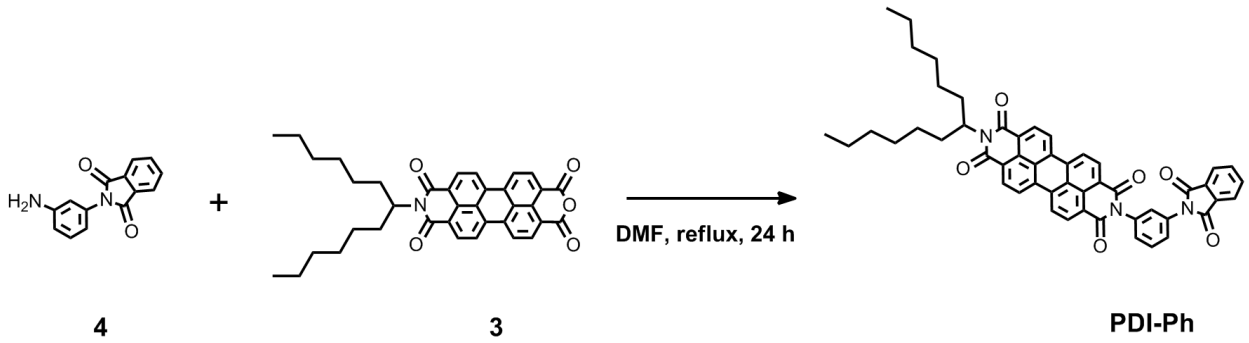

Scheme 2-1-5. Synthesis of **PDI-Ph**.

***N*-(3-Aminophenyl)-1,8-naphthalenedicarboximide (5)**

Naphthal anhydride (3.97 g, 20.03 mmol) and *m*-phenylenediamine (2.17 g, 20.07 mmol) were dissolved in 30 mL of DMF. The reaction mixture was heated with stirring at 110 ℃ for 24 h under argon atmosphere. Afterwards the reaction mixture was evaporated in vacuo and further purified by column chromatography (silica gel; dichloromethane/ethyl acetate (1:20, v/v)) to obtain the yellow solid **5** (2.01 g, 6.97 mmol, 35%).

^{1}H NMR ($CDCl_3$, 400 MHz): δ 3.78 (br, 2H), 6.62 (t, *J* = 2.1 Hz, 1H), 6.69 (d, *J* = 7.8 Hz, 1H), 6.78 (dd, *J* = 8.2, 2.3 Hz, 1H), 7.31 (t, *J* = 8.0 Hz, 1H), 7.77 (t, *J* = 7.8 Hz, 2H), 8.26 (d, *J* = 8.3 Hz, 2H), 8.64 (t, *J* = 8.5 Hz, 2H).

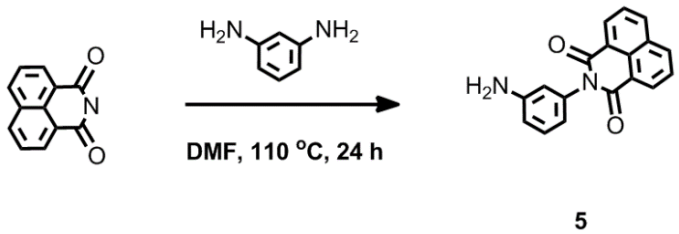

Scheme 2-1-6. Synthesis of **5**.

PDI-NI

5 (0.49 g, 1.70 mmol) and **3** (0.65 g, 1.13 mmol) were dissolved in 40 mL of DMF. The reaction mixture was heated with stirring to reflux for 7 d under argon atmosphere. Afterwards the reaction mixture was evaporated in vacuo and purified by column chromatography (silica gel; dichloromethane). Further purification was carried by column chromatography (silica gel; dichloromethane/ethyl acetate (gradient)) to obtain the dark red solid **PDI-NI** (52 mg, 0.06 mmol, 5%).

^{1}H NMR ($CDCl_3$, 400 MHz): δ 0.82 (m, 6H), 1.23 (m, 12H), 1.84 (m, 4H), 2.23 (m, 4H), 5.19 (m, 1H), 7.42 (s, 1H), 7.51 (m, 1H), 7.75 (m, 4H), 8.27 (d, *J* = 8.3 Hz, 2H), 8.65 (m, 10H). FAB MS: calcd. 843.33, found 845 (M+1).

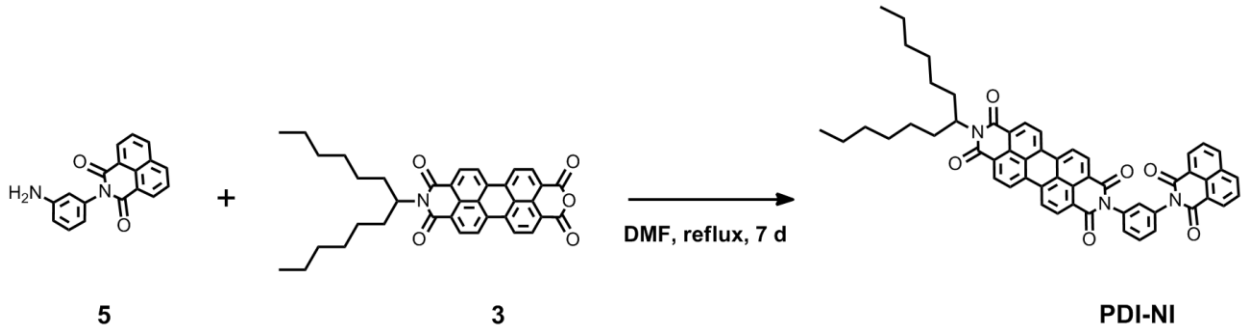

Scheme 2-1-7. Synthesis of **PDI-NI**.

***N*-(2-Ethylhexyl)benzene-1,2-dicarboxyanhydride-4,5-dicarboximide (6)**

1,2,4,5-Benzenetetracarboxylic dianhydride (8.95 g, 41.03 mmol) was placed in 100 mL of DMF and heated to 80 °C. 2-Ethyl-1-hexylamine (5.29 g, 40.93 mmol) dissolved in 30 mL of DMF was added drop wise to the reaction flask over a period of 3 h. The reaction mixture was heated at 110 °C under argon atmosphere. After 24 h, the reaction mixture was cooled to room temperature. Disubstituted precipitate was removed by filtration. The DMF filtrate was then evaporated in vacuo and the tacky residue was dissolved in dichloromethane. Some unreacted starting material precipitated from dichloromethane as a white solid and was easily filtered off. The filtrate was evaporated in vacuo. Further purification was achieved by column chromatography (silica gel; dichloromethane/ethyl acetate (gradient)). After the column, the tacky material dissolved in acetic anhydride was heated at 80 ℃ for 8 h to yield the pale yellow solid **6** (1.28 g, 3.89 mmol, 10%).

^{1}H NMR ($CDCl_3$, 400 MHz): δ 0.87 (m, 6H), 1.27 (m, 8H), 1.84 (m, 1H), 3.64 (d, J = 6.9 Hz, 2H), 8.32 (s, 2H).

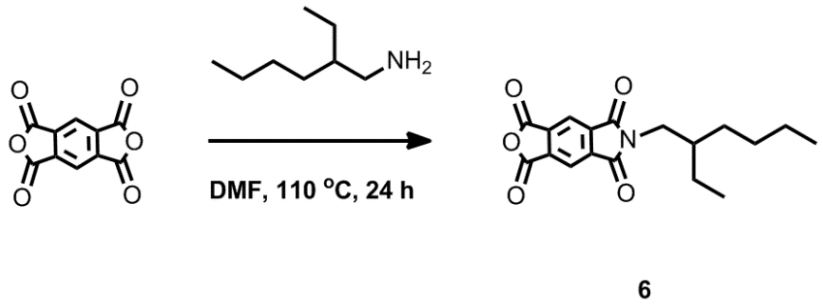

6

Scheme 2-1-8. Synthesis of **6**.

2-(3-Aminophenyl)-6-(2-ethylhexyl)pyrrolo[3,4-*f*]isoindole-1,3,5,7(2*H*,6*H*)-tetraone (7)

m-Phenylenediamine (0.29 g, 2.68 mmol) was dissolved in 50 mL of DMF and heated to 80 °C. To this solution **6** (0.88 g, 2.67 mmol) dissolved in 50 mL of DMF was added drop wise over a period of 20 h. The reaction mixture was heated at 110 ℃ for 24 h under argon atmosphere. The reaction mixture was concentrated under reduced pressure, and then dissolved in 50 mL of dichloromethane, and washed with water (120 mL × 3). Afterwards the solution was extracted by dichloromethane/ethyl acetate and evaporated in vacuo to give a crude product. Further purification was carried by column chromatography (silica gel; dichloromethane and then dichloromethane/ethyl acetate (gradient)) to obtain the yellow solid **7** (0.37 g, 0.88 mmol, 33%).

^{1}H NMR ($CDCl_3$, 400 MHz): δ 0.87 (m, 6H), 1.29 (m, 8H), 1.86 (m, 1H), 3.65 (d, J = 6.9 Hz, 2H), 3.84 (br, 2H), 6.74 (m, 2H), 6.81 (d, J = 6.9 Hz, 1H), 7.29 (m, 1H), 8.37 (s, 2H).

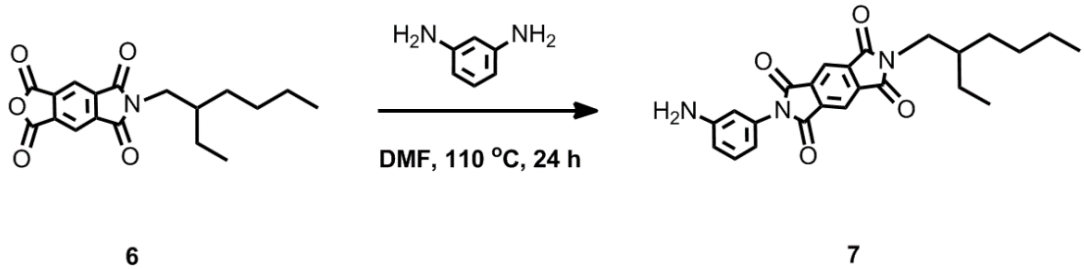

6 7

Scheme 2-1-9. Synthesis of **7**.

PDI-PI

7 (0.37 g, 0.88 mmol) and **3** (0.51 g, 0.89 mmol) were dissolved in 30 mL of DMF. The reaction mixture was heated with stirring to reflux for 10 d under argon atmosphere. Afterwards the reaction mixture was evaporated in vacuo and purified by column chromatography (silica gel; chloroform and then chloroform/ethyl acetate (gradient)). Further purification was carried by column chromatography (silica gel; dichloromethane and then dichloromethane/ethyl acetate (gradient)) to obtain the dark red solid **PDI-PI** (50 mg, 0.05 mmol, 6%).

^{1}H NMR ($CDCl_3$, 400 MHz): δ 0.81 (m, 12H), 1.24 (m, 21H), 1.84 (m, 4H), 2.20 (m, 4H), 3.65 (d, J = 7.3 Hz, 2H), 5.16 (m, 1H), 7.43 (m, 1H), 7.65 (m, 1H), 7.72 (m, 2H), 8.37 (s, 2H), 8.62 (m, 8H). FAB MS: calcd. 974.43, found 976 (M+1).

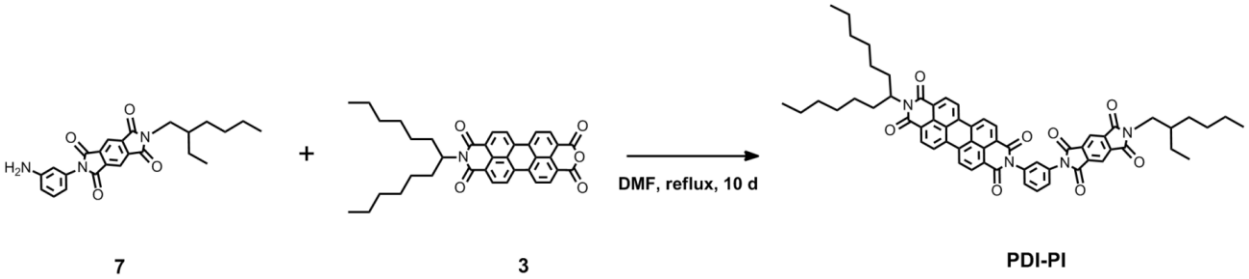

Scheme 2-1-10. Synthesis of **PDI-PI**.

***N*-(2-Ethylhexyl)naphthalenetetracarboxylic monoanhydride monoimide (8)**

In a single-neck round-bottom flask equipped with a reflux condenser, 1,4,5,8-naphthalenetetracarboxylic dianhydride (6.18 g, 23.04 mmol) was suspended in 80 mL of DMF, and the solution was stirred to 80 ℃. To this solution 2-ethyl-1-hexylamine (2.98 g, 23.06 mmol) was added drop wise over a period of 1 h and the mixture was heated at 120 ℃ under argon atmosphere. After 24 hours, the reaction mixture was cooled to room temperature and the precipitated diimide were filtered off. DMF was evaporated under reduced pressure. The crude material was purified by column chromatography (silica gel; dichloromethane) to obtain the pale yellow solid **8** (4.09 g, 10.78 mmol, 47%).

^{1}H NMR ($CDCl_3$, 400 MHz): δ 0.87 (t, J = 6.9 Hz, 3H), 0.93 (t, J = 7.3 Hz, 3H), 1.30 (m, 8H), 1.91 (m, 1H), 4.10 (m, 2H), 8.82 (m, 4H).

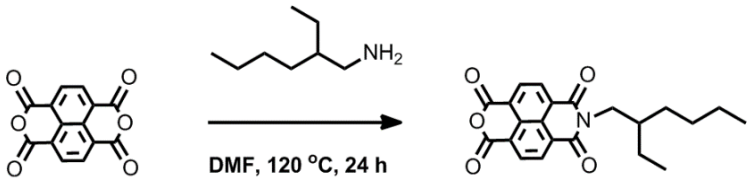

8

Scheme 2-1-11. Synthesis of **8**.

2-(3-Aminophenyl)-7-(2-ethylhexyl)benzo[*lmn*][3,8]phenanthroline-1,3,6,8(2*H*,7*H*)-tetraone (9)

8 (0.97 g, 2.78 mmol) and *m*-phenylenediamine (0.35 g, 3.24 mmol) were dissolved in 40 mL of DMF. The reaction mixture was heated with stirring at 120 ℃ for 24 h under argon atmosphere. Afterwards the reaction mixture was evaporated in vacuo, purified by column chromatography (silica gel; dichloromethane and then dichloromethane/ethyl acetate (gradient)) and concentrated to obtain the dark brown solid **9** (0.56 g, 1.19 mmol, 43%).

^{1}H NMR ($CDCl_3$, 400 MHz): δ 0.87 (t, *J* = 6.9 Hz, 3H), 0.93 (t, *J* = 7.3 Hz, 3H), 1.31 (m, 8H), 1.93 (m, 1H), 3.82 (br, 2H), 4.12 (m, 2H), 6.61 (t, *J* = 2.1 Hz, 1H), 6.68 (d, *J* = 7.8 Hz, 1H), 6.80 (dd, *J* = 8.2, 2.3 Hz, 1H), 7.32 (t, *J* = 8.0 Hz, 1H), 8.80 (m, 4H).

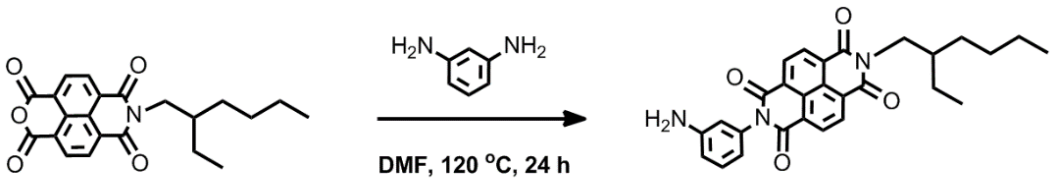

8 9

Scheme 2-1-12. Synthesis of **9**.

PDI-NDI

9 (0.11 g, 0.23 mmol) and **3** (0.11 g, 0.19 mmol) were dissolved in 40 mL of DMF. The reaction mixture was heated with stirring to reflux for 4 d under argon atmosphere. Afterwards the reaction mixture was evaporated in vacuo and purified by column chromatography (silica gel; chloroform and then chloroform/ethyl acetate (gradient)). Further purification was carried by

column chromatography (silica gel; dichloromethane and then dichloromethane/ethyl acetate (gradient)) to obtain the dark red solid **PDI-NDI** (50 mg, 0.05 mmol, 26%).

^{1}H NMR ($CDCl_3$, 400 MHz): δ 0.82 (m, 12H), 1.23 (m, 16H), 1.86 (m, 6H), 2.18 (m, 6H), 4.02 (m, 3H), 5.15 (m, 1H), 7.41 (s, 1H), 7.51 (m, 2H), 7.76 (t, *J* = 7.6 Hz, 1H), 8.44 (m, 12H). FAB MS: calcd. 1025.44, found 1027 (M+1).

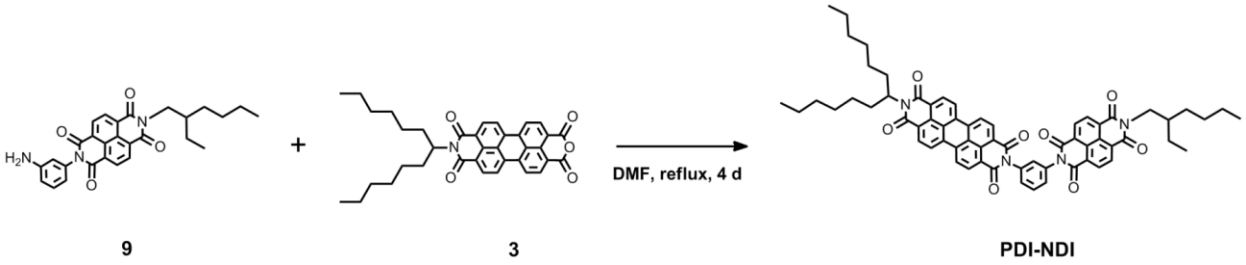

9 3 PDI-NDI

Scheme 2-1-13. Synthesis of **PDI-NDI**.

PDI-PDI

3 (0.92 g, 1.60 mmol) and *m*-phenylenediamine (0.09 g, 0.83 mmol) were dissolved in 40 mL of DMF. The reaction mixture was heated with stirring to reflux for 4 d under argon atmosphere. Afterwards the reaction mixture was evaporated in vacuo and purified by column chromatography (silica gel; chloroform and then chloroform/ethyl acetate (gradient)). Further purification was carried by column chromatography (silica gel; dichloromethane and then dichloromethane/ethyl acetate (gradient)) to obtain the dark red solid **PDI-PDI** (50 mg, 0.04 mmol, 5%).

^{1}H NMR ($CDCl_3$, 400 MHz): δ 0.81 (t, *J* = 6.9 Hz, 12H), 1.23 (m, 32H), 1.83 (m, 4H), 2.22 (m, 4H), 5.14 (m, 2H), 7.46 (s, 1H), 7.54 (d, *J* = 7.8 Hz, 2H), 7.77 (t, *J* = 8.0 Hz, 1H), 8.64 (m, 16H). FAB MS: calcd. 1218.55, found 1220 (M+1).

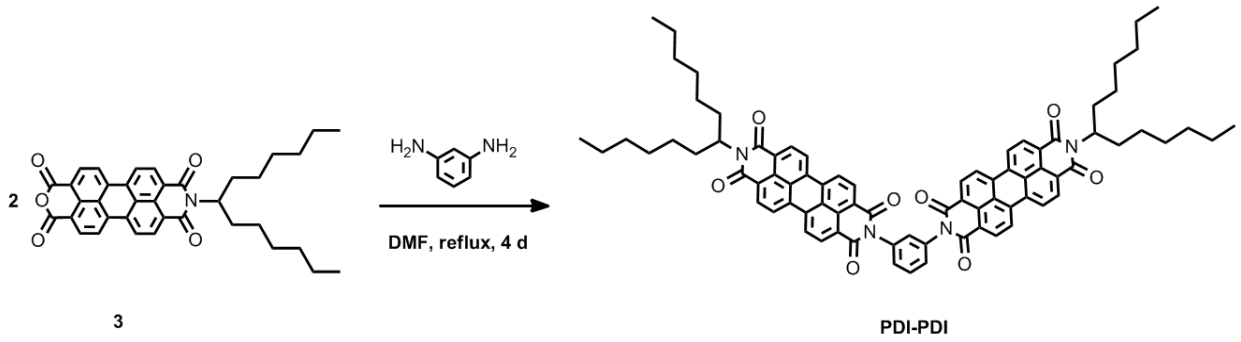

Scheme 2-1-14. Synthesis of **PDI-PDI**.

Materials. PDI, PDI-Ph, PDI-NI, PDI-PI, PDI-NDI, and PDI-PDI were synthesized as described above. In the present study, *N*,*N*-dimethylformamide (DMF) was used as the solvent for all the spectroscopies. Tetrakis(dimethylamino)ethylene (TDAE) was purchased from Tokyo Chemical Industry.

Apparatus. Steady-state absorption spectra were measured using a Shimadzu UV-3600 UV-vis-NIR spectrometer. Transient absorption spectra during the femtosecond laser flash photolysis were measured as described in the former paper.[44] In the present study, the samples were excited by a 700 nm femtosecond laser pulse (~130 fs fwhm, ~5 μJ per pulse).

Theoretical Calculations. Optimized structures of the molecules in this study were estimated using density functional theory (DFT) at the (U)B3LYP/6-31G(d) level. All theoretical calculations were carried out using the Gaussian 09 package.[45] It was confirmed that the estimated structures did not exhibit imaginary frequencies.

Results and Discussion

Figure 2-1-1 shows the absorption spectra of PDI with varied concentrations of TDAE in DMF. With stepwise addition of TDAE,[46] the absorbance of neutral PDI showed a decrease and new absorption bands at 680, 700, 712, 766, 795, and 955 nm appeared, which can be attributed to the radical anion, $PDI^{\bullet-}$. The absorbance of $PDI^{\bullet-}$ reached its maximum with the addition of an equivalent amount of TDAE. The ratio between the maximum absorbance of neutral PDI and

that of $PDI^{\bullet-}$ was similar to the reported value,[27] suggesting a quantitative reduction of PDI by TDAE. Moreover, the absorption bands of $PDI^{\bullet-}$ kept their intensity for several hours when oxygen had been removed from the solvent by Ar bubbling, indicating that $PDI^{\bullet-}$ was stable under the experimental conditions. Similar phenomena were also confirmed in the cases of PDI-Ph, PDI-NI, PDI-PI and PDI-NDI, implying that the PDI moiety in these dyads can be selectively reduced by TDAE. As for the PDI-PDI dimer, one- or two-equivalent amount of TDAE was added for the preparation of $PDI^{\bullet-}$-PDI or $PDI^{\bullet-}$-$PDI^{\bullet-}$, respectively. The spectral shape of $PDI^{\bullet-}$-$PDI^{\bullet-}$ was the same as that of $PDI^{\bullet-}$, indicating negligible interactions between the two $PDI^{\bullet-}$ moieties. Neither inter- nor intramolecular disproportionation was confirmed to occur in the ground state.

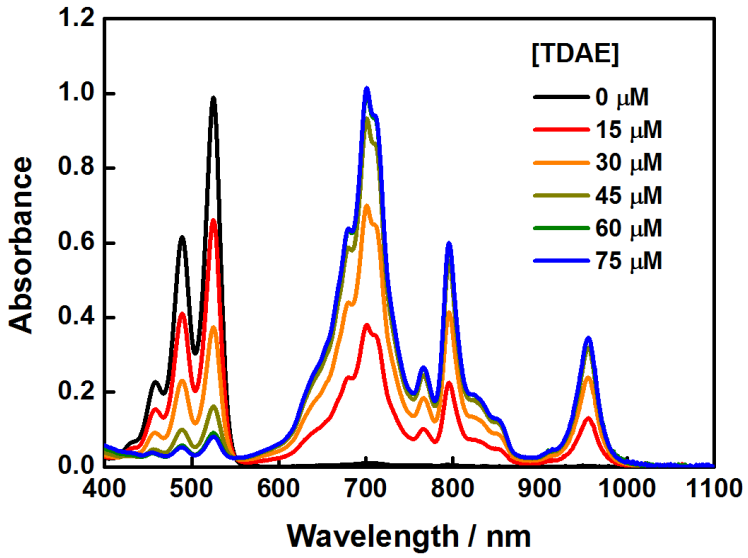

Figure 2-1-1. Absorption spectra of PDI (60 μM) with varied concentrations of TDAE (0−75 μM) in DMF.

Figure 2-1-2a shows the transient absorption spectra of $PDI^{\bullet-}$ during the laser flash photolysis using a 700 nm femtosecond laser. The spectrum taken at 32 ps after the laser excitation showed positive signals with maxima at 455 and 600 nm, and negative signals with minima at 520, 673, 696, and 707 nm, indicating the generation of $PDI^{\bullet-}$* and bleaching of $PDI^{\bullet-}$. With an increase in the delay time, the positive signals showed a decrease whereas the negative signals showed a recovery. This phenomenon is attributed to a $D_1 \rightarrow D_0$ deactivation process from $PDI^{\bullet-}$* to $PDI^{\bullet-}$

with a lifetime of 145 ps (6.9×10^9 s^{-1}), which can be obtained by fitting a single exponential function to the decay kinetics of ΔO.D. at 455 nm (Figure 2-1-2b). It is notable that the $PDI^{\bullet-}$* lifetime shown here is sufficiently long for various subsequent reactions.

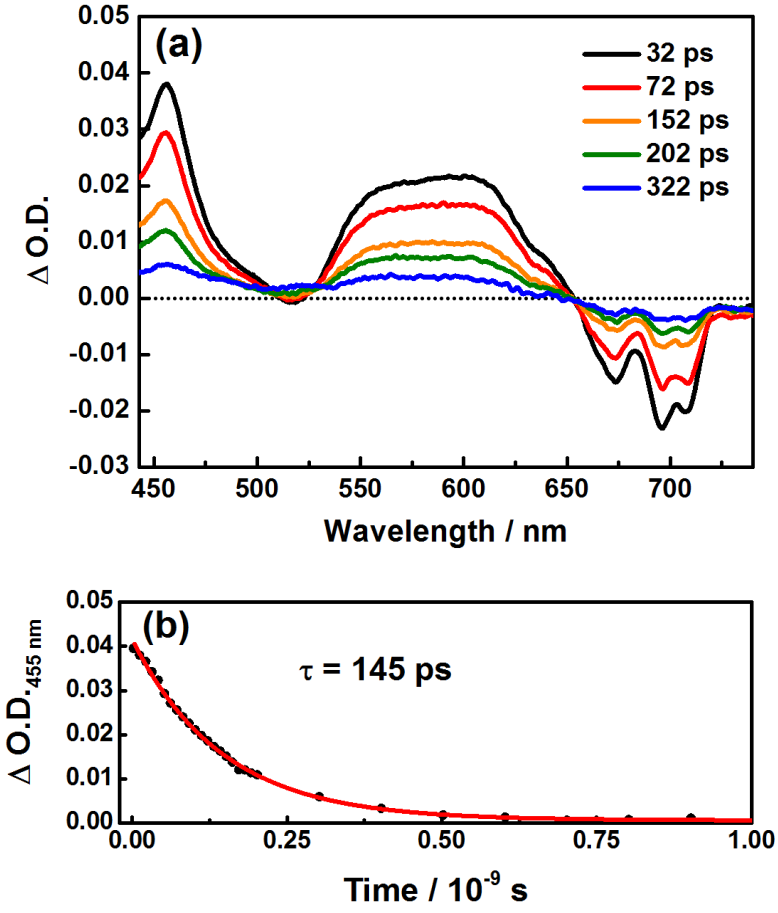

Figure 2-1-2. (a) Transient absorption spectra of PDI (60 μM) in DMF in the presence of TDAE (60 μM) during the laser flash photolysis using a 700 nm femtosecond laser and (b) kinetic trace of ΔO.D. at 455 nm.

Figure 2-1-3a shows the transient absorption spectra of $PDI^{\bullet-}$-PI during the laser flash photolysis using a 700 nm femtosecond laser. The spectrum taken at 35 ps after the laser excitation indicated the generation of $PDI^{\bullet-}$*-PI. Meanwhile, new absorption peaks appeared at 485 (PDI), 520 (PDI), and 720 nm ($PI^{\bullet-}$) due to the generation of PDI-$PI^{\bullet-}$, suggesting an intramolecular ET process from $PDI^{\bullet-}$* to PI as indicated in eq 2-1-1.

$$PDI^{\bullet-}\text{*-PI} \xrightarrow{k_{intraET}} PDI\text{-}PI^{\bullet-} \qquad (2\text{-}1\text{-}1)$$

The kinetic trace of ΔO.D. at 455 nm decayed with a constant of 8.5×10^9 s^{-1} (Figure 2-1-3b). Therefore, the intramolecular ET rate constant ($k_{intraET}$) was calculated to be 1.6×10^9 s^{-1} by taking into account the $D_1 \rightarrow D_0$ deactivation process ($k_d = 6.9 \times 10^9$ s^{-1}). Within the instrumental time window, the intramolecular back ET (BET) process from PDI-$PI^{\bullet-}$ to $PDI^{\bullet-}$-PI was hardly confirmed. Thus, the rate constant for this process ($k_{intraBET}$) is $< 3 \times 10^8$ s^{-1}. Similar ET processes were also confirmed in $PDI^{\bullet-}$-Ph, $PDI^{\bullet-}$-NI, and $PDI^{\bullet-}$-NDI upon excitation of the $PDI^{\bullet-}$ moiety, although the ET yields in $PDI^{\bullet-}$*-Ph and $PDI^{\bullet-}$*-NI were rather small, likely due to the lower electron-accepting ability of Ph and NI. In particular, the excitation of $PDI^{\bullet-}$-PDI gave the shortest lifetime of $PDI^{\bullet-}$* due to the fastest ET process ($PDI^{\bullet-}$*-PDI $\xrightarrow{k_{intraET}}$ PDI-$PDI^{\bullet-}$, $k_{intraET} = 1.0 \times 10^{10}$ s^{-1}), and there was no BET process because of the zero driving force.

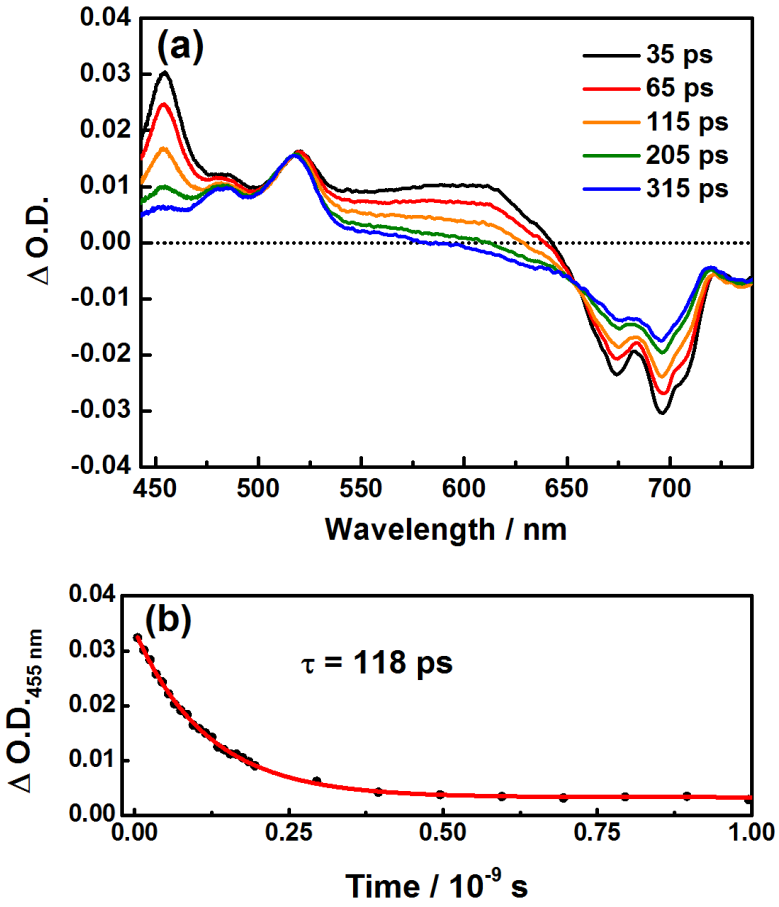

Figure 2-1-3. (a) Transient absorption spectra of PDI-PI (60 μM) in DMF in the presence of TDAE (60 μM) during the laser flash photolysis using a 700 nm femtosecond laser and (b) kinetic trace of ΔO.D. at 455 nm.

Figure 2-1-4a shows the transient visible absorption spectra of $PDI^{\bullet-}$-$PDI^{\bullet-}$ during the laser flash photolysis using a 700 nm femtosecond laser. The spectrum taken at 24 ps after the laser excitation indicated the generation of $PDI^{\bullet-}$*-$PDI^{\bullet-}$. With an increase in the delay time, new peaks appeared in the spectra. Based on the previously reported peak positions and relative intensities,[27] the absorption peaks at 530 and 573 nm are attributable to PDI and PDI^{2-}, respectively, suggesting an intramolecular ET process from $PDI^{\bullet-}$* to $PDI^{\bullet-}$ as indicated in eq 2-1-2.

$$PDI^{\bullet-}\text{*-}PDI^{\bullet-} \xrightarrow{k_{intraET}} PDI\text{-}PDI^{2-} \quad (2\text{-}1\text{-}2)$$

Thus, surprisingly, an intramolecular disproportionation reaction was confirmed upon excitation of $PDI^{\bullet-}$-$PDI^{\bullet-}$. Here, $PDI^{\bullet-}$ is considered as an electron acceptor; therefore, the reduction potential of $PDI^{\bullet-}$ (i.e., the second reduction potential of PDI) is essential for this process. In addition, the relatively small difference between the first and second reduction potentials of PDI realized a sufficient driving force for eq 2-1-2. The kinetic trace of ΔO.D. at 460 nm decayed with a constant of $9.3 \times 10^9\ s^{-1}$ (Figure 2-1-4b). Therefore, the $k_{intraET}$ was calculated to be $2.4 \times 10^9\ s^{-1}$ by taking the $D_1 \rightarrow D_0$ deactivation process into account. In addition, the generated PDI-PDI^{2-} showed a subsequent decay caused by the intramolecular BET, although the entire process could not be traced.

The above processes were further investigated in the NIR region. Figure 2-1-4c shows the transient NIR absorption spectra of $PDI^{\bullet-}$-$PDI^{\bullet-}$ in DMF under the same conditions. The spectrum taken at 88 ps after the laser excitation showed negative bands with minima at 975 and 1120 nm, corresponding to the bleaching of $PDI^{\bullet-}$ and stimulated emission from $PDI^{\bullet-}$*, respectively. By increasing the delay time to > 500 ps, all the negative absorption bands showed a recovery with only the bands due to the ground state bleaching remaining, while the band due to the stimulated emission disappeared, indicating the production of PDI-PDI^{2-} and quenching of $PDI^{\bullet-}$*-$PDI^{\bullet-}$. The kinetic trace of ΔO.D. at 1120 nm provided the same $k_{intraET}$ value mentioned in the previous paragraph (Figure 2-1-4d). It is worth noting that the kinetics of stimulated emission in the NIR region were consistent with those of the D_1 state absorption in the visible region. Thus, stimulated emission has been proved as a good marker to assign the precursor state for ET from excited radical anion.

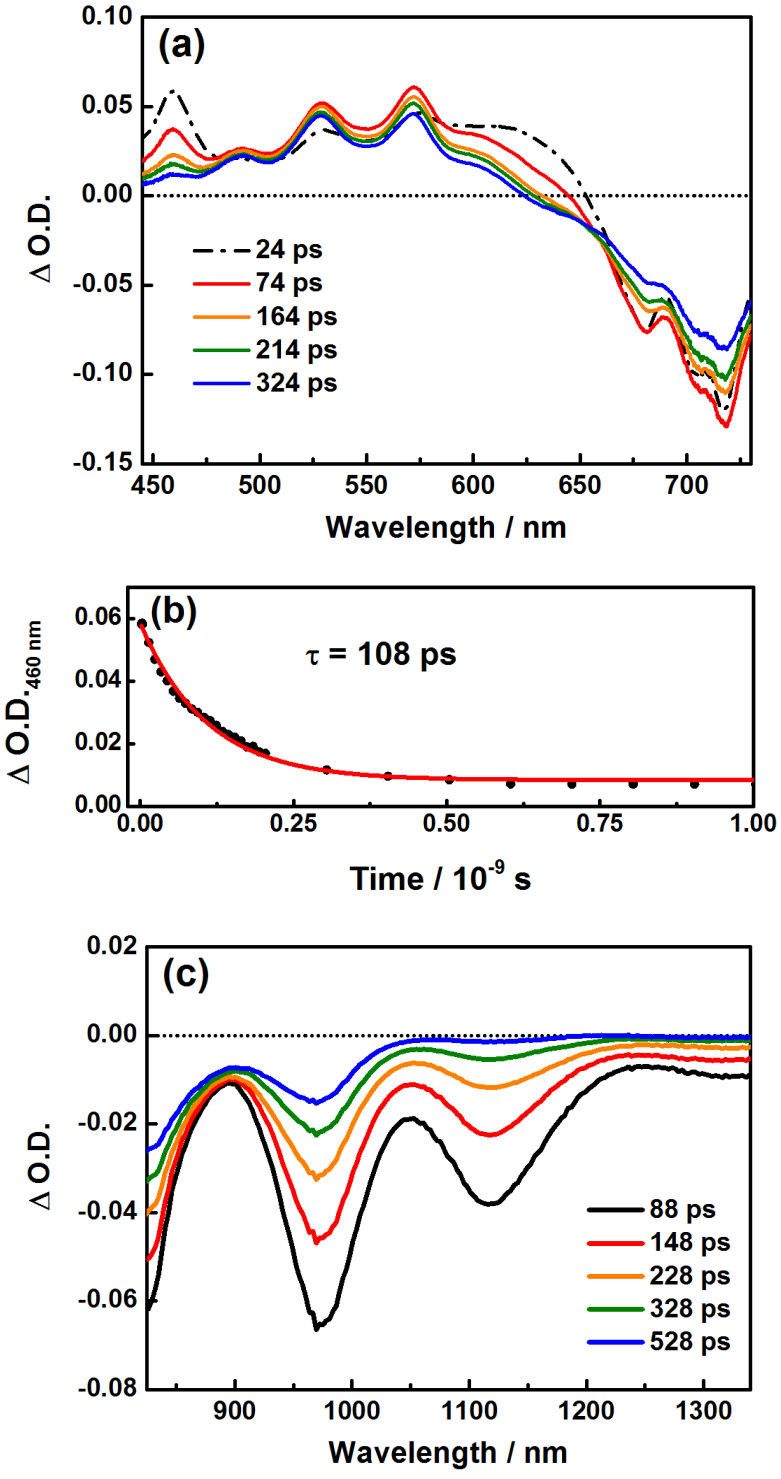
(a)
0.10
0.05
0.00
-0.05
-0.10
-0.15
Δ O.D.
24 ps
74 ps
164 ps
214 ps
324 ps
450
500
550
600
650
700
Wavelength / nm
(b)
τ = 108 ps
Δ O.D.460 nm
0.06
0.04
0.02
0.00
0.00
0.25
0.50
0.75
1.00
Time / 10-9 s
(c)
0.02
0.00
-0.02
-0.04
-0.06
-0.08
Δ O.D.
88 ps
148 ps
228 ps
328 ps
528 ps
900
1000
1100
1200
1300
Wavelength / nm

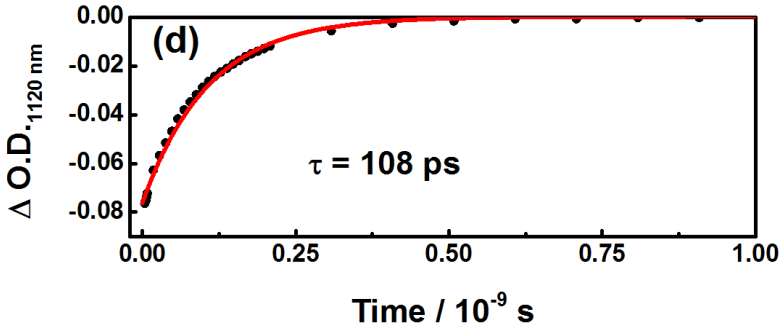

Figure 2-1-4. (a) Transient visible absorption spectra of PDI-PDI (0.12 mM) in DMF in the presence of TDAE (0.24 mM) during the laser flash photolysis using a 700 nm femtosecond laser and (b) kinetic trace of ΔO.D. at 460 nm. (c) Transient NIR absorption spectra of PDI-PDI (0.12 mM) in DMF in the presence of TDAE (0.24 mM) during the laser flash photolysis using a 700 nm femtosecond laser and (d) kinetic trace of ΔO.D. at 1120 nm.

The rate constants and driving forces for the intramolecular ET processes from $PDI^{\bullet-}$* are summarized in Table 2-1-1. The driving forces for intramolecular ET and BET ($-\Delta G_{intraET}$ and $-\Delta G_{intraBET}$) were calculated following eqs 2-1-3 and 2-1-4.

$$\Delta G_{intraET} = E(PDI^{\bullet-}/PDI) - E(A^{\bullet-}/A) - E_{D1}(PDI^{\bullet-}*) \quad (2\text{-}1\text{-}3)$$

$$\Delta G_{intraBET} = E(A^{\bullet-}/A) - E(PDI^{\bullet-}/PDI) \quad (2\text{-}1\text{-}4)$$

In the case of $PDI^{\bullet-}$*-$PDI^{\bullet-}$, the above equations were rewritten as:

$$\Delta G_{intraET} = E(PDI^{\bullet-}/PDI) - E(PDI^{2-}/PDI^{\bullet-}) - E_{D1}(PDI^{\bullet-}*) \quad (2\text{-}1\text{-}5)$$

$$\Delta G_{intraBET} = E(PDI^{2-}/PDI^{\bullet-}) - E\,(PDI^{\bullet-}/PDI) \quad (2\text{-}1\text{-}6)$$

where $E(PDI^{\bullet-}/PDI)$, $E(PDI^{2-}/PDI^{\bullet-})$, $E(A^{\bullet-}/A)$, and $E_{D1}(PDI^{\bullet-}*)$ represent the reduction potential of PDI, reduction potential of $PDI^{\bullet-}$, reduction potential of the electron acceptor, and D_1 state energy of $PDI^{\bullet-}$*, respectively. It has been suggested that the absorption band of $PDI^{\bullet-}$ at 955 nm is due to the $D_1 \leftarrow D_0$ transition;[27] thus, $E_{D1}(PDI^{\bullet-}*)$ is 1.30 eV.

As shown in Table 2-1-1, the $-\Delta G_{intraET}$ values for $PDI^{\bullet-}$*-Ph and $PDI^{\bullet-}$*-NI were calculated to be 0.33 and 0.37 eV, respectively. In these dyads, the intramolecular ET from $PDI^{\bullet-}$* was inefficient. On the other hand, the values of $-\Delta G_{intraET}$ for $PDI^{\bullet-}$*-PI, $PDI^{\bullet-}$*-NDI, $PDI^{\bullet-}$*-PDI, and $PDI^{\bullet-}$*-$PDI^{\bullet-}$ were calculated to be 1.02, 1.25, 1.30, and 1.03 eV, respectively. In these dyads, the intramolecular ET processes from $PDI^{\bullet-}$* were clearly observed, and the values of $k_{intraET}$ become larger with an increase in the values of $-\Delta G_{intraET}$.

Table 2-1-1. Rate Constants ($k_{intraET}$ and $k_{intraBET}$), Driving Forces ($-\Delta G_{intraET}$ and $-\Delta G_{intraBET}$), and Reorganization Energies (λ_o, λ_i, and λ_{tot}) for Intramolecular ET Processes from $PDI^{\bullet-}$*.

	$k_{intraET}$[a] (s^{-1})	$-\Delta G_{intraET}$ (eV)	$k_{intraBET}$[a] (s^{-1})	$-\Delta G_{intraBET}$ (eV)	λ_o (eV)	λ_i (eV)	λ_{tot} (eV)
$PDI^{\bullet-}$*-Ph	$< 1 \times 10^9$	0.33	$< 3 \times 10^8$	0.97	1.23	0.73	1.96
$PDI^{\bullet-}$*-NI	$< 1 \times 10^9$	0.37	$< 3 \times 10^8$	0.94	1.15	0.52	1.67
$PDI^{\bullet-}$*-PI	1.6×10^9	1.02	$< 3 \times 10^8$	0.28	1.16	0.69	1.85
$PDI^{\bullet-}$*-NDI	3.2×10^9	1.25	$< 3 \times 10^8$	0.05	1.10	0.56	1.66
$PDI^{\bullet-}$*-PDI	1.0×10^{10}	1.30	-[b]	0	1.09	0.49	1.58
$PDI^{\bullet-}$*-$PDI^{\bullet-}$	2.4×10^9	1.03	$< 3 \times 10^8$	0.27	-[c]	-[c]	-[c]

[a]Estimation error: < 10%. [b]Not observed. [c]Not obtained.

To obtain a deeper understanding of the driving force ($-\Delta G_{ET}$) dependence of ET rate constant (k_{ET}), Marcus theory was applied to the dyad systems. According to this theory, the k_{ET} can be expressed following eqs 2-1-(7-9):[47-49]

$$k_{ET} = \sqrt{\frac{\pi}{\hbar^2 \lambda_o k_B T}} |V|^2 \sum_m \left(e^{-S} \left(\frac{S^m}{m!} \right) \right) \exp\left(- \frac{(\lambda_o + \Delta G + m\hbar\langle\omega\rangle)^2}{4\lambda_o k_B T} \right) \quad (2\text{-}1\text{-}7)$$

$$\lambda_o = e^2 \left(\frac{1}{2r_D} + \frac{1}{2r_A} - \frac{1}{r} \right) \left(\frac{1}{n^2} - \frac{1}{\varepsilon_s} \right) \quad (2\text{-}1\text{-}8)$$

$$S = \frac{\lambda_i}{\hbar\langle\omega\rangle} \quad (2\text{-}1\text{-}9)$$

where λ_o, V, S, $\langle\omega\rangle$, and λ_i represent the outer sphere reorganization energy, electronic coupling, electron-vibration coupling constant, averaged angular frequency, and inner sphere reorganization energy, respectively. r_D, r_A, r, n, and ε_S represent the donor radius, acceptor radius, distance between the centers of the donor and acceptor, optical dielectric constant, and static dielectric constant, respectively. The λ_o values were estimated from eq 2-1-8, assuming ionic

radii (r_D *or* r_A) of 4.73, 4.27, 3.99, 3.86, and 3.58 Å for PDI, NDI, PI, NI, and Ph, respectively by means of DFT calculations. The λ_i values were estimated using a previously reported method.[50] The present ET processes are considered to be in the Marcus normal region because the k_{ET} values increase with more negative values of ΔG_{ET}, and the total reorganization energies (λ_{tot}, i.e., the sum of λ_o and λ_i) are larger than $-\Delta G_{ET}$, as listed in Table 2-1-1. The relationship between the driving forces ($-\Delta G_{intraET}$ and $-\Delta G_{intraBET}$) and ET rate constants ($k_{intraET}$ and $k_{intraBET}$) in $NDI^{\bullet-}$*-acceptors ($NDI^{\bullet-}$*-A) and $PDI^{\bullet-}$*-acceptors ($PDI^{\bullet-}$*-A) was plotted, as shown in Figure 2-1-5. The red curve was obtained by eq 2-1-7, assuming λ_o = 1.13 eV, λ_i = 0.66 eV, V = 0.013 eV, and $\hbar\langle\omega\rangle$ = 0.15 eV for $NDI^{\bullet-}$*-A,[34] and the blue curve assumed λ_o = 1.15 eV, λ_i = 0.60 eV, V = 0.0011 eV, and $\hbar\langle\omega\rangle$ = 0.15 eV for $PDI^{\bullet-}$*-A. These curves reasonably reproduced the $-\Delta G_{ET}$ dependence of k_{ET} in the dyad systems.

The difference in k_{ET} between $NDI^{\bullet-}$*-A and $PDI^{\bullet-}$*-A can be explained by two main reasons. The first is the energy for the reduced spacer. Based on the first-order perturbation theory and super-exchange mechanism, the electronic coupling between an electron donor (D) and an acceptor (A) through a spacer (S) can be expressed as follows:[51-53]

$$V = \frac{V_{DS}V_{SA}}{\Delta} \tag{2-1-10}$$

where V_{DS}, V_{SA}, and Δ represent the electronic coupling between the donor and the spacer, the electronic coupling between the spacer and the acceptor, and the energy required to form the reduced spacer, respectively. By applying the reduction potential of the spacer (E_{Sred}), the Δ values for $NDI^{\bullet-}$*-A and $PDI^{\bullet-}$*-A can be evaluated as $-2.09 - E_{Sred}$ and $-1.73 - E_{Sred}$, respectively. Because of the endothermic nature of the reduction of the spacer via the excited radical anion, the Δ values should be $\Delta_{NDI\bullet-*-A} < \Delta_{PDI\bullet-*-A}$, giving $V_{NDI\bullet-*-A} > V_{PDI\bullet-*-A}$, which is consistent with the trend shown in Figure 2-1-5. The second reason is the longer donor-acceptor distances in $PDI^{\bullet-}$*-A compared with those in $NDI^{\bullet-}$*-A (e.g., 12.8 Å for $PDI^{\bullet-}$*-PI and 10.9 Å for $NDI^{\bullet-}$*-PI). Longer donor-acceptor distances result in smaller V; thus, slower ET is expected for $PDI^{\bullet-}$*-A.

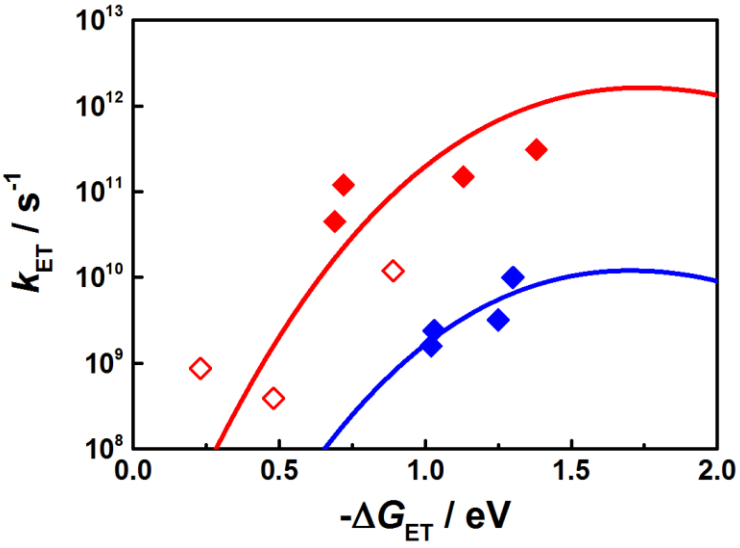

Figure 2-1-5. Driving force ($-\Delta G_{intraET}$ and $-\Delta G_{intraBET}$) dependence of ET rate constants ($k_{intraET}$ as solid squares and $k_{intraBET}$ as hollow squares). The red and blue squares correspond to $NDI^{\bullet-}$*-A and $PDI^{\bullet-}$*-A dyads, respectively.

Notably, in the current study, unprecedented ET processes were found in the dyad molecules of $PDI^{\bullet-}$*-PDI and $PDI^{\bullet-}$*-$PDI^{\bullet-}$. It should be pointed out that these ET processes are closely related to the photocurrent conduction processes in organic materials, because PDI-PDI can be regarded as the smallest unit of the conductive PDI-based polymeric and crystalline materials (Scheme 2-1-15). The photoinduced ET process and rate in $PDI^{\bullet-}$-PDI correspond to the photocarrier (i.e., polaron) generation and mobility.[54,55] The fast ET rate means rapid polaron migration. Furthermore, the production of the dianion from photoexcited $PDI^{\bullet-}$-$PDI^{\bullet-}$ implies the generation of a di-charged carrier (i.e., bipolaron) in n-type semiconducting materials.[56,57] Facile production of the bipolaronic state is achievable using densely packed PDI and/or high $PDI^{\bullet-}$ (polaron) concentrations, which can be expected in the polymeric and crystalline materials. Thus, the current findings have successfully simulated the generation of mono- and di-charged carriers, and clearly indicated the importance of pathways from excited radical anion.

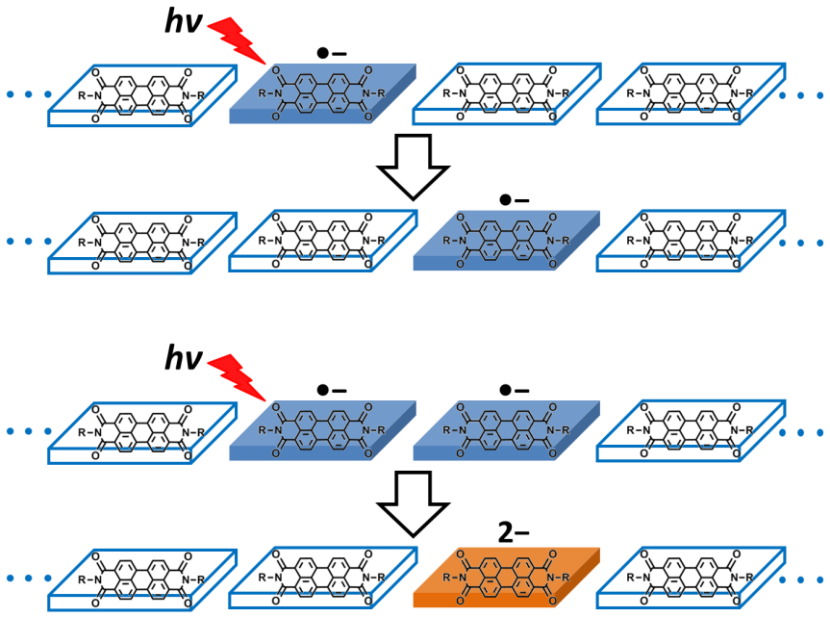

Scheme 2-1-15. Photocarriers generated from $PDI^{\bullet-}$* in n-type semiconductor materials.

Conclusions

Several dyads, including $PDI^{\bullet-}$-Ph, $PDI^{\bullet-}$-NI, $PDI^{\bullet-}$-PI, $PDI^{\bullet-}$-NDI, $PDI^{\bullet-}$-PDI, and $PDI^{\bullet-}$-$PDI^{\bullet-}$, were investigated by the femtosecond laser flash photolysis to observe the intramolecular ET processes from $PDI^{\bullet-}$* for the first time. It was found that efficient intramolecular ET occurred in $PDI^{\bullet-}$*-PI and $PDI^{\bullet-}$*-NDI because of the sufficient driving forces. In particular, $PDI^{\bullet-}$*-PDI and $PDI^{\bullet-}$*-$PDI^{\bullet-}$ exhibited quite different ET pathways. By applying the Marcus theory to the dyad systems of $NDI^{\bullet-}$*-A and $PDI^{\bullet-}$*-A, the k_{ET} difference could be reasonably explained. The results shown here provided valuable insights into the unique characteristics of $PDI^{\bullet-}$* as an electron donor and generator of photocarriers (polaron and bipolaron) in related n-type semiconductor materials for OFETs, OLEDs, and OSCs.

References

(1) Fulscher, M. P.; Matzinger, S.; Bally, T. *Chem. Phys. Lett.* **1995**, *236*, 167.

(2) Kawashima, Y.; Nakayama, K.; Nakano, H.; Hirao, K. *Chem. Phys. Lett.* **1997**, *267*, 82.

(3) Hirata, S.; Head-Gordon, M.; Szczepanski, J.; Vala, M. *J. Phys. Chem. A* **2003**, *107*, 4940.

(4) Hall, K. F.; Boggio-Pasqua, M.; Bearpark, M. J.; Robb, M. A. *J. Phys. Chem. A* **2006**, *110*, 13591.

(5) Shine, H. J.; Zhao, D. C. *J. Org. Chem.* **1990**, *55*, 4086.

(6) Ishida, A.; Fukui, M.; Ogawa, H.; Tojo, S.; Majima, T.; Takamuku, S. *J. Phys. Chem.* **1995**, *99*, 10808.

(7) Huang, Y.; Hopkins, J. B. *J. Phys. Chem.* **1996**, *100*, 9585.

(8) Ichinose, N.; Majima, T. *Chem. Phys. Lett.* **2000**, *322*, 15.

(9) Ichinose, N.; Tanaka, T.; Kawanishi, S.; Majima, T. *Chem. Phys. Lett.* **2000**, *326*, 293.

(10) Häupl, T.; Lomoth, R.; Hammarström, L. *J. Phys. Chem. A* **2003**, *107*, 435.

(11) Zhao, L.; Lian, R.; Shkrob, I. A.; Crowell, R. A.; Pommeret, S.; Chronister, E. L.; Liu, A. D.; Trifunac, A. D. *J. Phys. Chem. A* **2004**, *108*, 25.

(12) Okhrimenko, A. N.; Gusev, A. V.; Rodgers, M. A. J. *J. Phys. Chem. A* **2005**, *109*, 7653.

(13) Pagès, S.; Lang, B.; Vauthey, E. *J. Phys. Chem. A* **2006**, *110*, 7547.

(14) Sánchez-Carrera, R. S.; Coropceanu, V.; Da Silva Filho, D. A.; Friedlein, R.; Osikowicz, W.; Murdey, R.; Suess, C.; Salaneck, W. R.; Brédas, J. *J. Phys. Chem. B* **2006**, *110*, 18904.

(15) Cai, X.; Sakamoto, M.; Fujitsuka, M.; Majima, T. *Chem. Phys. Lett.* **2006**, *432*, 436.

(16) Samori, S.; Fujitsuka, M.; Majima, T. *J. Phys. Chem. A* **2008**, *112*, 11312.

(17) Amarie, S.; Förster, U.; Gildenhoff, N.; Dreuw, A.; Wachtveitl, J. *Chem. Phys.* **2010**, *373*, 8.

(18) Grilj, J.; Buchgraber, P.; Vauthey, E. *J. Phys. Chem. A* **2012**, *116*, 7516.

(19) Shukla, S. S.; Rusling, J. F. *J. Phys. Chem.* **1985**, *89*, 3353.

(20) Compton, R. G.; Eklund, J. C.; Fisher, A. C.; Waller, A. M. *J. Chem. Soc. Faraday Trans.* **1990**, *86*, 2951.

(21) Eggins, B. R.; Robertson, P. K. J. *J. Chem. Soc. Faraday Trans.* **1994**, *90*, 2249.

(22) Breslin, D. T.; Fox, M. A. *J. Phys. Chem.* **1994**, *98*, 408.

(23) Fujita, M.; Ishida, A.; Majima, T.; Takamuku, S. *J. Phys. Chem.* **1996**, *100*, 5382.

(24) Majima, T.; Fukui, M.; Ishida, A.; Takamuku, S. *J. Phys. Chem.* **1996**, *100*, 8913.

(25) Cook, A. R.; Curtiss, L. A.; Miller, J. R. *J. Am. Chem. Soc.* **1997**, *119*, 5729.

(26) Debreczeny, M. P.; Svec, W. A.; Marsh, E. M.; Wasielewski, M. R. *J. Am. Chem. Soc.* **1996**, *118*, 8174.

(27) Gosztola, D.; Niemczyk, M. P.; Svec, W.; Lukas, A. S.; Wasielewski, M. R. *J. Phys. Chem. A* **2000**, *104*, 6545.

(28) Lukas, A. S.; Miller, S. E.; Wasielewski, M. R. *J. Phys. Chem. B* **2000**, *104*, 931.

(29) Lukas, A. S.; Bushard, P. J.; Wasielewski, M. R. *J. Am. Chem. Soc.* **2001**, *123*, 2440.

(30) Gumy, J.; Vauthey, E. *J. Phys. Chem. A* **1997**, *101*, 8575.

(31) Brodard, P.; Sarbach, A.; Gumy, J.; Bally, T.; Vauthey, E. *J. Phys. Chem. A* **2001**, *105*, 6594.

(32) Hope, M. J.; Higlett, M. P.; Andrews, D. L.; Meech, S. R.; Hands, I. D.; Dunn, J. L.; Bates, C. A. *Chem. Phys. Lett.* **2009**, *474*, 112.

(33) Horke, D. A.; Roberts, G. M.; Verlet, J. R. R. *J. Phys. Chem. A* **2011**, *115*, 8369.

(34) Fujitsuka, M.; Kim, S. S.; Lu, C.; Tojo, S.; Majima, T. *J. Phys. Chem. B* **2015**, *119*, 7275.

(35) Fujitsuka, M.; Ohsaka, T.; Majima, T. *Phys. Chem. Chem. Phys.* **2015**, *17*, 31030.

(36) Angadi, M. A.; Gosztola, D.; Wasielewski, M. R. *Mater. Sci. Eng., B* **1999**, *63*, 191.

(37) Briseno, A. L.; Mannsfeld, S. C. B.; Reese, C.; Hancock, J. M.; Xiong, Y.; Jenekhe, S. A.; Bao, Z.; Xia, Y. *Nano Lett.* **2007**, *7*, 2847.

(38) Rajaram, S.; Shivanna, R.; Kandappa, S. K.; Narayan, K. S. *J. Phys. Chem. Lett.* **2012**, *3*, 2405.

(39) Supur, M.; El-Khouly, M. E.; Seok, J. H.; Kim, J. H.; Kay, K.; Fukuzumi, S. *J. Phys. Chem. C* **2010**, *114*, 10969.

(40) Rieth, S.; Li, Z.; Hinkle, C. E.; Guzman, C. X.; Lee, J. J.; Nehme, S. I.; Braunschweig, A. B. *J. Phys. Chem. C* **2013**, *117*, 11347.

(41) Singh, T. B.; Erten, S.; Günes, S.; Zafer, C.; Turkmen, G.; Kuban, B.; Teoman, Y.; Sariciftci, N. S.; Icli, S. *Org. Electron.* **2006**, *7*, 480.

(42) Würthner, F.; Stolte, M. *Chem. Commun.* **2011**, *47*, 5109.

(43) Mackinnon, S. M.; Wang, Z. Y. *J. Polym. Sci., Part A: Polym. Chem.* **2000**, *38*, 3467.

(44) Fujitsuka, M.; Cho, D. W.; Tojo, S.; Inoue, A.; Shiragami, T.; Yasuda, M.; Majima, T. *J. Phys. Chem. A* **2007**, *111*, 10574.

(45) Frisch, M. J.; Trucks, G. W.; Schlegel, H. B.; Scuseria, G. E.; Robb, M. A.; Cheeseman, J. R.; Scalmani, G.; Barone, V.; Mennucci, B.; Petersson, G. A.; Nakatsuji, H.; Caricato, M.; Li, X.; Hratchian, H. P.; Izmaylov, A. F.; Bloino, J.; Zheng, G.; Sonnenberg, J. L.; Hada, M.; Ehara, M.; Toyota, K.; Fukuda, R.; Hasegawa, J.; Ishida, M.; Nakajima, T.; Honda, Y.; Kitao, O.; Nakai, H.; Vreven, T.; Montgomery, J. A., Jr.; Peralta, J. E.; Ogliaro, F.; Bearpark, M.; Heyd, J. J.; Brothers, E.; Kudin, K. N.; Staroverov, V. N.; Kobayashi, R.; Normand, J.; Raghavachari, K.; Rendell, A.;

Burant, J. C.; Iyengar, S. S.; Tomasi, J.; Cossi, M.; Rega, N.; Millam, N. J.; Klene, M.; Knox, J. E.; Cross, J. B.; Bakken, V.; Adamo, C.; Jaramillo, J.; Gomperts, R.; Stratmann, R. E.; Yazyev, O.; Austin, A. J.; Cammi, R.; Pomelli, C.; Ochterski, J. W.; Martin, R. L.; Morokuma, K.; Zakrzewski, V. G.; Voth, G. A.; Salvador, P.; Dannenberg, J. J.; Dapprich, S.; Daniels, A. D.; Farkas, Ö.; Foresman, J. B.; Ortiz, J. V.; Cioslowski, J.; Fox, D. J. *Gaussian 09*, Revision C.01; Gaussian, Inc.: Wallingford, CT, 2009.

(46) Fujitsuka, M.; Luo, C.; Ito, O. *J. Phys. Chem. B* **1999**, *103*, 445.

(47) Marcus, R. A. *Annu. Rev. Phys. Chem.* **1964**, *15*, 144.

(48) Marcus, R. A.; Sutin, N. *Biochim. Biophys. Acta* **1985**, *811*, 265.

(49) Marcus, R. A. *Angew. Chem. Int. Ed. Eng.* **1993**, *32*, 1111.

(50) Klimkans, A.; Larsson, S. *Chem. Phys.* **1994**, *189*, 25.

(51) McConnell, H. M. *J. Chem. Phys.* **1961**, *35*, 508.

(52) Paulson, B. P.; Miller, J. R.; Gan, W.; Closs, G. *J. Am. Chem. Soc.* **2005**, *127*, 4860.

(53) Albinsson, B.; Eng, M. P.; Pettersson, K.; Winters, M. U. *Phys. Chem. Chem. Phys.* **2007**, *9*, 5847.

(54) Hwang, I.; Moses, D.; Heeger, A. J. *J. Phys. Chem. C* **2008**, *112*, 4350.

(55) Guo, J.; Ohkita, H.; Benten, H.; Ito, S. *J. Am. Chem. Soc.* **2010**, *132*, 6154.

(56) Heeger, A. J. *J. Phys. Chem. B* **2001**, *105*, 8475.

(57) Da Cunha, W. F.; Ribeiro, L. A.; Fonseca, A. L. D. A.; Gargano, R.; E Silva, G. M. *J. Phys. Chem. C* **2014**, *118*, 23451.

Chapter 2. Intramolecular Electron Transfer from Excited Aromatic Diimide Radical Anion:

Chapter 2-2. Dual Character of Excited Radical Anions in Aromatic Diimide Bis(Radical Anion)s

Abstract

Intramolecular electron transfer (ET) processes in the excited aromatic diimide bis(radical anion)s (ADI$^{\bullet-}$*-ADI'$^{\bullet-}$) were systematically investigated by applying femtosecond laser flash photolysis to bis(radical anion)s of naphthalenediimide (NDI) and perylenediimide (PDI), including NDI$^{\bullet-}$-*m*-NDI$^{\bullet-}$, NDI$^{\bullet-}$-*p*-NDI$^{\bullet-}$, PDI$^{\bullet-}$-*m*-PDI$^{\bullet-}$, and NDI$^{\bullet-}$-*m*-PDI$^{\bullet-}$ (*m* and *p* indicate the substitution positions). The excitation of NDI$^{\bullet-}$-*m*-NDI$^{\bullet-}$ and NDI$^{\bullet-}$-*p*-NDI$^{\bullet-}$ initiated disproportionation reactions generating NDI and NDI^{2-} with different ET rate constants. For the first time, the dual characteristics of ADI$^{\bullet-}$* were confirmed upon selective excitation of NDI$^{\bullet-}$-*m*-PDI$^{\bullet-}$: NDI$^{\bullet-}$* was unambiguously demonstrated to function as an electron donor in NDI$^{\bullet-}$*-*m*-PDI$^{\bullet-}$, whereas PDI$^{\bullet-}$* acted as an electron acceptor in NDI$^{\bullet-}$-*m*-PDI$^{\bullet-}$* because of the energetically preferable production of NDI-*m*-PDI^{2-}. The relationship between the ET rate constants and driving forces in ADI$^{\bullet-}$*-ADI'$^{\bullet-}$ could be reasonably analyzed using the Marcus theory. The current findings provided a new viewpoint regarding the bipolaron-generating nature of ADI$^{\bullet-}$*-ADI'$^{\bullet-}$ and simulated various types of photocarrier migration in the densely charged regions of homo- and heterogeneous n-type semiconductor materials upon irradiation.

Introduction

Aromatic diimides (ADIs), especially naphthalenediimide (NDI) and perylenediimide (PDI), are among the most widely explored components for n-type semiconductor materials in organic field-effect transistors (OFETs), organic light-emitting diodes (OLEDs), and organic solar cells (OSCs).[1-6] This is because of their remarkable properties such as ease of reduction, good charge mobility, excellent thermal stability, and high molar absorptivity. Recently, a new series of co-polymers containing both NDI and PDI was designed as the electron acceptors for bulk heterojunction OSCs, and the efficiency (e.g., carrier mobility) of solar cells was found to vary substantially with the NDI/PDI composition.[7,8] In addition, it is worth mentioning that NDI and PDI can be reduced stepwise in two phases: first producing radical anions, followed by dianions.[9] Therefore, the reduced NDI and PDI as photocarriers including not only polarons ($NDI^{\bullet-}$ and $PDI^{\bullet-}$) but also bipolarons (NDI^{2-} and PDI^{2-}) are closely related to the electronic and optical performance of ADI-based materials, although studies focusing on bipolaron-generation mechanisms and dynamics are extremely limited.

On the other hand, excited radical ions with powerful redox ability have attracted increasing attention.[10-18] $NDI^{\bullet-}$ and $PDI^{\bullet-}$ in the excited states ($NDI^{\bullet-}$* and $PDI^{\bullet-}$*) are stronger reductants than their ground-state counterparts. Wasielewski and his co-workers first reported the transient absorption features of excited ADI radical anions with lifetimes of up to a few hundreds of picoseconds, long enough to initiate various chemical reactions.[11] Recently, our research group further elucidated the detailed characteristics of intramolecular electron transfer (ET) from $NDI^{\bullet-}$* and $PDI^{\bullet-}$* by applying femtosecond laser flash photolysis to several purposely reduced dyads.[15,17] In particular, we examined photoinduced ET in a stepwise reduced PDI-PDI dimer (i.e., $PDI^{\bullet-}$-PDI or $PDI^{\bullet-}$-$PDI^{\bullet-}$); surprisingly, an intramolecular disproportionation producing PDI and PDI^{2-} was observed upon excitation of $PDI^{\bullet-}$-$PDI^{\bullet-}$.[17] Considering the roles of the densely populated charges in homo- and heterogeneous organic conductors, the generation of bipolarons via the irradiation of concentrated polarons should be regarded as an important process. Nevertheless, several puzzles (e.g., the driving force, spatial distance, and excitation wavelength dependences) remain to be solved for understanding the related processes in polymeric and crystalline structures.

Thus, in this study, NDI, PDI, NDI-*m*-NDI, NDI-*p*-NDI, PDI-*m*-PDI, and NDI-*m*-PDI (*m* and *p* indicate the substitution positions) were prepared as target molecules (Scheme 2-2-1). 2-Ethylhexyl and tridecan-7-yl groups were introduced to ensure substantial solubility in organic solvents. Additionally, a phenyl (or 2,5-dimethylphenyl) group was used as a spacer to realize a fixed donor-acceptor distance and minimize the π-conjugation with NDI or PDI due to the perpendicular conformation caused by steric effect. A systematic investigation was conducted to clarify the bipolaron-generating nature of ADI$^{\bullet-}$*-ADI'$^{\bullet-}$ in various organic molecular devices.

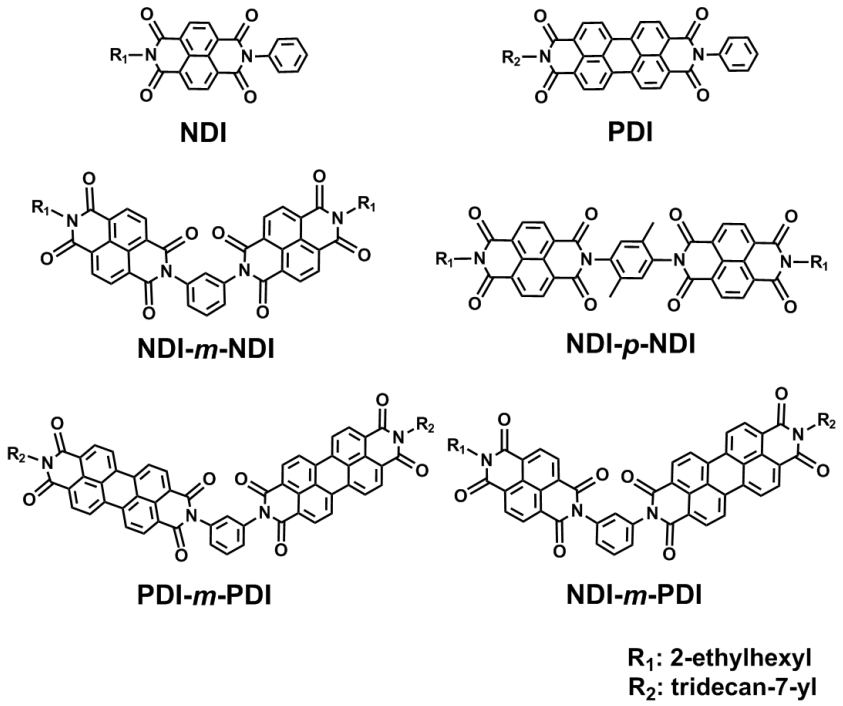

Scheme 2-2-1. Chemical structures of NDI, PDI, NDI-*m*-NDI, NDI-*p*-NDI, PDI-*m*-PDI, and NDI-*m*-PDI.

Experimental Section

Synthesis.

N-(2-Ethylhexyl)naphthalenetetracarboxylic monoanhydride monoimide (1)

In a single-neck round-bottom flask equipped with a reflux condenser, 1,4,5,8-naphthalene-tetracarboxylic dianhydride (6.18 g, 23.04 mmol) was suspended in 80 mL of DMF, and the

solution was stirred at 80 ℃. To this solution 2-ethyl-1-hexylamine (2.98 g, 23.06 mmol) was added drop wise over a period of 1 h and the mixture was heated to 120 ℃ under argon atmosphere. After 24 hours, the reaction mixture was cooled to room temperature and the precipitated diimide were filtered off. DMF was evaporated under reduced pressure. The crude material was purified by column chromatography (silica gel; dichloromethane) to obtain the pale yellow solid **1** (4.09 g, 10.78 mmol, 47%).

^{1}H NMR ($CDCl_3$, 400 MHz): δ 0.87 (t, J = 6.9 Hz, 3H), 0.92 (t, J = 7.3 Hz, 3H), 1.30 (m, 8H), 1.90 (m, 1H), 4.10 (m, 2H), 8.76 (m, 4H).

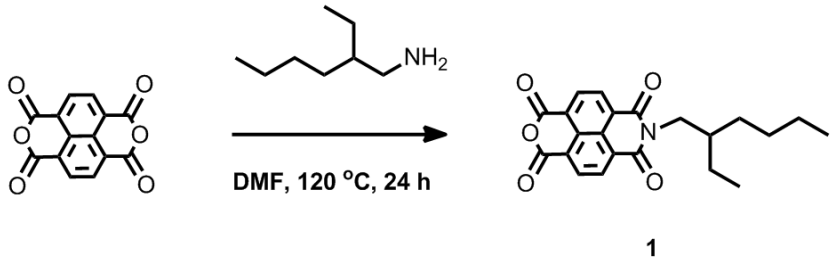

Scheme 2-2-2. Synthesis of **1**.

NDI

1 (0.33 g, 0.87 mmol) and aniline (0.24 g, 2.58 mmol) were dissolved in 50 mL of DMF. The reaction mixture was heated with stirring to reflux for 24 h under argon atmosphere. Afterwards the reaction mixture was evaporated in vacuo and further purified by column chromatography (silica gel; dichloromethane) to obtain the pale yellow solid **NDI** (0.20 g, 0.44 mmol, 51%).

^{1}H NMR ($CDCl_3$, 400 MHz): δ 0.87 (t, J = 7.3 Hz, 3H), 0.94 (t, J = 7.8 Hz, 3H), 1.31 (m, 8H), 1.93 (m, 1H), 4.12 (m, 2H), 7.32 (m, 2H), 7.51 (m, 3H), 8.81 (m, 4H).

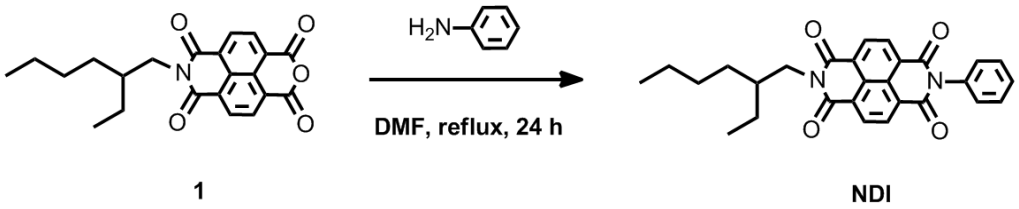

Scheme 2-2-3. Synthesis of **NDI**.

NDI-*m*-NDI

1 (0.61 g, 1.61 mmol) and *m*-phenylenediamine (0.09 g, 0.83 mmol) were dissolved in 50 mL of DMF. The reaction mixture was heated with stirring to reflux for 24 h under argon atmosphere. Afterwards the reaction mixture was evaporated in vacuo and purified by column chromatography (silica gel; chloroform and then chloroform/ethyl acetate (gradient)). Further purification was carried by column chromatography (silica gel; dichloromethane and then dichloromethane/ethyl acetate (gradient)) to obtain the pale yellow solid **NDI-*m*-NDI** (30 mg, 0.04 mmol, 5%).

^{1}H NMR ($CDCl_3$, 400 MHz): δ 0.87 (t, J = 7.3 Hz, 6H), 0.93 (t, J = 7.8 Hz, 6H), 1.31 (m, 16H), 1.94 (m, 2H), 4.11 (m, 4H), 7.39 (m, 1H), 7.51 (m, 2H), 7.77 (m, 1H), 8.79 (m, 8H). FAB MS: calcd. 830.33, found 831 (M+1).

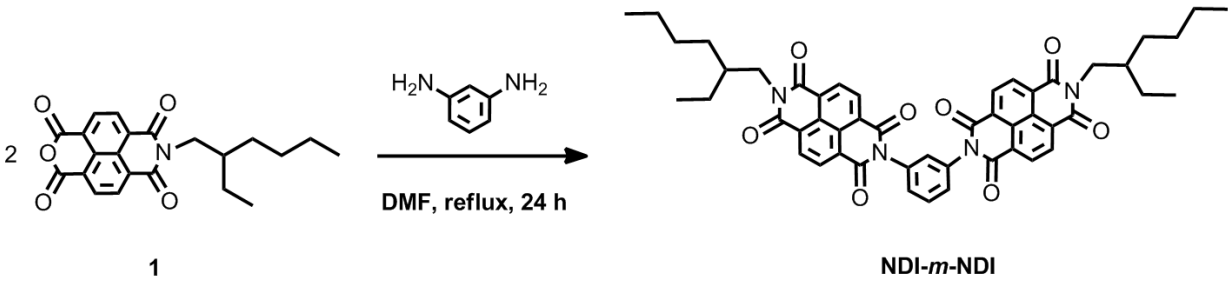

Scheme 2-2-4. Synthesis of **NDI-*m*-NDI**.

NDI-*p*-NDI

1 (0.89 g, 2.35 mmol) and 2,5-dimethylbenzene-1,4-diamine (0.16 g, 1.17 mmol) were dissolved in 50 mL of DMF. The reaction mixture was heated with stirring to reflux for 24 h under argon atmosphere. Afterwards the reaction mixture was evaporated in vacuo and purified by column chromatography (silica gel; chloroform and then chloroform/ethyl acetate (gradient)). Further purification was carried by column chromatography (silica gel; dichloromethane and then dichloromethane/ethyl acetate (gradient)) to obtain the pale yellow solid **NDI-*p*-NDI** (50 mg, 0.06 mmol, 5%).

^{1}H NMR (CF_3COOH, 400 MHz): δ 0.85 (t, J = 7.1 Hz, 6H), 0.95 (t, J = 7.3 Hz, 6H), 1.28 (m, 16H), 2.03 (m, 2H), 2.23 (m, 6H), 4.32 (m, 4H), 7.43 (m, 2H), 8.98 (m, 8H). FAB MS: calcd. 858.36, found 859 (M+1).

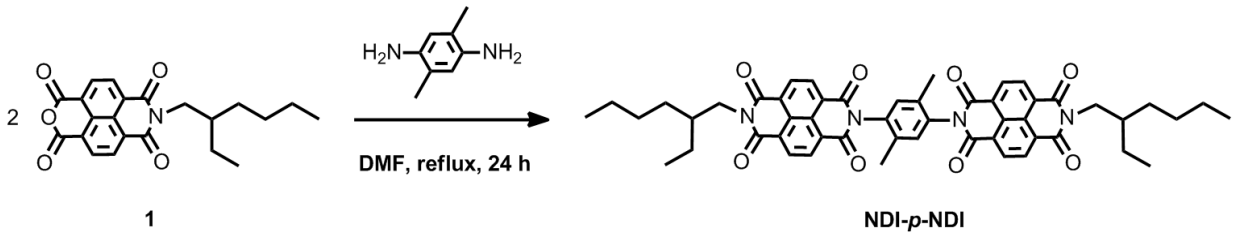

Scheme 2-2-5. Synthesis of **NDI-*p*-NDI**.

Materials. PDI, PDI-*m*-PDI, and NDI-*m*-PDI were synthesized as reported in our previous work.[17] The synthesis procedures for NDI, NDI-*m*-NDI, and NDI-*p*-NDI are summarized in the above part. In the present study, *N*,*N*-dimethylformamide (DMF) was used as the solvent for all spectroscopic measurements. Tetrakis(dimethylamino)ethylene (TDAE) was purchased from Tokyo Chemical Industry.

Apparatus. Steady-state absorption spectra were measured using a Shimadzu UV-3600 UV-vis-NIR spectrometer. Transient absorption spectra during femtosecond laser flash photolysis were measured as described previously.[19] In this study, the samples were excited by a 475 or 700 nm femtosecond laser pulse (~130 fs fwhm, ~5 μJ per pulse).

Results and Discussion

Figure 2-2-1 shows the steady-state absorption spectra of NDI-*m*-PDI in DMF with varying concentrations of TDAE. The features of neutral NDI and PDI were simultaneously observed in the absorption spectrum of NDI-*m*-PDI. When TDAE was added as a reducing agent,[20] the absorbance of NDI and PDI decreased and a new set of bands attributable to $PDI^{\bullet-}$ appeared with the maximum occurring at 700 nm. As the TDAE concentration increased, a growing peak was clearly observed at 475 nm. This can be attributed to the generation of $NDI^{\bullet-}$ because of the similar reduction potentials of NDI and PDI (−0.48 and −0.43 V vs. SCE, respectively).[11] The absorbance of $NDI^{\bullet-}$ and $PDI^{\bullet-}$ reached their maxima with a two-equivalent addition of TDAE, indicating the quantitative reduction of NDI-*m*-PDI. The band intensity of $NDI^{\bullet-}$-*m*-$PDI^{\bullet-}$ was maintained for several hours after removing the oxygen from the solvent by Ar bubbling. We noted that the spectral features of $NDI^{\bullet-}$ and $PDI^{\bullet-}$ in $NDI^{\bullet-}$-*m*-$PDI^{\bullet-}$ were essentially the same as those of the monomeric species,[11] suggesting that negligible interactions existed. Most importantly, the selective excitation of the $NDI^{\bullet-}$ and $PDI^{\bullet-}$ moieties in this heterodimer could be achieved at 475 and 700 nm, respectively. As for the other target molecules including NDI, PDI, NDI-*m*-NDI, NDI-*p*-NDI, and PDI-*m*-PDI, one or two equivalents of TDAE were added to prepare the radical anion or bis(radical anion), respectively.

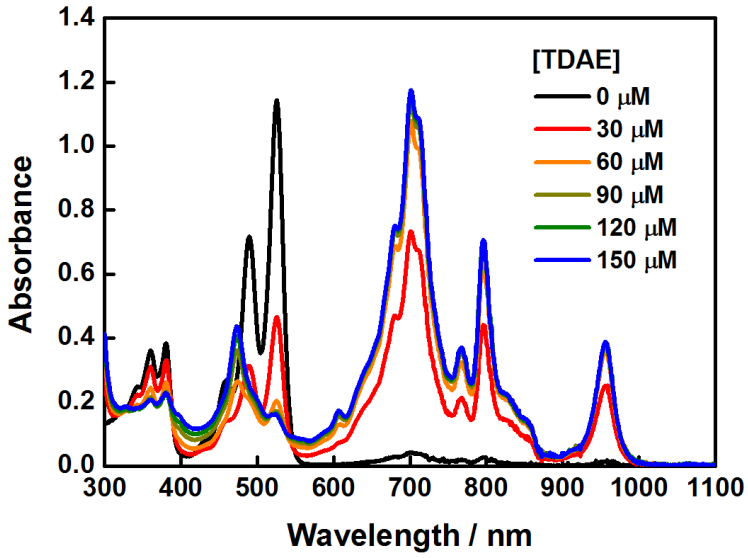

Figure 2-2-1. Steady-state absorption spectra of NDI-*m*-PDI (75 μM) in DMF with varied concentrations of TDAE (0−150 μM).

Figure 2-2-2a shows the transient absorption spectra of $NDI^{\bullet-}$ measured during laser flash photolysis using a 475 nm femtosecond laser. The spectrum taken 6 ps after laser excitation showed both positive and negative signals, indicating the generation of $NDI^{\bullet-}$* and the bleaching of $NDI^{\bullet-}$, respectively. With an increase in the delay time, the positive signals showed a decrease whereas the negative signals showed a recovery. This phenomenon is attributed to the $D_1 \rightarrow D_0$ deactivation process of $NDI^{\bullet-}$ with a lifetime of 112 ps ($8.9 \times 10^9\ s^{-1}$), which can be obtained by fitting a single exponential function to the decay kinetics of ΔO.D. at 650 nm (Figure 2-2-2b).

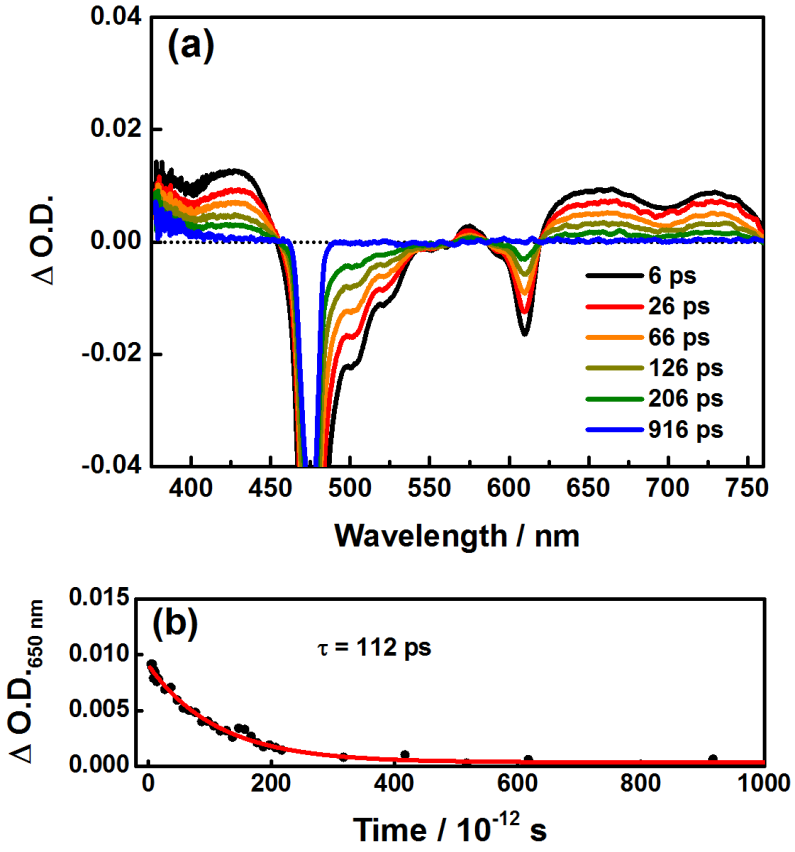

Figure 2-2-2. (a) Transient absorption spectra of NDI (0.20 mM) in DMF in the presence of TDAE (0.20 mM) during a 475 nm femtosecond laser excitation and (b) kinetic trace of ΔO.D. at 650 nm.

Figure 2-2-3a shows the transient absorption spectra of $NDI^{\bullet-}$-*m*-$NDI^{\bullet-}$ measured during laser flash photolysis using a 475 nm femtosecond laser. The spectrum taken 4 ps after laser excitation indicated the generation of $NDI^{\bullet-}$*-*m*-$NDI^{\bullet-}$. Meanwhile, sharp absorption peaks appeared at 385 nm (NDI) and 425 nm (NDI^{2-}) due to the generation of NDI-*m*-NDI^{2-}, suggesting an intramolecular ET process, as described in eq 2-2-1.

$$NDI^{\bullet-}\text{*-}m\text{-}NDI^{\bullet-} \xrightarrow{k_{intraET}} NDI\text{-}m\text{-}NDI^{2-} \quad (2\text{-}2\text{-}1)$$

Thus, a disproportionation reaction was confirmed to occur upon excitation of $NDI^{\bullet-}$-*m*-$NDI^{\bullet-}$. By analyzing the kinetic trace of ΔO.D. at 650 nm (Figure 2-2-3b) and taking the $D_1 \rightarrow D_0$ deactivation process into account, the intramolecular ET rate constant ($k_{intraET}$) was calculated to be 1.3×10^{11} s^{-1}. With further increase in the delay time, the positive bands decreased continuously, whereas the negative bands showed a recovery, suggesting a back ET (BET) process, as described in eq 2-2-2.

$$NDI\text{-}m\text{-}NDI^{2-} \xrightarrow{k_{intraBET}} NDI^{\bullet-}\text{-}m\text{-}NDI^{\bullet-} \quad (2\text{-}2\text{-}2)$$

The intramolecular BET rate constant ($k_{intraBET}$) was estimated to be 1.1×10^{10} s^{-1} based on the decay of NDI-*m*-NDI^{2-} (Figure 2-2-3c). Similar phenomena were also observed upon excitation of $NDI^{\bullet-}$-*p*-$NDI^{\bullet-}$ (Figures 2-2-3d,e). Compared to $NDI^{\bullet-}$*-*m*-$NDI^{\bullet-}$, $NDI^{\bullet-}$*-*p*-$NDI^{\bullet-}$ exhibited a slower ET with a $k_{intraET}$ of 8.3×10^{10} s^{-1}, and the generated NDI-*p*-NDI^{2-} showed BET that did not complete within the instrumental time window. These results indicate that the spatial distance between chromophores does have an effect on the ET processes initiated by excited bis(radical anion)s.

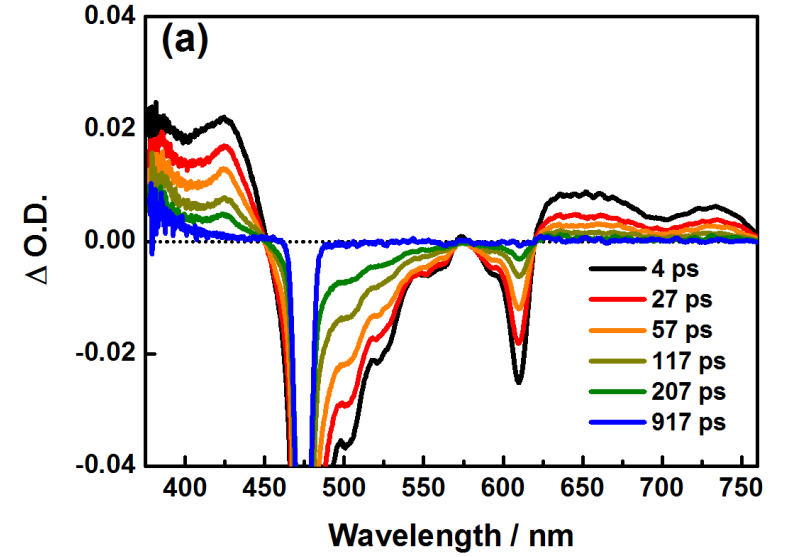
(a)
0.04
0.02
0.00
-0.02
-0.04
Δ O.D.
400
450
500
550
600
650
700
750
Wavelength / nm
4 ps
27 ps
57 ps
117 ps
207 ps
917 ps

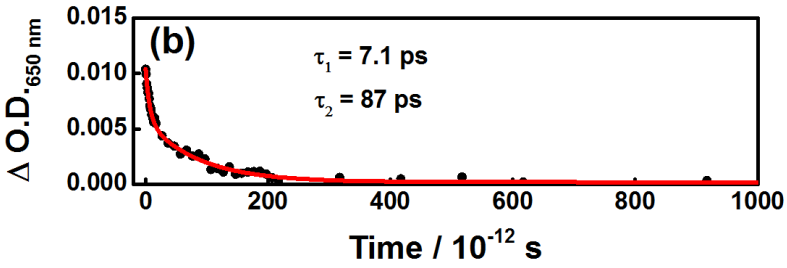
(b)
Δ O.D.650 nm
0.015
0.010
0.005
0.000
τ1 = 7.1 ps
τ2 = 87 ps
0
200
400
600
800
1000
Time / 10-12 s

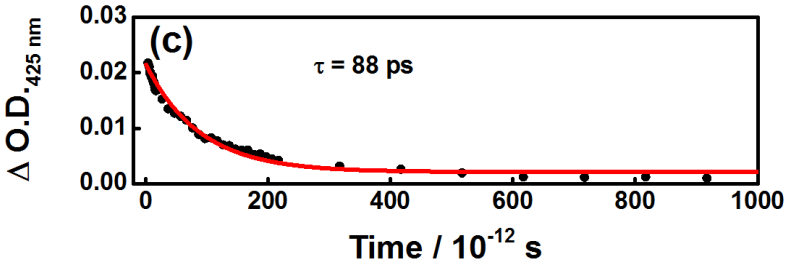
(c)
Δ O.D.425 nm
0.03
0.02
0.01
0.00
τ = 88 ps
0
200
400
600
800
1000
Time / 10-12 s

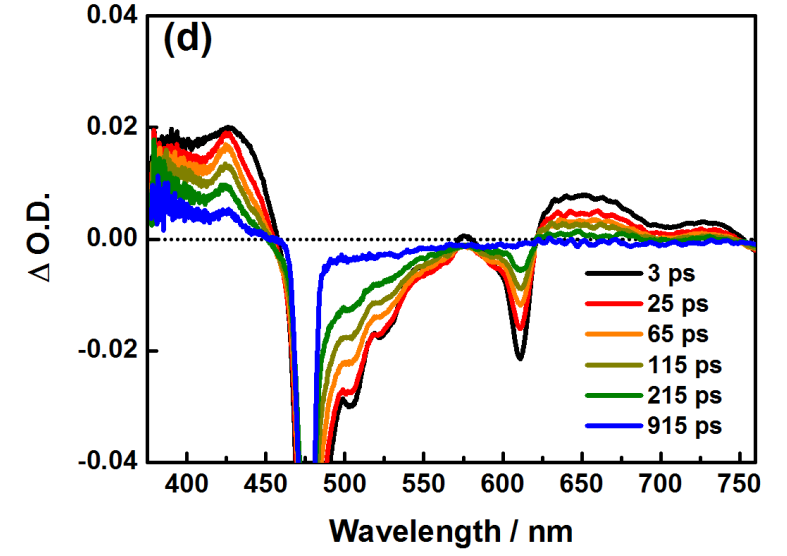
(d)
0.04
0.02
0.00
-0.02
-0.04
Δ O.D.
400
450
500
550
600
650
700
750
Wavelength / nm
3 ps
25 ps
65 ps
115 ps
215 ps
915 ps

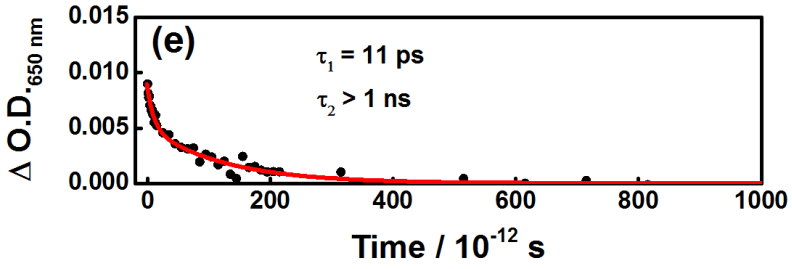

Figure 2-2-3. (a) Transient absorption spectra of NDI-*m*-NDI (0.20 mM) in DMF in the presence of TDAE (0.40 mM) during a 475 nm femtosecond laser excitation and (b,c) kinetic traces of ΔO.D. at 650 and 425 nm. (d) Transient absorption spectra of NDI-*p*-NDI (0.20 mM) in DMF in the presence of TDAE (0.40 mM) during a 475 nm femtosecond laser excitation and (e) kinetic trace of ΔO.D. at 650 nm.

Figure 2-2-4a shows the transient absorption spectra of $NDI^{\bullet-}$-*m*-$PDI^{\bullet-}$ measured during laser flash photolysis using a 475 nm femtosecond laser. The spectrum taken 2 ps after laser excitation indicated the generation of $NDI^{\bullet-}$*-*m*-$PDI^{\bullet-}$. The most significant positive peak due to PDI^{2-} was detected at 575 nm with a $k_{intraET}$ of 3.3×10^{11} s^{-1} (Figure 2-2-4b), suggesting a process indicated in eq 2-2-3.

$$NDI^{\bullet-}\text{*-}m\text{-}PDI^{\bullet-} \xrightarrow{k_{intraET}} NDI\text{-}m\text{-}PDI^{2-} \quad (2\text{-}2\text{-}3)$$

Unambiguously, $NDI^{\bullet-}$* acted as an electron donor in this reaction. On the other hand, Figure 2-2-4c shows the transient absorption spectra of $NDI^{\bullet-}$-*m*-$PDI^{\bullet-}$ upon 700 nm laser excitation. The spectrum taken 2 ps after the laser excitation exhibited positive bands with the greatest intensity at 460 nm, which are attributable to $PDI^{\bullet-}$*. By increasing the delay time, the 575 nm-maximized signals appeared in the spectra, suggesting the production of NDI-*m*-PDI^{2-} indicated in eq 2-2-4.

$$NDI^{\bullet-}\text{-}m\text{-}PDI^{\bullet-}\text{*} \xrightarrow{k_{intraET}} NDI\text{-}m\text{-}PDI^{2-} \quad (2\text{-}2\text{-}4)$$

Surprisingly, here, the excited radical anion ($PDI^{\bullet-}$*) was found to be an electron acceptor. The $k_{intraET}$ of this process was calculated to be 1.8×10^9 s^{-1} by considering the $D_1 \rightarrow D_0$ deactivation of $PDI^{\bullet-}$* at 460 nm (Figure 2-2-4d).[17] The entire BET processes could not be traced for either $NDI^{\bullet-}$*-*m*-$PDI^{\bullet-}$ or $NDI^{\bullet-}$-*m*-$PDI^{\bullet-}$*, owing to instrumental limitation.

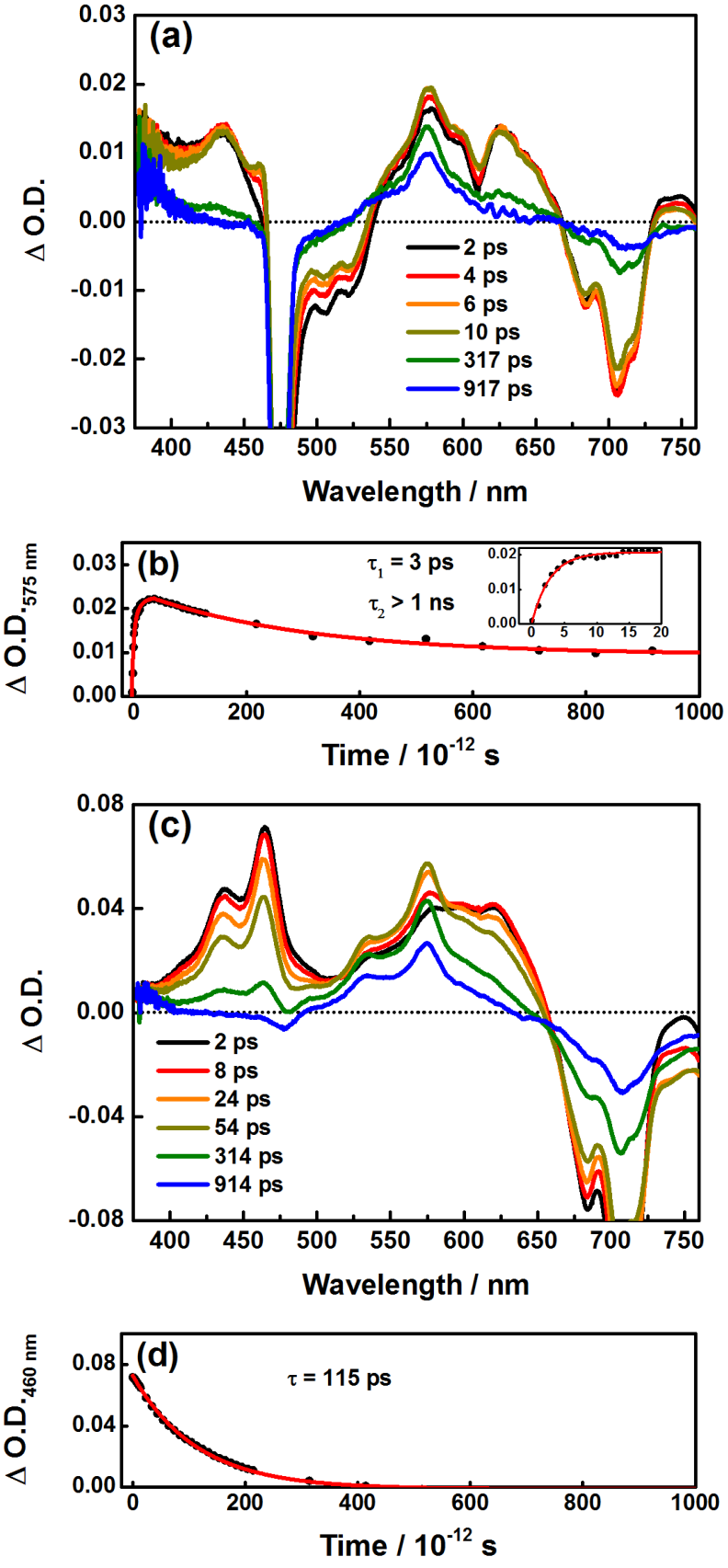
(a)
Δ O.D.
Wavelength / nm
2 ps
4 ps
6 ps
10 ps
317 ps
917 ps
(b)
Δ O.D.575 nm
τ1 = 3 ps
τ2 > 1 ns
Time / 10-12 s
(c)
Δ O.D.
Wavelength / nm
2 ps
8 ps
24 ps
54 ps
314 ps
914 ps
(d)
Δ O.D.460 nm
τ = 115 ps
Time / 10-12 s

Figure 2-2-4. (a) Transient absorption spectra of NDI-*m*-PDI (0.20 mM) in DMF in the presence of TDAE (0.40 mM) during a 475 nm femtosecond laser excitation and (b) kinetic trace of ΔO.D. at 575 nm. (Inset: enlarged kinetic trace within 20 ps.) (c) Transient absorption spectra of NDI-*m*-PDI (0.12 mM) in DMF in the presence of TDAE (0.24 mM) during a 700 nm femtosecond laser excitation and (d) kinetic trace of ΔO.D. at 460 nm.

Scheme 2-2-6 shows the molecular orbital diagrams for the intramolecular ET processes upon excitation of $NDI^{\bullet-}$-electron acceptor (A), $NDI^{\bullet-}$-$NDI^{\bullet-}$, and $NDI^{\bullet-}$-$PDI^{\bullet-}$. Generally, a radical anion has a single electron in its highest occupied molecular orbital (HOMO = SOMO), corresponding to the lowest unoccupied molecular orbital (LUMO) of its neutral state. In the case of $NDI^{\bullet-}$*-A, one electron is excited from the HOMO-1 to HOMO (SOMO) of $NDI^{\bullet-}$, and then moves to the LUMO of A (Scheme 2-2-6a). Here, the excited radical anion acts solely as an electron donor, which is consistent with all the previous reports.[10-18] However, when it comes to the case of $NDI^{\bullet-}$*-$NDI^{\bullet-}$, the role of the excited radical anion (electron donor or acceptor) is difficult to be determined because injecting the excited electron of $NDI^{\bullet-}$* into the SOMO of the counter $NDI^{\bullet-}$ and receiving the SOMO electron from $NDI^{\bullet-}$ at the HOMO-1 of $NDI^{\bullet-}$* are both energetically possible pathways (Scheme 2-2-6b). Such duality was clearly confirmed upon selective $NDI^{\bullet-}$ and $PDI^{\bullet-}$ excitation of $NDI^{\bullet-}$-$PDI^{\bullet-}$ (Scheme 2-2-6c). In the particular case of $NDI^{\bullet-}$-$PDI^{\bullet-}$*, $PDI^{\bullet-}$* worked as an electron acceptor and NDI-PDI^{2-} was preferably generated because of the lower second reduction potential of PDI (−0.70 V vs. SCE) than that of NDI (−0.99 V vs. SCE).[11] Thus, for the first time, excited radical anion was proved to be not only an electron donor but also an electron acceptor by applying femtosecond laser flash photolysis to the bis(radical anion) of an ADI heterodimer.

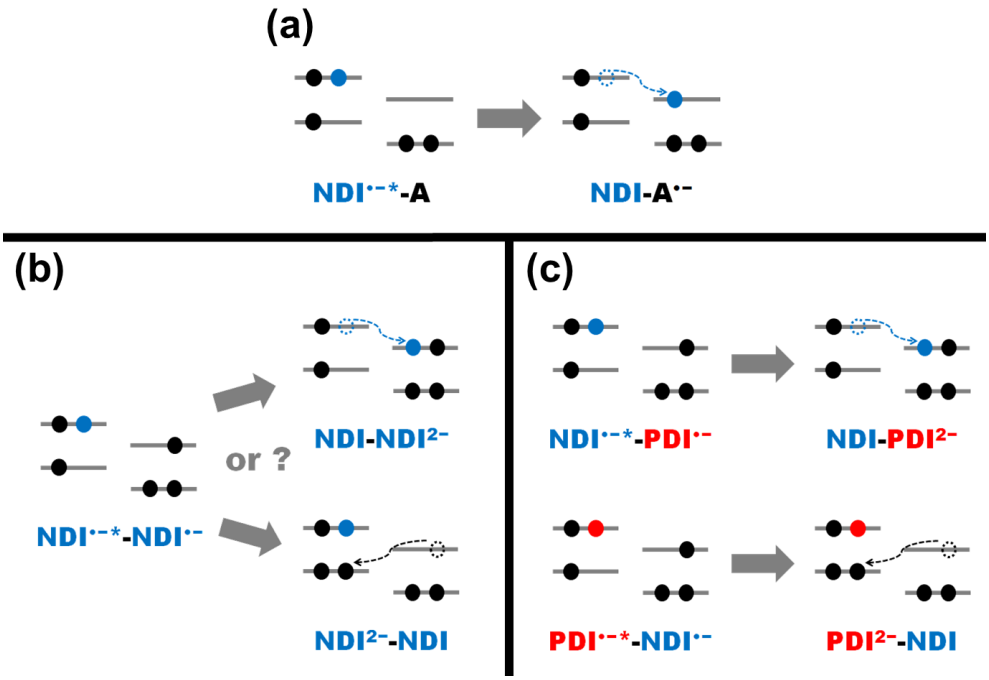

Scheme 2-2-6. Molecular orbital diagrams for the ET processes in (a) $NDI^{\bullet-}$*-A, (b) $NDI^{\bullet-}$*-$NDI^{\bullet-}$, and (c) $NDI^{\bullet-}$*-$PDI^{\bullet-}$ and $NDI^{\bullet-}$-$PDI^{\bullet-}$*.

The rate constants (k_{ET}) and driving forces ($-\Delta G_{ET}$) for the ET processes in $ADI^{\bullet-}$*-$ADI'^{\bullet-}$ are summarized in Table 2-2-1. The $-\Delta G_{ET}$ values for intramolecular ET and BET ($-\Delta G_{intraET}$ and $-\Delta G_{intraBET}$, respectively) were calculated according to eqs 2-2-(5-10).

In the case of $NDI^{\bullet-}$*-$NDI^{\bullet-}$ or $PDI^{\bullet-}$*-$PDI^{\bullet-}$:

$$\Delta G_{intraET} = E(ADI^{\bullet-}/ADI) - E(ADI^{2-}/ADI^{\bullet-}) - E_{D1}(ADI^{\bullet-}*) \quad (2\text{-}2\text{-}5)$$

$$\Delta G_{intraBET} = E(ADI^{2-}/ADI^{\bullet-}) - E(ADI^{\bullet-}/ADI) \quad (2\text{-}2\text{-}6)$$

In the case of $NDI^{\bullet-}$*-$PDI^{\bullet-}$:

$$\Delta G_{intraET} = E(NDI^{\bullet-}/NDI) - E(PDI^{2-}/PDI^{\bullet-}) - E_{D1}(NDI^{\bullet-}*) \quad (2\text{-}2\text{-}7)$$

$$\Delta G_{intraBET} = E(PDI^{2-}/PDI^{\bullet-}) - E(NDI^{\bullet-}/NDI) \quad (2\text{-}2\text{-}8)$$

In the case of $NDI^{\bullet-}$-$PDI^{\bullet-}$*:

$$\Delta G_{intraET} = E(PDI^{\bullet-}/PDI) - E(PDI^{2-}/PDI^{\bullet-}) - E_{D1}(PDI^{\bullet-}*) \quad (2\text{-}2\text{-}9)$$

$$\Delta G_{intraBET} = E(PDI^{2-}/PDI^{\bullet-}) - E(PDI^{\bullet-}/PDI) \quad (2\text{-}2\text{-}10)$$

where $E(ADI^{\bullet-}/ADI)$, $E(ADI^{2-}/ADI^{\bullet-})$, and $E_{D1}(ADI^{\bullet-}*)$ represent the reduction potentials of ADI and $ADI^{\bullet-}$ and the D_1 state energy of $ADI^{\bullet-}$*, respectively. In particular, the values of

E(NDI$^{\bullet-}$/NDI), E(NDI^{2-}/NDI$^{\bullet-}$), E(PDI$^{\bullet-}$/PDI), and E(PDI^{2-}/PDI$^{\bullet-}$) were applied as −0.48, −0.99, −0.43, and −0.70 V vs. SCE, respectively.[11] Due to the $D_1 \leftarrow D_0$ absorption bands of NDI$^{\bullet-}$ and PDI$^{\bullet-}$ at 770 and 955 nm, respectively,[11] the following values were used for E_{D1}(NDI$^{\bullet-}$*) and E_{D1}(PDI$^{\bullet-}$*): 1.61 and 1.30 eV, respectively. As shown in Table 2-2-1, the values of $-\Delta G_{intraET}$ for NDI$^{\bullet-}$*-*m*-NDI$^{\bullet-}$, PDI$^{\bullet-}$*-*m*-PDI$^{\bullet-}$, NDI$^{\bullet-}$*-*m*-PDI$^{\bullet-}$, and NDI$^{\bullet-}$-*m*-PDI$^{\bullet-}$* were calculated to be 1.10, 1.03, 1.39, and 1.03 eV, respectively. In these dyads, efficient ET processes were detected, and the $k_{intraET}$ values tended to increase as the $-\Delta G_{intraET}$ values increased. Figure 2-2-5 shows the relationship between the $-\Delta G_{ET}$ and k_{ET} in ADI$^{\bullet-}$*-A determined previously using the Marcus theory (weak-colored squares).[17] We further plotted the data (strong-colored circles) obtained from the ET processes initiated by ADI$^{\bullet-}$*-ADI'$^{\bullet-}$. The $-\Delta G_{ET}$ dependence of k_{ET} observed in the present study can be reasonably explained by the same Marcus parabola in the normal region.[21-23] The difference between the k_{ET} values from NDI$^{\bullet-}$* and PDI$^{\bullet-}$* is attributable to the energy required to form the reduced spacer and the distance between the electron donor and acceptor.[17]

Table 2-2-1. Estimated Rate Constants (k_{ET}) and Driving Forces ($-\Delta G_{ET}$) for Intramolecular ET in ADI$^{\bullet-}$*-ADI'$^{\bullet-}$.

	$k_{intraET}$[a] (s^{-1})	$-\Delta G_{intraET}$ (eV)	$k_{intraBET}$[a] (s^{-1})	$-\Delta G_{intraBET}$ (eV)
NDI$^{\bullet-}$*-*m*-NDI$^{\bullet-}$	1.3×10^{11}	1.10	1.1×10^{10}	0.51
PDI$^{\bullet-}$*-*m*-PDI$^{\bullet-}$	2.4×10^{9}	1.03	$< 1 \times 10^{9}$	0.27
NDI$^{\bullet-}$*-*m*-PDI$^{\bullet-}$	3.3×10^{11}	1.39	$< 1 \times 10^{9}$	0.22
NDI$^{\bullet-}$-*m*-PDI$^{\bullet-}$*	1.8×10^{9}	1.03	$< 1 \times 10^{9}$	0.27

[a]Estimation error: < 10%.

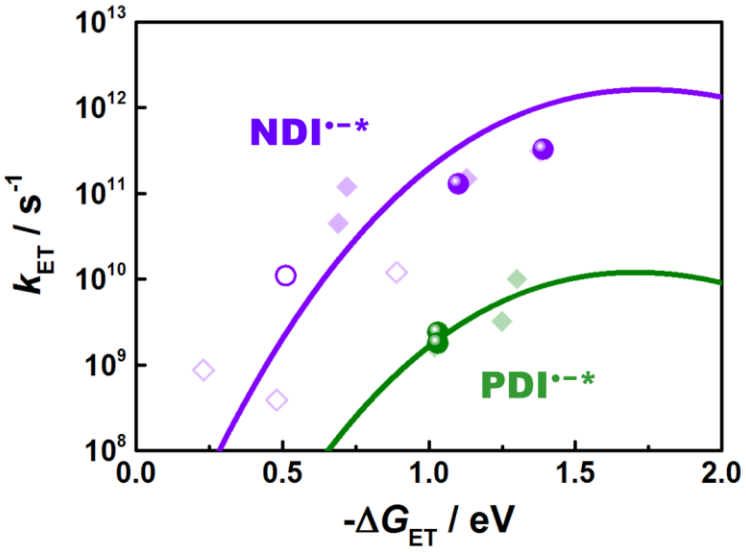

Figure 2-2-5. Relationship between $-\Delta G_{ET}$ and k_{ET} in the dyads of ADI$^{\bullet-}$*. The weak-colored solid and hollow squares correspond to ET and BET, respectively in ADI$^{\bullet-}$*-A. The strong-colored solid and hollow circles correspond to ET and BET, respectively in ADI$^{\bullet-}$*-ADI'$^{\bullet-}$.

Since the ADI dyads can be treated as the simplest units of related polymeric or crystalline materials, it is worth noting that the ET processes exhibited by ADI$^{\bullet-}$*-ADI'$^{\bullet-}$ provide valuable information relating to the generation of bipolarons in the densely charged regions of organic semiconductors upon irradiation.[24-26] Considering the intramolecular ET and subsequent BET detected in NDI$^{\bullet-}$*-NDI$^{\bullet-}$, PDI$^{\bullet-}$*-PDI$^{\bullet-}$, NDI$^{\bullet-}$*-PDI$^{\bullet-}$, and NDI$^{\bullet-}$-PDI$^{\bullet-}$*, several migration routes of photocarriers (e.g., NDI$^{\bullet-}$* $\overset{ET}{\rightarrow}$ NDI$^{\bullet-}$ $\overset{ET}{\rightarrow}$ NDI, NDI$^{\bullet-}$* $\overset{ET}{\rightarrow}$ PDI$^{\bullet-}$ $\overset{ET}{\rightarrow}$ PDI, and NDI$^{\bullet-}$ $\overset{ET}{\rightarrow}$ PDI$^{\bullet-}$* $\overset{ET}{\rightarrow}$ PDI) can be proposed for ADI-based polymers and crystals, which are much more complex than the dyad systems (Scheme 2-2-7). The different $k_{intraET}$ observed in NDI$^{\bullet-}$*-*m*-NDI$^{\bullet-}$ and NDI$^{\bullet-}$*-*p*-NDI$^{\bullet-}$ reflected the effect of spatial distance in a multi-molecular structure, revealing the possibility of additional charge transport. According to the present results, the $k_{intraET}$ obtained from NDI$^{\bullet-}$*-*m*-NDI$^{\bullet-}$ (1.3×10^{11} s^{-1}) or NDI$^{\bullet-}$*-*m*-PDI$^{\bullet-}$ (3.3×10^{11} s^{-1}) was 1-2 orders of magnitude faster than the $D_1 \rightarrow D_0$ deactivation of NDI$^{\bullet-}$* (8.9×10^{9} s^{-1}), indicating the facile formation of a bipolaronic state. Moreover, the photochemical performance of an interface is always an attractive point to be clarified when utilizing co-polymers.[27,28] In the current study, the generation of the same ET products from NDI$^{\bullet-}$*-*m*-PDI$^{\bullet-}$ and NDI$^{\bullet-}$-*m*-PDI$^{\bullet-}$* suggested

that a directional charge transport (from $NDI^{\bullet-}$ to $PDI^{\bullet-}$) occurs at the interface between the charged NDI and PDI regions under photoirradiation. Thus, the above-mentioned findings successfully simulated the unique ET behaviors of the homogeneous NDI/NDI and PDI/PDI, and heterogeneous NDI/PDI components in various organic molecular devices and demonstrated the importance of the pathways from excited bis(radical anion)s.

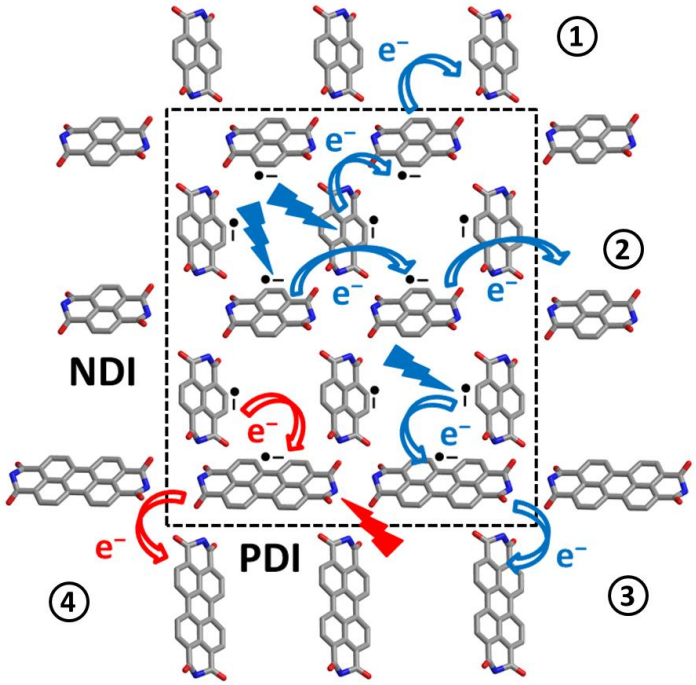

1,2) $NDI^{\bullet-*}$/$NDI^{\bullet-}$/NDI; 3) $NDI^{\bullet-*}$/$PDI^{\bullet-}$/PDI; 4) $NDI^{\bullet-}$/$PDI^{\bullet-*}$/PDI

Scheme 2-2-7. Photocarrier migration in the densely-charged ADI components upon irradiation.

Conclusions

The excited ET in densely charged ADIs was systematically investigated by femtosecond laser flash photolysis using a series of reduced dyads: $NDI^{\bullet-}$-*m*-$NDI^{\bullet-}$, $NDI^{\bullet-}$-*p*-$NDI^{\bullet-}$, $PDI^{\bullet-}$-*m*-$PDI^{\bullet-}$, and $NDI^{\bullet-}$-*m*-$PDI^{\bullet-}$. Different $k_{intraET}$ were observed for the generation of NDI and NDI^{2-} in $NDI^{\bullet-}$*-*m*-$NDI^{\bullet-}$ and $NDI^{\bullet-}$*-*p*-$NDI^{\bullet-}$. Interestingly, the duality of the excited radical anion, which could act as both an electron donor and acceptor, was clearly revealed upon excitation of

the $NDI^{\bullet-}$ and $PDI^{\bullet-}$ moieties in $NDI^{\bullet-}$-$PDI^{\bullet-}$, respectively. By applying the Marcus theory, the relationship between the k_{ET} and $-\Delta G_{ET}$ in $ADI^{\bullet-}$*-$ADI'^{\bullet-}$ could be reasonably explained. The results shown here provided valuable insights into the unique characteristics of $ADI^{\bullet-}$*-$ADI'^{\bullet-}$ as the effective initiators for bipolaron generation in related n-type organic semiconductors.

References

(1) Ego, C.; Marsitzky, D.; Becker, S.; Zhang, J.; Grimsdale, A. C.; Müllen, K.; MacKenzie, J. D.; Silva, C.; Friend, R. H. *J. Am. Chem. Soc.* **2003**, *125*, 437.

(2) Briseno, A. L.; Mannsfeld, S. C. B.; Reese, C.; Hancock, J. M.; Xiong, Y.; Jenekhe, S. A.; Bao, Z.; Xia, Y. *Nano Lett.* **2007**, *7*, 2847.

(3) Wang, S.; Pisula, W.; Müllen, K. *J. Mater. Chem.* **2012**, *22*, 24827.

(4) Rozanski, L. J.; Castaldelli, E.; Sam, F. L. M.; Mills, C. A.; Demets, G. J.; Silva, S. R. P. *J. Mater. Chem. C* **2013**, *1*, 3347.

(5) Earmme, T.; Hwang, Y.; Murari, N. M.; Subramaniyan, S.; Jenekhe, S. A. *J. Am. Chem. Soc.* **2013**, *135*, 14960.

(6) Lin, Y.; Wang, Y.; Wang, J.; Hou, J.; Li, Y.; Zhu, D.; Zhan, X. *Adv. Mater.* **2014**, *26*, 5137.

(7) Kozycz, L. M.; Gao, D.; Tilley, A. J.; Seferos, D. S. *J. Polym. Sci., Part A: Polym. Chem.* **2014**, *52*, 3337.

(8) Hwang, Y.; Earmme, T.; Courtright, B. A. E.; Eberle, F. N.; Jenekhe, S. A. *J. Am. Chem. Soc.* **2015**, *137*, 4424.

(9) Marcon, R. O.; Brochsztain, S. *J. Phys. Chem. A* **2009**, *113*, 1747.

(10) Debreczeny, M. P.; Svec, W. A.; Marsh, E. M.; Wasielewski, M. R. *J. Am. Chem. Soc.* **1996**, *118*, 8174.

(11) Gosztola, D.; Niemczyk, M. P.; Svec, W.; Lukas, A. S.; Wasielewski, M. R. *J. Phys. Chem. A* **2000**, *104*, 6545.

(12) Lukas, A. S.; Miller, S. E.; Wasielewski, M. R. *J. Phys. Chem. B* **2000**, *104*, 931.

(13) Lukas, A. S.; Bushard, P. J.; Wasielewski, M. R. *J. Am. Chem. Soc.* **2001**, *123*, 2440.

(14) Ghosh, I.; Ghosh, T.; Bardagi, J. I.; König, B. *Science* **2014**, *346*, 725.

(15) Fujitsuka, M.; Kim, S. S.; Lu, C.; Tojo, S.; Majima, T. *J. Phys. Chem. B* **2015**, *119*, 7275.

(16) Fujitsuka, M.; Ohsaka, T.; Majima, T. *Phys. Chem. Chem. Phys.* **2015**, *17*, 31030.

(17) Lu, C.; Fujitsuka, M.; Sugimoto, A.; Majima, T. *J. Phys. Chem. C* **2016**, *120*, 12734.

(18) Zeng, L.; Liu, T.; He, C.; Shi, D.; Zhang, F.; Duan, C. *J. Am. Chem. Soc.* **2016**, *138*, 3958.

(19) Fujitsuka, M.; Cho, D. W.; Tojo, S.; Inoue, A.; Shiragami, T.; Yasuda, M.; Majima, T. *J. Phys. Chem. A* **2007**, *111*, 10574.

(20) Fujitsuka, M.; Luo, C.; Ito, O. *J. Phys. Chem. B* **1999**, *103*, 445.

(21) Marcus, R. A. *Annu. Rev. Phys. Chem.* **1964**, *15*, 144.

(22) Marcus, R. A.; Sutin, N. *Biochim. Biophys. Acta* **1985**, *811*, 265.

(23) Marcus, R. A. *Angew. Chem. Int. Ed. Eng.* **1993**, *32*, 1111.

(24) van Haare, J. A.; Havinga, E. E.; van Dongen, J. L.; Janssen, R. A.; Cornil, J.; Brédas, J. L. *Chem. Eur. J.* **1998**, *4*, 1509.

(25) Heeger, A. J. *J. Phys. Chem. B* **2001**, *105*, 8475.

(26) Park, B.; Yang, L.; Johansson, E. M. J.; Vlachopoulos, N.; Chams, A.; Perruchot, C.; Jouini, M.; Boschloo, G.; Hagfeldt, A. *J. Phys. Chem. C* **2013**, *117*, 22484.

(27) Kuang, L.; Olson, T. L.; Lin, S.; Flores, M.; Jiang, Y.; Zheng, W.; Williams, J. C.; Allen, J. P.; Liang, H. *J. Phys. Chem. Lett.* **2014**, *5*, 787.

(28) Gao, W.; Liu, T.; Hao, M.; Wu, K.; Zhang, C.; Sun, Y.; Yang, C. *Chem. Sci.* **2016**, *7*, 6167.

Chapter 3. Photo-Accelerated Hole Transfer in Oligothiophene Assemblies

Abstract

A new series of mesitylene-linked oligothiophenes (*n*T, *n* is the number of thiophene units), including 2T-M, 3T-M, 4T-M, 4T-M-2T, and 4T-M-3T, was prepared to investigate the intramolecular hole transfer (HT) from excited radical cation for the first time. The results of spectroscopic and theoretical studies indicated that mesitylene acts as a spacer minimizing the perturbation to the thiophene π-conjugation and increasing the stability of *n*T radical cations ($n\mathrm{T}^{\bullet+}$). Femtosecond laser flash photolysis was applied to $4\mathrm{T}^{\bullet+}$-M, $4\mathrm{T}^{\bullet+}$-M-2T, and $4\mathrm{T}^{\bullet+}$-M-3T. Upon 670 nm laser excitation, the transient absorption spectra of $4\mathrm{T}^{\bullet+}$-M showed the existence of two species as the D_1 and D_0^{hot} states. The intramolecular HT processes from excited $4\mathrm{T}^{\bullet+}$ ($4\mathrm{T}^{\bullet+}$*) with the time constants of 1.6 and 0.8 ps were observed upon excitation of $4\mathrm{T}^{\bullet+}$-M-2T and $4\mathrm{T}^{\bullet+}$-M-3T, respectively. This was the first capture of such ultrafast processes with the subsequent back HT from the ground-state $2\mathrm{T}^{\bullet+}$ or $3\mathrm{T}^{\bullet+}$ in *n*T assemblies. The current findings indicated an accelerated migration of photocarriers (polarons) in thiophene-based p-type semiconductor materials upon irradiation and provided a fresh viewpoint to understand the successive HT in polythiophenes for various organic molecular devices.

Introduction

Oligothiophenes (*n*T, *n* is the number of thiophene units) and polythiophenes, which are among the most well-known p-type π-conjugated materials, have been used as the core components in various photoelectric devices such as organic photovoltaics (OPVs), organic light emitting diodes (OLEDs), and organic field effect transistors (OFETs).[1-6] This is mainly due to two of their extraordinary characteristics: ease of oxidation and excellent charge mobility. Consequently, the generation of oxidized *n*T ($n\mathrm{T}^{\bullet+}$) as the photocarriers (polarons) is essential for their electronic and optical performances.[7,8] With the progress of modern science and technology, nowadays the properties of *n*T and polythiophenes can be studied by molecular-level approaches like single-molecule electroluminescence or photoluminescence spectroscopy, which provides the detailed behaviors of photocarriers.[9-12] It should be pointed out that in the case of polythiophenes, the positive charge is localized on the *n*T moieties instead of being delocalized on the entire polymer chains.[13,14] Recently, theoretical simulations showed that the localized charge in a thiophene-containing molecular wire can be transported by stepwise hopping or tunneling along the π-conjugation backbone.[15] However, the actual structures of polythiophenes (e.g., poly(3-alkylthiophene)) appear to have a large extent of bending and folding in their chains, thus making it difficult to provide a clear description of the molecular structures and direct observation of the charge transport.[16,17] Therefore, the hole transfer (HT) in polythiophenes should have various possible pathways, and their mechanisms and kinetics should be elucidated.

On the other hand, there is a growing interest in the studies of excited radical ions, which can be treated as stronger redox agents than those in the ground states.[18-22] Previously, the properties of excited radical cations have been discussed on the basis of their fluorescence behaviors and relaxation dynamics.[23-31] In particular, our group investigated the lifetimes of excited $n\mathrm{T}^{\bullet+}$ ($n\mathrm{T}^{\bullet+}$*) obtained from the bleaching of $n\mathrm{T}^{\bullet+}$ absorption upon laser excitation.[32] Furthermore, in the presence of a hole acceptor (A), e.g., 1-methoxynaphthalene, the intermolecular HT from $n\mathrm{T}^{\bullet+}$* was confirmed by the observation of $\mathrm{A}^{\bullet+}$.[32] It is worth noting that the excited-state properties of $n\mathrm{T}^{\bullet+}$ are very important when considering the charge carrier in photoconduction for various thiophene-based organic molecular devices. Here, $n\mathrm{T}^{\bullet+}$* should be regarded as the precursors, not only leading to oxidative reactions, but also generating photocarriers (polarons).

Nevertheless, the direct information about $n\mathrm{T}^{\bullet+}$* and the intramolecular HT processes from them have not yet been reported due to the lack of proper molecular systems and analytical methods.

Thus, in this study, 3,3'-dihexyl-2,2'-bithiophene (2T), 3,3''-dihexyl-2,2':5',2''-terthiophene (3T), and 3,3'''-dihexyl-2,2':5',2'':5'',2'''-quaterthiophene (4T) with a new series of their mesitylene-linked derivatives including 2T-M, 3T-M, 4T-M, 4T-M-2T, and 4T-M-3T were prepared as the target molecules (Scheme 3-1). Hexyl groups were introduced to these molecules to achieve a substantial solubility in organic solvents. The ground- and excited-state properties of mesitylene-linked $n\mathrm{T}^{\bullet+}$ were investigated in detail, and for the first time, ultrafast intramolecular HT processes from excited radical cation ($4\mathrm{T}^{\bullet+}$*) were observed. This was also the first capture of such photo-accelerated processes in *n*T assemblies.

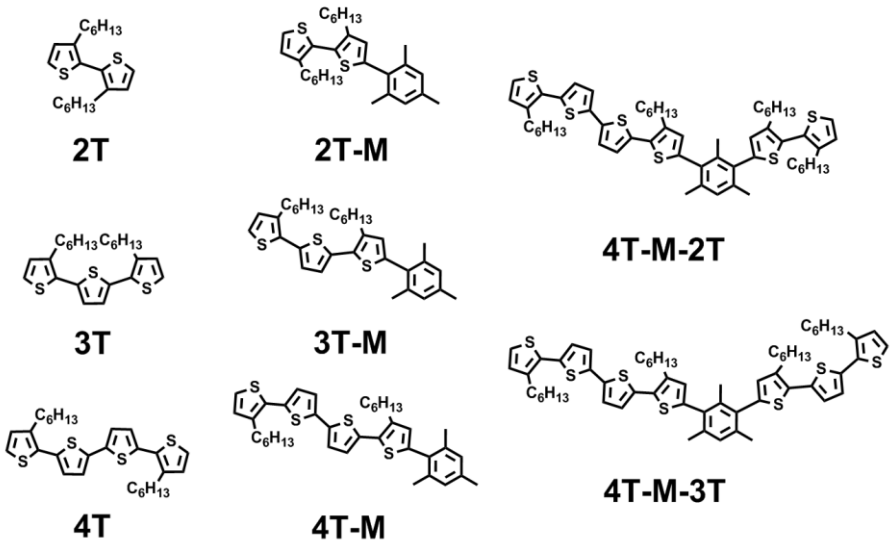

Scheme 3-1. Chemical structures of 2T, 3T, 4T, 2T-M, 3T-M, 4T-M, 4T-M-2T, and 4T-M-3T.

Experimental Section

Synthesis.

3,3'-Dihexyl-5-mesityl-2,2'-bithiophene (2T-M)

To a solution of 3,3'-dihexyl-2,2'-bithiophene (0.45 g, 1.34 mmol) in 10 mL of THF, a 1.6 M solution of *n*-BuLi in hexane (0.88 mL, 1.41 mmol) was added dropwise at -78 ℃. The solution was stirred for 1 h at room temperature. Afterwards the solution was cooled to -78 ℃ and tri(*n*-

butyl)stannyl chloride (0.48 g, 1.47 mmol) was added. The solution was stirred for 1 h at room temperature. Afterwards the reaction solution was extracted by dichloromethane, dried over Na_2SO_4 and evaporated in vacuo to give a crude product. This crude product was then dissolved in 10 mL toluene and added dropwise to a solution of 2-bromo-1,3,5-trimethylbenzene (0.27 g, 1.36 mmol), $Pd(PPh_3)_4$ (0.077 g, 0.07 mmol) and 10 mL toluene under argon. Finally the reaction solution was refluxed overnight. Afterwards the reaction solution was extracted by dichloromethane, dried over Na_2SO_4 and evaporated in vacuo to give a crude product. Further purification was carried by column chromatography (silica gel; hexane) to obtain the transparent oily **2T-M** (0.30 g, 0.66 mmol, 49%).

^{1}H NMR ($CDCl_3$, 400 MHz): δ 7.29 (d, *J* = 5.5 Hz, 1H), 6.97 (d, *J* = 5.5 Hz, 1H), 6.94 (s, 2H), 6.64 (s, 1H), 2.58 (m, 4H), 2.32 (s, 3H), 2.19 (s, 6H), 1.68 (m, 4H), 1.32 (m, 12H), 0.90 (m, 6H).

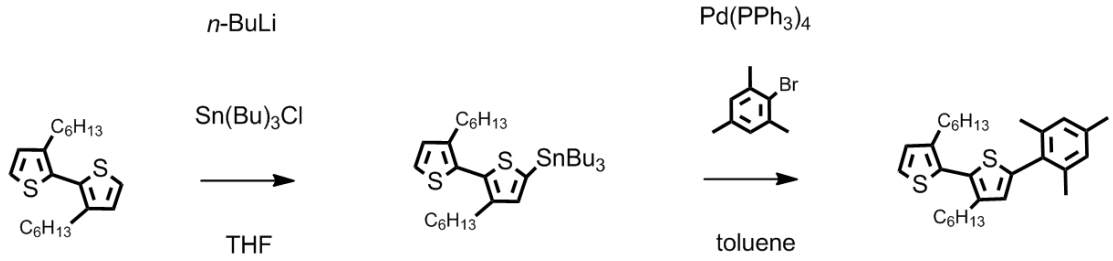

Scheme 3-2. Synthesis of **2T-M**.

3,3''-Dihexyl-5-mesityl-2,2':5',2''-terthiophene (3T-M)

To a solution of 3,3"-dihexyl-2,2':5',2"-terthiophene (0.57 g, 1.37 mmol) in 10 mL of THF, a 1.6 M solution of *n*-BuLi in hexane (0.91 mL, 1.44 mmol) was added dropwise at -78 ℃. The solution was stirred for 1 h at room temperature. Afterwards the solution was cooled to -78 ℃ and tri(*n*-butyl)stannyl chloride (0.49 g, 1.51 mmol) was added. The solution was stirred for 1 h at room temperature. Afterwards the reaction solution was extracted by dichloromethane, dried over Na_2SO_4 and evaporated in vacuo to give a crude product. This crude product was then dissolved in 10 mL toluene and added dropwise to a solution of 2-bromo-1,3,5-trimethylbenzene (0.27 g, 1.36 mmol), $Pd(PPh_3)_4$ (0.080 g, 0.07 mmol) and 10 mL toluene under argon. Finally the reaction solution was refluxed overnight. Afterwards the reaction solution was extracted by dichloromethane, dried over Na_2SO_4 and evaporated in vacuo to give a crude product. Further

purification was carried by column chromatography (silica gel; hexane) to obtain the yellow oily **3T-M** (0.35 g, 0.65 mmol, 48%).

^{1}H NMR ($CDCl_3$, 400 MHz): δ 7.18 (d, *J* = 5.5 Hz, 1H), 7.08 (m, 2H), 6.95 (m, 3H), 6.62 (s, 1H), 2.83 (m, 4H), 2.32 (s, 3H), 2.20 (s, 6H), 1.71 (m, 4H), 1.39 (m, 12H), 0.90 (m, 6H).

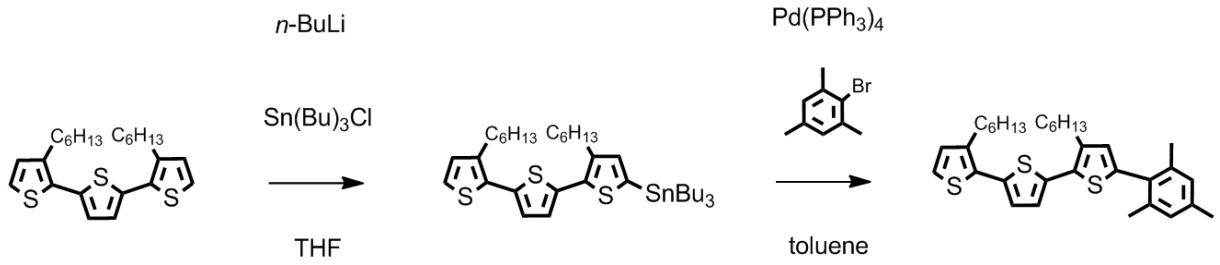

Scheme 3-3. Synthesis of **3T-M**.

3,3'''-Dihexyl-5-mesityl-2,2':5',2'':5'',2'''-quaterthiophene (4T-M)

To a solution of 3,3'''-dihexyl-2,2':5',2'':5'',2'''-quaterthiophene (0.46 g, 0.92 mmol) in 10 mL of THF, a 1.6 M solution of *n*-BuLi in hexane (0.60 mL, 0.97 mmol) was added dropwise at -78 ℃. The solution was stirred for 1 h at room temperature. Afterwards the solution was cooled to -78 ℃ and tri(*n*-butyl)stannyl chloride (0.33 g, 1.01 mmol) was added. The solution was stirred for 1 h at room temperature. Afterwards the reaction solution was extracted by dichloromethane, dried over Na_2SO_4 and evaporated in vacuo to give a crude product. This crude product was then dissolved in 10 mL toluene and added dropwise to a solution of 2-bromo-1,3,5-trimethylbenzene (0.20 g, 1.00 mmol), $Pd(PPh_3)_4$ (0.053 g, 0.05 mmol) and 10 mL toluene under argon. Finally the reaction solution was refluxed overnight. Afterwards the reaction solution was extracted by dichloromethane, dried over Na_2SO_4 and evaporated in vacuo to give a crude product. Further purification was carried by column chromatography (silica gel; hexane) to obtain the yellow oily **4T-M** (0.25 g, 0.41 mmol, 45%).

^{1}H NMR ($CDCl_3$, 400 MHz): δ 7.19 (d, *J* = 5.3 Hz, 1H), 7.13 (d, *J* = 3.9 Hz, 2H), 7.04 (m, 2H), 6.95 (m, 3H), 6.62 (s, 1H), 2.83 (m, 4H), 2.32 (s, 3H), 2.20 (s, 6H), 1.70 (m, 4H), 1.39 (m, 12H), 0.91 (m, 6H).

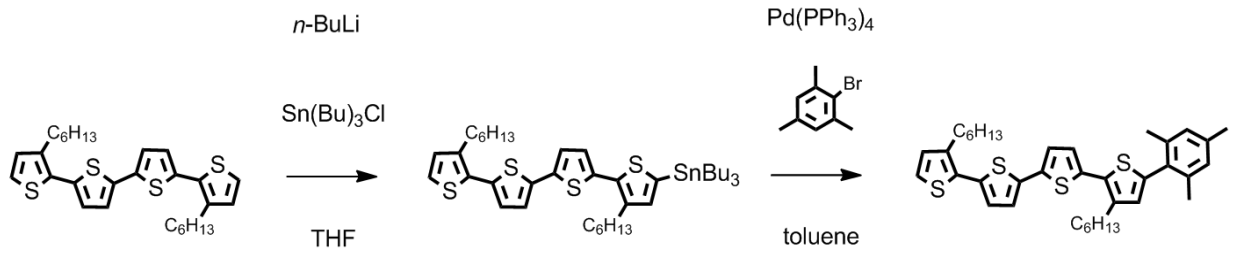

Scheme 3-4. Synthesis of **4T-M**.

5-(3-Bromo-2,4,6-trimethylphenyl)-3,3'-dihexyl-2,2'-bithiophene (Br-M-2T)

To a solution of 3,3'-dihexyl-2,2'-bithiophene (0.50 g, 1.49 mmol) in 10 mL of THF, a 1.6 M solution of *n*-BuLi in hexane (0.98 mL, 1.56 mmol) was added dropwise at -78 ℃. The solution was stirred for 1 h at room temperature. Afterwards the solution was cooled to -78 ℃ and tri(*n*-butyl)stannyl chloride (0.53 g, 1.63 mmol) was added. The solution was stirred for 1 h at room temperature. Afterwards the reaction solution was extracted by dichloromethane, dried over Na_2SO_4 and evaporated in vacuo to give a crude product. This crude product was then dissolved in 10 mL toluene and added dropwise to a solution of 2,4-dibromo-1,3,5- trimethylbenzene (0.41 g, 1.49 mmol), $Pd(PPh_3)_4$ (0.086 g, 0.07 mmol) and 10 mL toluene under argon. Finally the reaction solution was refluxed overnight. Afterwards the reaction solution was extracted by dichloromethane, dried over Na_2SO_4 and evaporated in vacuo to give a crude product. Further purification was carried by column chromatography (silica gel; hexane) to obtain the transparent oily **Br-M-2T** (0.40 g, 0.75 mmol, 50%).

^{1}H NMR ($CDCl_3$, 400 MHz): δ 7.29 (m, 1H), 7.02 (s, 1H), 6.97 (m, 1H), 6.63 (s, 1H), 2.58 (m, 4H), 2.42 (s, 3H), 2.32 (s, 3H), 2.13 (s, 3H), 1.65 (m, 4H), 1.34 (m, 12H), 0.90 (m, 6H).

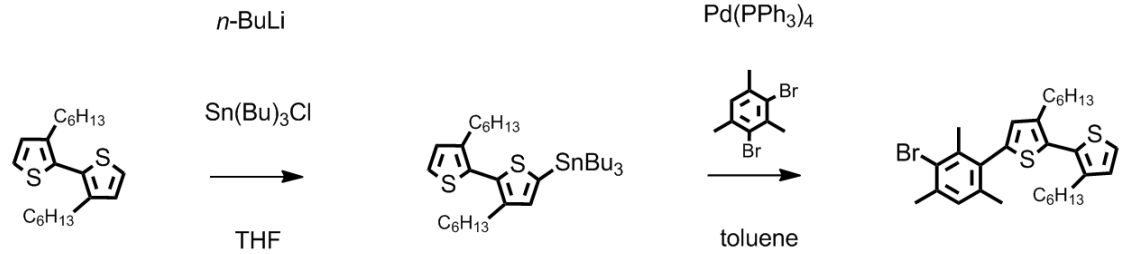

Scheme 3-5. Synthesis of **Br-M-2T**.

5-(3-(3,3'-Dihexyl-[2,2'-bithiophen]-5-yl)-2,4,6-trimethylphenyl)-3,3'''-dihexyl-2,2':5', 2'':5'',2'''-quaterthiophene (4T-M-2T)

To a solution of 3,3'''-dihexyl-2,2':5',2'':5'',2'''-quaterthiophene (0.37 g, 0.75 mmol) in 10 mL of THF, a 1.6 M solution of *n*-BuLi in hexane (0.49 mL, 0.79 mmol) was added dropwise at -78 ℃. The solution was stirred for 1 h at room temperature. Afterwards the solution was cooled to -78 ℃ and tri(*n*-butyl)stannyl chloride (0.27 g, 0.83 mmol) was added. The solution was stirred for 1 h at room temperature. Afterwards the reaction solution was extracted by dichloromethane, dried over Na_2SO_4 and evaporated in vacuo to give a crude product. This crude product was then dissolved in 10 mL toluene and added dropwise to a solution of **Br-M-2T** (0.40 g, 0.75 mmol), $Pd(PPh_3)_4$ (0.043 g, 0.04 mmol) and 10 mL toluene under argon. Finally the reaction solution was refluxed overnight. Afterwards the reaction solution was extracted by dichloromethane, dried over Na_2SO_4 and evaporated in vacuo to give a crude product. Further purification was carried by column chromatography (silica gel; hexane) to obtain the yellow oily **4T-M-2T** (0.30 g, 0.32 mmol, 43%).

^{1}H NMR ($CDCl_3$, 400 MHz): δ 7.29 (d, *J* = 5.0 Hz, 1H), 7.19 (d, *J* = 5.0 Hz, 1H), 7.14 (d, *J* = 3.7 Hz, 2H), 7.06 (m, 3H), 6.97 (m, 2H), 6.67 (m, 2H), 2.84 (m, 6H), 2.58 (m, 4H), 2.23 (s, 6H), 2.09 (s, 3H), 1.72 (m, 6H), 1.39 (m, 24H), 0.90 (m, 12H). FAB MS: calcd. 948.40, found 949 (M+1).

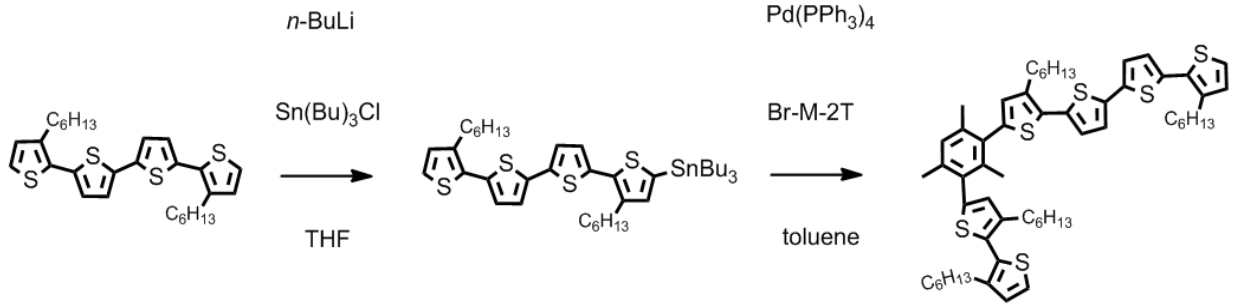

Scheme 3-6. Synthesis of **4T-M-2T**.

5-(3-Bromo-2,4,6-trimethylphenyl)-3,3''-dihexyl-2,2':5',2''-terthiophene (Br-M-3T)

To a solution of 3,3"-dihexyl-2,2':5',2"-terthiophene (0.42 g, 1.01 mmol) in 10 mL of THF, a 1.6 M solution of *n*-BuLi in hexane (0.66 mL, 1.06 mmol) was added dropwise at -78 ℃. The solution was stirred for 1 h at room temperature. Afterwards the solution was cooled to -78 ℃

and tri(*n*-butyl)stannyl chloride (0.36 g, 1.11 mmol) was added. The solution was stirred for 1 h at room temperature. Afterwards the reaction solution was extracted by dichloromethane, dried over Na_2SO_4 and evaporated in vacuo to give a crude product. This crude product was then dissolved in 10 mL toluene and added dropwise to a solution of 2,4-dibromo-1,3,5-trimethylbenzene (0.28 g, 1.01 mmol), $Pd(PPh_3)_4$ (0.058 g, 0.05 mmol) and 10 mL toluene under argon. Finally the reaction solution was refluxed overnight. Afterwards the reaction solution was extracted by dichloromethane, dried over Na_2SO_4 and evaporated in vacuo to give a crude product. Further purification was carried by column chromatography (silica gel; hexane) to obtain the yellow oily **Br-M-3T** (0.40 g, 0.65 mmol, 64%).

^{1}H NMR ($CDCl_3$, 400 MHz): δ 7.19 (d, *J* = 5.3 Hz, 1H), 7.08 (m, 2H), 7.02 (s, 1H), 6.95 (d, *J* = 5.3 Hz, 1H), 6.61 (s, 1H), 2.83 (m, 4H), 2.42 (s, 3H), 2.32 (s, 3H), 2.14 (s, 3H), 1.71 (m, 4H), 1.38 (m, 12H), 0.90 (m, 6H).

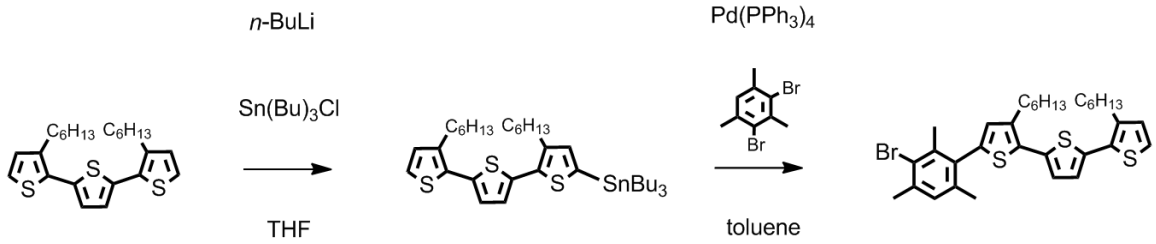

Scheme 3-7. Synthesis of **Br-M-3T**.

4-(3-(3,3''-Dihexyl-[2,2':5',2''-terthiophen]-5-yl)-2,4,6-trimethylphenyl)-3,3'''-dihexyl-2,2':5',2'':5'',2'''-quaterthiophene (4T-M-3T)

To a solution of 3,3'''-dihexyl-2,2':5',2'':5'',2'''-quaterthiophene (0.32 g, 0.64 mmol) in 10 mL of THF, a 1.6 M solution of *n*-BuLi in hexane (0.38 mL, 0.65 mmol) was added dropwise at -78 ℃. The solution was stirred for 1 h at room temperature. Afterwards the solution was cooled to -78 ℃ and tri(*n*-butyl)stannyl chloride (0.23 g, 0.71 mmol) was added. The solution was stirred for 1 h at room temperature. Afterwards the reaction solution was extracted by dichloromethane, dried over Na_2SO_4 and evaporated in vacuo to give a crude product. This crude product was then dissolved in 10 mL toluene and added dropwise to a solution of **Br-M-3T** (0.40 g, 0.65 mmol), $Pd(PPh_3)_4$ (0.035 g, 0.03 mmol) and 10 mL toluene under argon. Finally the reaction solution was refluxed overnight. Afterwards the reaction solution was extracted by dichloromethane,

dried over Na_2SO_4 and evaporated in vacuo to give a crude product. Further purification was carried by column chromatography (silica gel; hexane/dichloromethane (10:1, v/v)) to obtain the yellow oily **4T-M-3T** (0.30 g, 0.29 mmol, 45%).

^{1}H NMR ($CDCl_3$, 400 MHz): δ 7.19 (m, 2H), 7.14 (d, J = 3.9 Hz, 2H), 7.08 (m, 5H), 6.95 (d, J = 5.3 Hz, 2H), 6.66 (s, 2H), 2.84 (m, 8H), 2.23 (s, 6H), 2.10 (s, 3H), 1.72 (m, 8H), 1.39 (m, 24H), 0.90 (m, 12H). FAB MS: calcd. 1030.38, found 1031 (M+1).

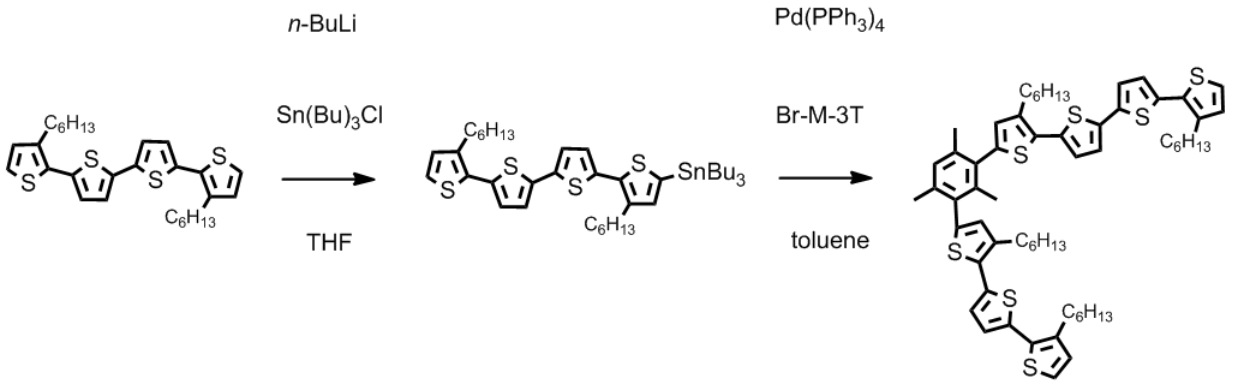

Scheme 3-8. Synthesis of **4T-M-3T**.

Materials. 2T, 3T, and 4T were synthesized according to the reported procedures.[33] 2T-M, 3T-M, 4T-M, 4T-M-2T, and 4T-M-3T were synthesized as described above. 1,2-Dichloroethane (DCE) was used as the solvent for spectroscopic measurements. Anhydrous powder of iron (III) chloride ($FeCl_3$) was purchased from Sigma-Aldrich.

Apparatus. Steady-state absorption spectra were measured using a Shimadzu UV-3600 UV-vis-NIR spectrometer. Transient absorption spectra during the femtosecond laser flash photolysis were measured as described previously.[34] In this study, the samples were excited by a 670 or 1120 nm femtosecond laser pulse (~130 fs fwhm, ~5 μJ per pulse).

Theoretical Calculations. The optimized structures of the molecules in this study were estimated using density functional theory (DFT) at the B3LYP/6-31G(d) level. The excitation energies for $n\mathrm{T}^{\bullet+}$* were calculated using the time-dependent DFT (TD-DFT) at the (U)B3LYP/6-31G(d) level, including the solvent effect using the SCRF(CPCM) method. All the

theoretical calculations were carried out using the Gaussian 09 package.[35] It was confirmed that the estimated structures did not exhibit imaginary frequencies.

Results and Discussion

Figure 3-1 shows the absorption spectra of 2T, 3T, 4T, 2T-M, 3T-M, 4T-M, 4T-M-2T, and 4T-M-3T in DCE. The dashed lines show the superpositions, i.e., 4T + 2T and 4T + 3T. It is notable that the absorption maxima ($\lambda^{Abs.}{}_{max}$) of *n*T-M shifted to the slightly longer wavelength than those of *n*T with almost the same molar absorption coefficient maxima (ε_{max}) (Figure 3-1a). Similarly, the absorption spectrum of 4T-M-2T showed a slightly red-shifted peak with almost the same ε_{max} when compared to the superposition of 2T and 4T (Figure 3-1b). This trend was also confirmed in 4T-M-3T. Previously, it was reported that a dyad system consisted of two 2Ts linked by a phenyl ring showed a significant red-shift in $\lambda^{Abs.}{}_{max}$ and increase in ε_{max}, suggesting a strongly conjugated network between two 2Ts through the phenyl ring.[36] However, in the cases of 4T-M-2T and 4T-M-3T, the conjugation of 4T and 2T (or 3T) through the mesitylene group is highly suppressed because of the perpendicular conformation between *n*T and mesitylene caused by the steric effect of the methyl groups. To obtain further insight on this point, DFT calculations were carried out to estimate the structure of 4T-M-3T as well as its highest occupied molecular orbital (HOMO) and lowest unoccupied molecular orbital (LUMO) surfaces. The calculation results are shown in Figure 3-2, in which the hexyl substituents were simplified to the methyl substituents. It was found that the dihedral angles between mesitylene and linked *n*T are in the range of 84.3°−84.9°, i.e., almost perpendicular. Moreover, the HOMO and LUMO of 4T-M-3T are mainly localized on the 4T moiety. The theoretical results are consistent with the above-mentioned absorption spectra, indicating that the mesitylene group can connect different *n*T moieties without a strong perturbation to their π-conjugation systems.

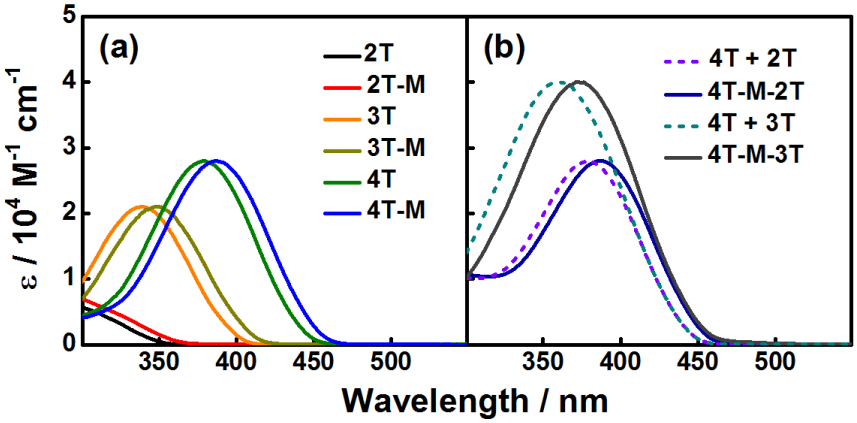

Figure 3-1. Absorption spectra of 2T, 3T, 4T, 2T-M, 3T-M, 4T-M, 4T-M-2T, and 4T-M-3T in DCE. Dashed lines indicate the added absorptions of 4T + 2T and 4T + 3T.

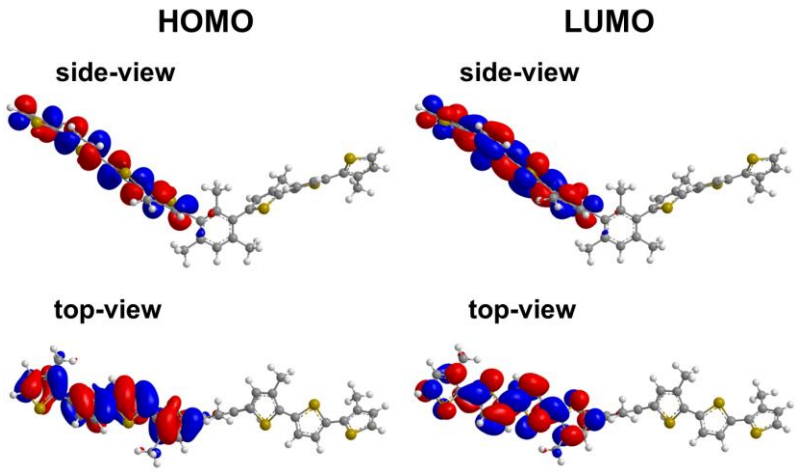

Figure 3-2. HOMO (left) and LUMO (right) surfaces for 4T-M-3T. (Hexyl groups were replaced by methyl groups for simplifying the calculations.)

Figure 3-3 shows the absorption spectra of 4T, 4T-M, 4T-M-2T, and 4T-M-3T with varied concentrations of $FeCl_3$ in DCE. In the case of 4T (Figure 3-3a), with the addition of $FeCl_3$ as an oxidizing reagent,[37,38] the absorbance of 4T showed a decrease, and two absorption peaks attributable to $4T^{\bullet+}$ were detected in the visible (660 nm) and near-infrared (1080 nm) regions. However, by further increasing the concentration of $FeCl_3$, extra signals located at the longer wavelength sides of $4T^{\bullet+}$ peaks were observed in the spectra. These signals can be assigned to $4T^{2+}$, resulting from the non-stepwisely oxidized $4T^{\bullet+}$ (e.g., disproportionation of $4T^{\bullet+}$).[37] On the other hand, in the case of 4T-M (Figure 3-3b), with the addition of $FeCl_3$, the absorbance of 4T-

M decreased, and new absorption peaks at 670 and 1120 nm appeared, indicating the production of $4T^{\bullet+}$-M. By increasing the $FeCl_3$ concentration, the absorbance of $4T^{\bullet+}$-M showed a further increase and no signals from the dication species were detected in the spectra. Similar phenomena were also confirmed in the cases of 4T-M-2T and 4T-M-3T, indicating that the 4T moiety in these dyads was selectively oxidized by $FeCl_3$ (Figures 3-3c, d). Thus, it was found that the linkage by the mesitylene group significantly improved the stability of $4T^{\bullet+}$, which is essential for the subsequent laser flash photolysis. This finding can be attributed to the electron-donating nature of the mesitylene group that reduces the positive charge density on the thiophene units, thus lowering the reactivity of $4T^{\bullet+}$.[39]

Moreover, during the oxidation of 2T/3T, only the signals of disproportionately produced dication species were detected (Figures 3-4a, c); whereas in the case of 2T-M/3T-M, first the absorption of $2T^{\bullet+}$-M/$3T^{\bullet+}$-M and then the additional signals of $2T^{2+}$-M/$3T^{2+}$-M were observed in the spectra with an increase in the $FeCl_3$ concentration (Figures 3-4b, d). Here, the stabilizing effect of mesitylene was proved again. The information of $2T^{\bullet+}$-M and $3T^{\bullet+}$-M (Table 3-1) is necessary for analyzing the transient absorption spectra of $4T^{\bullet+}$-M-2T and $4T^{\bullet+}$-M-3T.

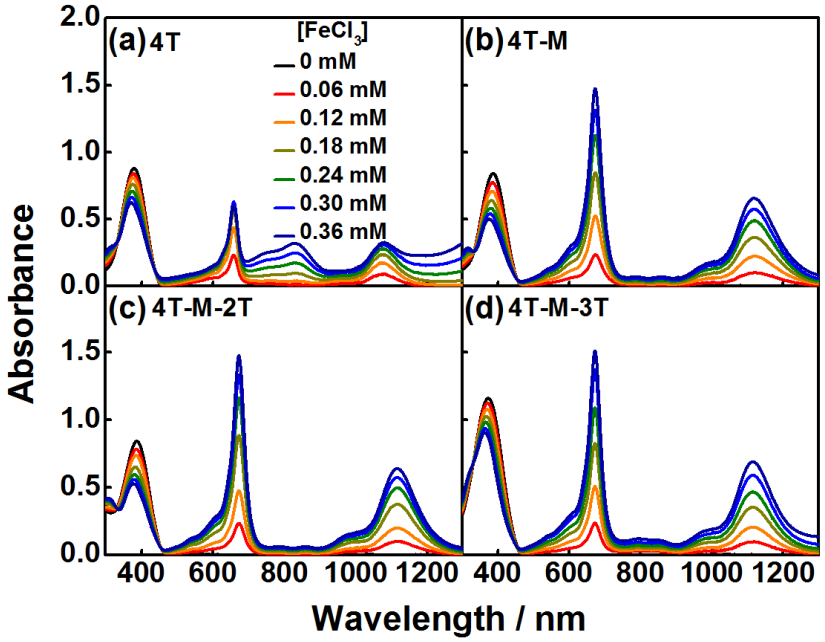

Figure 3-3. Absorption spectra of 4T (0.15 mM), 4T-M (0.15 mM), 4T-M-2T (0.15 mM), and 4T-M-3T (0.15 mM) with varied concentration of $FeCl_3$ (0-0.36 mM) in DCE.

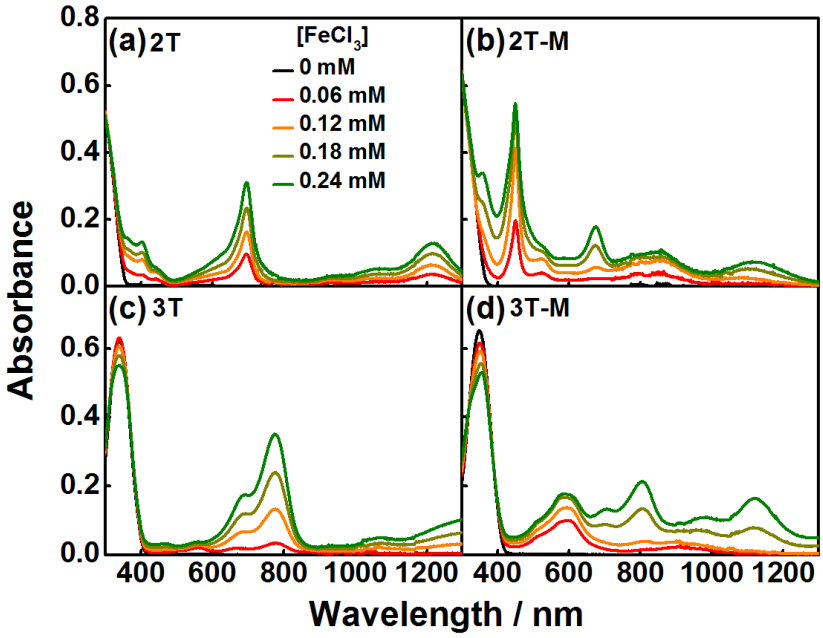

Figure 3-4. Absorption spectra of 2T (0.45 mM), 2T-M (0.45 mM), 3T (0.15 mM), and 3T-M (0.15 mM) with varied concentration of $FeCl_3$ (0−0.24 mM) in DCE.

Table 3-1. Absorption Peak Positions of *n*T in Neutral and Oxidized States Observed by $FeCl_3$ Oxidation.

	$\lambda^{Abs.}_{max}$ (*n*T) (nm)	$\lambda^{Abs.}_{max}$ ($nT^{\bullet+}$) (nm)	$\lambda^{Abs.}_{max}$ (nT^{2+}) (nm)
2T	< 300	-[a]	695, ~1215
2T-M	< 300	450, ~860	675, ~1118
3T	340	-[a]	777
3T-M	350	590, ~908	806, ~1123
4T	380	658, 1075	832
4T-M	388	673, 1118	-[a]
4T-M-2T	388	673, 1118	-[a]
4T-M-3T	374	673, 1118	-[a]

[a]Not observed.

Figure 3-5a shows the transient absorption spectra of $4T^{\bullet+}$-M during the laser flash photolysis using a 670 nm femtosecond laser excitation. The spectrum recorded at 0.6 ps after the laser excitation showed a 430 nm-peaked positive band with a shoulder at 510 nm and a negative band at >565 nm, corresponding to the generation of $4T^{\bullet+}$*-M and bleaching of $4T^{\bullet+}$-M, respectively. By increasing the delay time, the positive band decreased and the negative band showed a recovery, suggesting the deactivation process from $4T^{\bullet+}$*-M to $4T^{\bullet+}$-M. As indicated in Figure 3-5b, the dynamics of $4T^{\bullet+}$*-M were analyzed by global fitting assuming a double exponential function to the positive band. This resulted in a 430 nm-maximized major species with a decay constant of 4.8×10^{11} s^{-1} (2.1 ps) and a 510 nm-maximized minor species with a decay constant of 5.9×10^{10} s^{-1} (17 ps). To assign these two species, the transient absorption spectra of $4T^{\bullet+}$-M were also taken using an 1120 nm excitation, and only the 430 nm-peaked positive band without a shoulder was observed (Figure 3-6). It should be mentioned that according to the excitation energies obtained by the TD-DFT calculations (Table 3-2), the 670 and 1120 nm laser pulses initially excited $4T^{\bullet+}$-M to the D_2 and D_1 states, respectively. Therefore, the decay of the 430 nm-peaked band with a lifetime of 2.1 ps can be attributed to the D_1–D_0 internal conversion, whereas the decay of the 510 nm-peaked band with a lifetime of 17 ps is attributable to the relaxation of $4T^{\bullet+}$-M in the vibrationally hot ground state (D_0^{hot}), which was probably originated from the excess energy deposited on a small portion of the sample solution. In addition, the internal conversion from the D_2 state was too rapid to be detected.

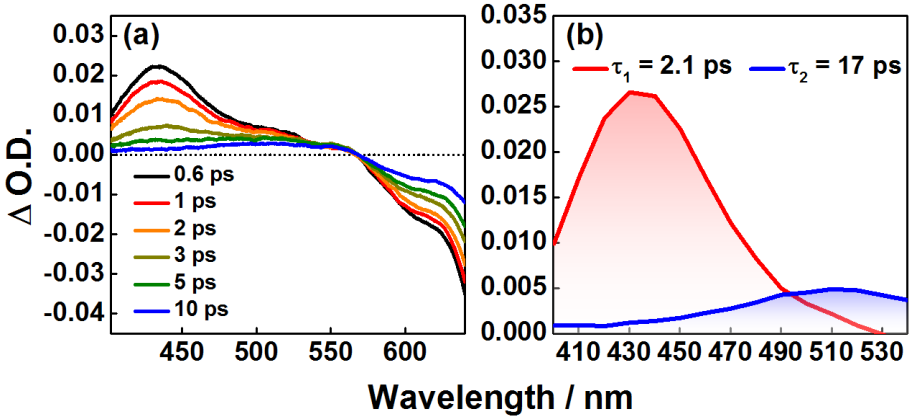

Figure 3-5. (a) Transient absorption spectra of 4T-M (0.15 mM) in DCE with the presence of $FeCl_3$ (0.30 mM) during a 670 nm femtosecond laser excitation. (b) Decay-associated spectra obtained by global fitting assuming a double exponential function to the positive band in Figure 3-5a.

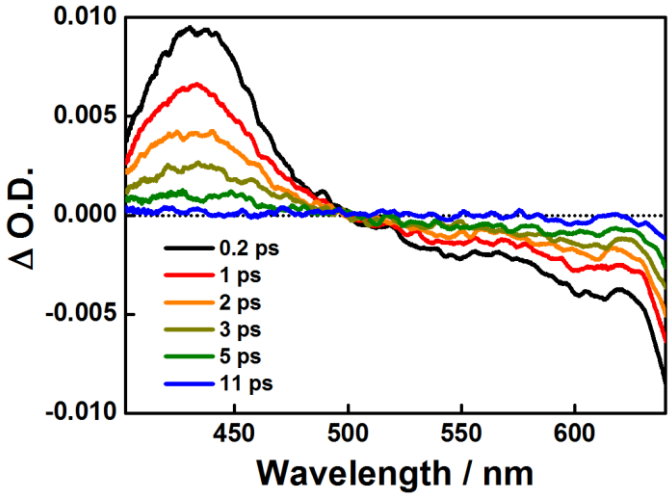

Figure 3-6. Transient absorption spectra of 4T-M (0.15 mM) in DCE with the presence of $FeCl_3$ (0.30 mM) during an 1120 nm femtosecond laser excitation.

Table 3-2. Calculated Transition Energies (*E*), Oscillator Strength (*f*), and Relative Contribution of Excited State Configuration of 4T Radical Cation (C_{2h} Symmetry).

	Calcd. *E* (eV)	*f*	Relative contribution of excited state configuration[a]
Excited state 1	1.323	0.281	0.91(H-1(β) → H(β)) − 0.41(H(α) → L(α))
Excited state 2	2.060	1.352	0.86(H(α) → L(α))
Excited state 3	2.160	0.000	0.92(H-2(β) → H(β))
Excited state 4	2.202	0.009	0.97(H-3(β) → H(β))

[a]Relative contribution larger than 0.3 is indicated. H and L indicate HOMO and LUMO, respectively.

Figure 3-7a shows the transient absorption spectra of $4T^{\bullet+}$-M-2T during the laser flash photolysis using a 670 nm femtosecond laser excitation. The spectrum recorded at 0.4 ps after the laser excitation indicates the generation of $4T^{\bullet+}$*-M-2T, whereas the positive peak was relatively broadened compared to the case of $4T^{\bullet+}$*-M. The kinetics were analyzed by global fitting assuming a double exponential function to the positive band (Figure 3-7b), providing a 440 nm-peaked species with a decay constant of 1.1×10^{12} s^{-1} (0.9 ps) and a 450 nm-peaked species with a decay constant of 2.5×10^{11} s^{-1} (4 ps). The former species is assigned to $4T^{\bullet+}$*-M-2T, whereas the latter species is assignable to 4T-M-$2T^{\bullet+}$ when considering the absorption of $2T^{\bullet+}$-M. These observations suggested an intramolecular HT process from $4T^{\bullet+}$* to 2T as indicated in eq 3-1.

$$4T^{\bullet+}\text{*-M-2T} \xrightarrow{k_{intraHT}} \text{4T-M-}2T^{\bullet+} \quad (3\text{-}1)$$

The intramolecular HT rate constant ($k_{intraHT}$) was calculated to be 6.3×10^{11} s^{-1} (1.6 ps) by taking the $D_1 \rightarrow D_0$ deactivation process into account. With further increase in the delay time, the positive band continuously decreased, whereas the negative band showed a recovery, suggesting a back HT (BHT) process from $2T^{\bullet+}$ to 4T as indicated in eq 3-2.

$$\text{4T-M-}2T^{\bullet+} \xrightarrow{k_{intraBHT}} 4T^{\bullet+}\text{-M-2T} \quad (3\text{-}2)$$

The intramolecular BHT rate constant ($k_{intraBHT}$) was 2.5×10^{11} s^{-1} (4 ps) as obtained from the decay of 4T-M-$2T^{\bullet+}$. The same intramolecular HT and BHT were also confirmed using an 1120 nm femtosecond laser (Figure 3-8).

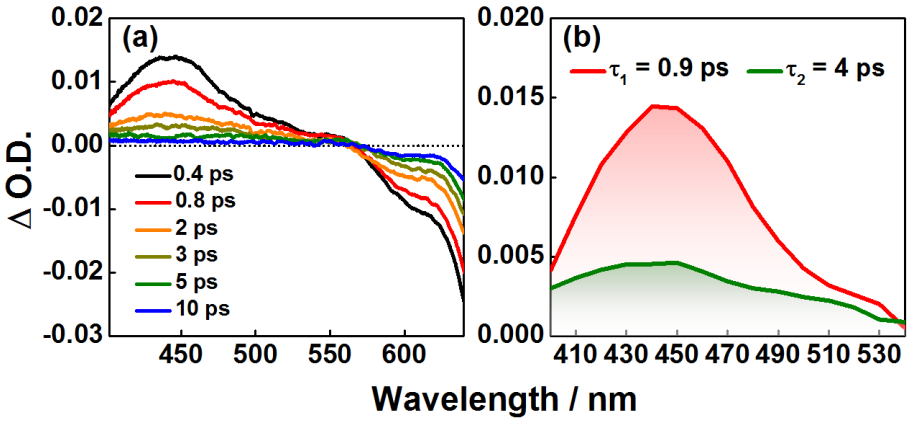

Figure 3-7. (a) Transient absorption spectra of 4T-M-2T (0.15 mM) in DCE with the presence of $FeCl_3$ (0.30 mM) during a 670 nm femtosecond laser excitation. (b) Decay-associated spectra

obtained by global fitting assuming a double exponential function to the positive band in Figure 3-7a.

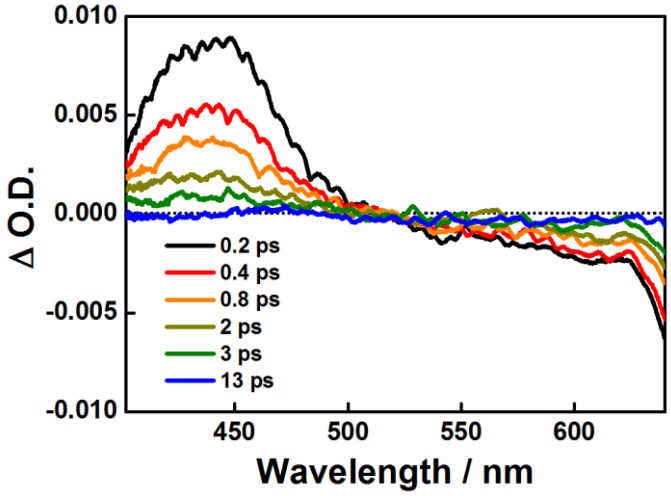

Figure 3-8. Transient absorption spectra of 4T-M-2T (0.15 mM) in DCE with the presence of $FeCl_3$ (0.30 mM) during an 1120 nm femtosecond laser excitation.

Figures 3-9a,b show the transient absorption spectra of $4T^{\bullet+}$-M-3T and the decay-associated spectra. The deactivation of $4T^{\bullet+}$*-M-3T and appearance of 4T-M-$3T^{\bullet+}$ indicated the intramolecular HT process from $4T^{\bullet+}$* to 3T (eq 3-3), whereas the decay of 4T-M-$3T^{\bullet+}$ indicated the BHT process (eq 3-4).

$$4T^{\bullet+}\text{*-M-3T} \xrightarrow{k_{\text{intraHT}}} \text{4T-M-}3T^{\bullet+} \qquad (3\text{-}3)$$

$$\text{4T-M-}3T^{\bullet+} \xrightarrow{k_{\text{intraBHT}}} 4T^{\bullet+}\text{-M-3T} \qquad (3\text{-}4)$$

The k_{intraHT} was calculated to be 1.3×10^{12} s^{-1} (0.8 ps) by taking into account the $D_1 \rightarrow D_0$ deactivation process. The k_{intraBHT} could not be obtained because of the overlapped absorption of $4T^{\bullet+}$* (D_0^{hot} state) and $3T^{\bullet+}$ (D_0 state). The same phenomena were also observed using the 1120 nm excitation (Figure 3-10). Thus, ultrafast intramolecular HT from excited radical cation within a timescale of 1−2 ps has been clearly confirmed upon $4T^{\bullet+}$ excitation of $4T^{\bullet+}$-M-2T and $4T^{\bullet+}$-M-3T.

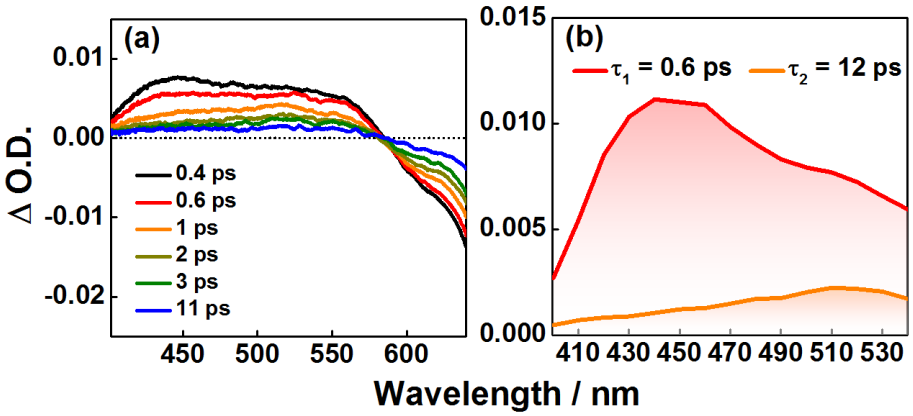

Figure 3-9. (a) Transient absorption spectra of 4T-M-3T (0.15 mM) in DCE with the presence of $FeCl_3$ (0.30 mM) during a 670 nm femtosecond laser excitation. (b) Decay-associated spectra obtained by global fitting assuming a double exponential function to the positive band in Figure 3-9a.

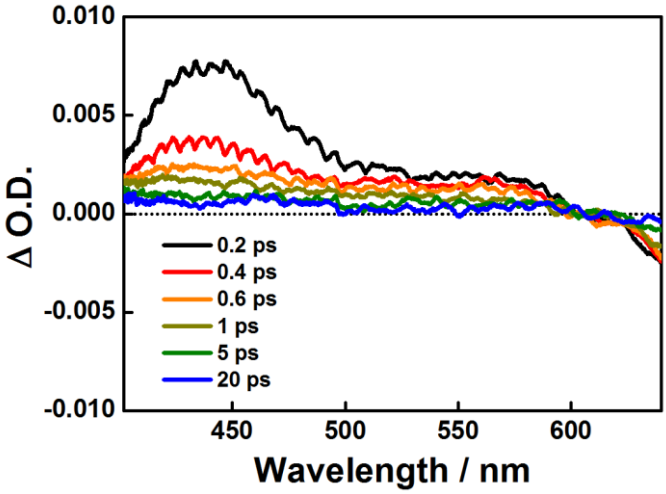

Figure 3-10. Transient absorption spectra of 4T-M-3T (0.15 mM) in DCE with the presence of $FeCl_3$ (0.30 mM) during an 1120 nm femtosecond laser excitation.

The rate constants and driving forces for the intramolecular HT processes from $4T^{\bullet+}$* are summarized in Table 3-3. The driving forces for HT and BHT ($-\Delta G_{intraHT}$ and $-\Delta G_{intraBHT}$) were calculated using eqs 3-5 and 3-6.

$$\Delta G_{intraHT} = -E(4T^{\bullet+}\text{-M}/4T\text{-M}) + E(A^{\bullet+}/A) - E_{D1}(4T^{\bullet+}\text{*-M}) \quad (3\text{-}5)$$

$$\Delta G_{intraBHT} = -E(A^{\bullet+}/A) + E(4T^{\bullet+}\text{-M}/4T\text{-M}) \quad (3\text{-}6)$$

where $E(4T^{\bullet+}\text{-M}/4T\text{-M})$, $E(A^{\bullet+}/A)$, and E_{D1} ($4T^{\bullet+}$*-M) are the oxidation potential of 4T-M, oxidation potential of the hole acceptor, and D_1 state energy of $4T^{\bullet+}$*-M, respectively. Due to the $D_1 \leftarrow D_0$ absorption band of $4T^{\bullet+}$-M at 1120 nm, 1.1 eV of E_{D1}($4T^{\bullet+}$*-M) was used in this study. As shown in Table 3-3, the $-\Delta G_{intraHT}$ values for $4T^{\bullet+}$*-M-2T and $4T^{\bullet+}$*-M-3T were calculated to be 0.8 and 1.0 eV, respectively. In these dyads, intramolecular HT processes were observed, and the $k_{intraHT}$ became larger with an increase in the $-\Delta G_{intraHT}$. Thus, it was suggested that exothermicity increases the intramolecular HT rate from excited radical cation as expected for the reactions in the Marcus normal region.[40-42]

Table 3-3. Rate Constants ($k_{intraHT}$ and $k_{intraBHT}$) and Driving Forces ($-\Delta G_{intraHT}$ and $-\Delta G_{intraBHT}$) for Intramolecular HT Processes from $4T^{\bullet+}$*.

	$k_{intraHT}$[a] (s^{-1})	$-\Delta G_{intraHT}$ (eV)	$k_{intraBHT}$[a] (s^{-1})	$-\Delta G_{intraBHT}$ (eV)
$4T^{\bullet+}$*-M-2T	6.3×10^{11}	0.8	2.5×10^{11}	0.3
$4T^{\bullet+}$*-M-3T	1.3×10^{12}	1.0	-[b]	0.1

[a]Estimation error: < 10%. [b]Not obtained.

Notably, the dyad systems in this study were designed to effectively capture the unique intramolecular HT between different *n*T moieties. To achieve this goal, the energy levels of the ground- and excited states of $nT^{\bullet+}$ have been considered. According to the current data and reported studies,[37,43] the oxidation potentials of 2T, 3T, 4T, 5T, and 6T are 1.3, 1.1, 1.0, 0.9, and 0.8 V vs. Ag/Ag^+, respectively, and the ΔE of D_1-D_0 transitions are 1.4, 1.3, 1.1, 0.9, and 0.8 eV, respectively (Scheme 3-9). Previously, we found that the intermolecular HT from $5T^{\bullet+}$* was relatively inefficient, probably because of its lower D_1 state energy level.[32] A similar consideration can also be applied to the case of $6T^{\bullet+}$*. Additionally, the larger dyad system (e.g., 5T-M-4T or 6T-M-5T) usually exhibits a poor solubility in organic solvents, causing difficulty in synthesis and spectroscopic measurements. In the cases of $2T^{\bullet+}$* and $3T^{\bullet+}$*, the candidate *n*T as the hole acceptors are almost nonexistent although the driving forces may be favorable. Moreover, the producing of $2T^{\bullet+}$* and $3T^{\bullet+}$* is a ticklish problem due to the instability of $2T^{\bullet+}$

and $3T^{\bullet+}$, as described in the chemical oxidation part. On the basis of all these reasons, here we prepared $4T^{\bullet+}$*-M-2T and $4T^{\bullet+}$*-M-3T as the key targets.

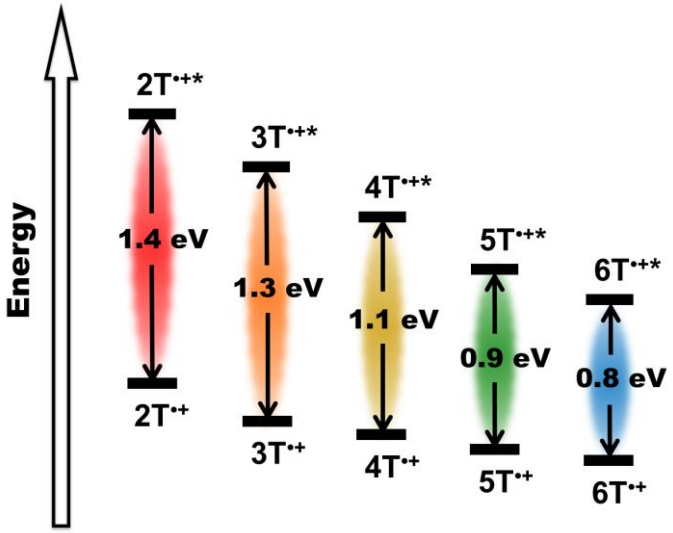

Scheme 3-9. Energetic scheme for ground- and excited states of different nT$^{\bullet+}$.

Generally, nT and their singlet/triplet excited species were applied as the hole acceptors during the intramolecular charge separation and recombination.[44-46] However, by adding an additional excitation energy to nT$^{\bullet+}$, we have shown here that nT$^{\bullet+}$* can be treated as the hole donors to initiate the intramolecular oxidation that cannot be expected in their neutral states. Furthermore, the present HT processes are closely related to the charged-carrier migration phenomena observed in p-type semiconductor materials, since nT can be regarded as the simplest units of conductive thiophene-based materials. The photoinduced HT and rate in $4T^{\bullet+}$-M-2T and $4T^{\bullet+}$-M-3T correspond to the photocarrier (i.e., polaron) migration and mobility, respectively, in the charged polythiophenes upon irradiation.[47-49] According to the current results, the HT rate (1.6 or 0.8 ps) is faster than the deactivation rate (2.1 ps), suggesting a prompt and effective polaron migration immediately after the production of nT$^{\bullet+}$*. In addition, the subsequent BHT processes shown here (4T-M-2T$^{\bullet+}$ → 4T$^{\bullet+}$-M-2T and 4T-M-3T$^{\bullet+}$ → 4T$^{\bullet+}$-M-3T) also gave a direct observation for the HT between the ground-state nTs in the clear structures. This indicates the possibility of further charge transport (e.g., interchain HT) between the nT segments in

polythiophenes,[50,51] which are far more complex than dyad molecules. The successive HT dynamics are shown in Scheme 3-10.

Interestingly, the hole mobility (μ) from $4T^{\bullet+}$* in this study can be estimated to be ~0.5 $cm^2V^{-1}s^{-1}$ using the equation, $\mu = eD/kT$, where e is the elementary charge, D is the time-dependent diffusion coefficient ($D = d^2/2t$, d is the center-to-center distance between the hole donor and acceptor; t is the k_{HT}^{-1}), k is the Boltzmann constant, and T is the temperature.[52] On the other hand, the μ from $2T^{\bullet+}$ or $3T^{\bullet+}$ was evaluated to be a lower value of ~0.1 $cm^2V^{-1}s^{-1}$, which agrees with the reported cases for highly regioregulated thiophene materials in the ground states.[50,53] Thus, this study has provided a completely different viewpoint to understand the HT behaviors of oligo- and polythiophenes in various organic molecular devices and clearly exhibited the importance of new pathways from $nT^{\bullet+}$*.

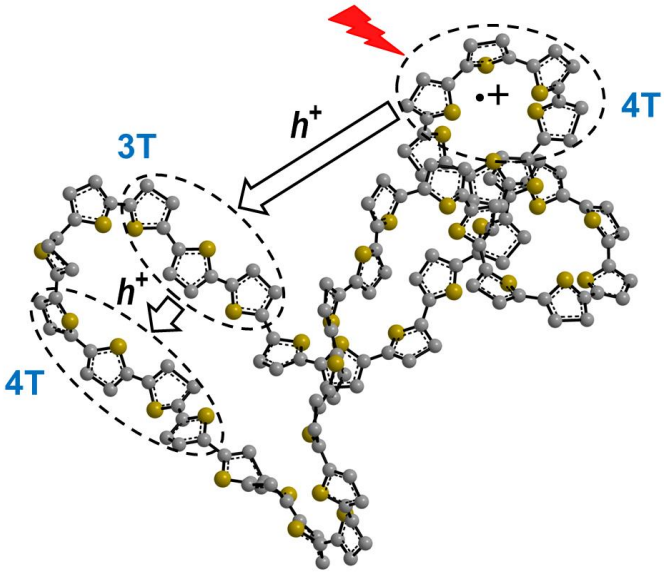

Scheme 3-10. Photocarriers migrated from $nT^{\bullet+}$* in polythiophenes.

Conclusions

The intramolecular HT from excited radical cation was investigated for the first time using a new series of mesitylene-linked nT. The use of mesitylene as a spacer realized a minimized π-conjugation with nT and an increased stability of $nT^{\bullet+}$. An analysis of the transient absorption

spectra of $4T^{\bullet+}$-M upon 670 nm excitation showed the existence of two species as the D_1 and D_0^{hot} states. Photo-accelerated intramolecular HT with the subsequent BHT processes were confirmed in $4T^{\bullet+}$*-M-2T and $4T^{\bullet+}$*-M-3T. This was the first capture of such successive HT by applying femtosecond laser flash photolysis to the charged *n*T assemblies. The results shown here have provided valuable insights into the unique characteristics of $nT^{\bullet+}$* as not only the hole donors, but also the initiators for rapid photocarrier generation in related p-type organic semiconductors.

References

(1) Mazzeo, M.; Pisignano, D.; Favaretto, L.; Barbarella, G.; Cingolani, R.; Gigli, G. *Synthetic Met.* **2003**, *139*, 671.

(2) Kunugi, Y.; Takimiya, K.; Negishi, N.; Otsubo, T.; Aso, Y. *J. Mater. Chem.* **2004**, *14*, 2840.

(3) Zen, A.; Pflaum, J.; Hirschmann, S.; Zhuang, W.; Jaiser, F.; Asawapirom, U.; Rabe, J. P.; Scherf, U.; Neher, D. *Adv. Funct. Mater.* **2004**, *14*, 757.

(4) Perepichka, I. F.; Perepichka, D. F.; Meng, H.; Wudl, F. *Adv. Mater.* **2005**, *17*, 2281.

(5) Hou, J.; Chen, H.; Zhang, S.; Li, G.; Yang, Y. *J. Am. Chem. Soc.* **2008**, *130*, 16144.

(6) Hains, A. W.; Ramanan, C.; Irwin, M. D.; Liu, J.; Wasielewski, M. R.; Marks, T. J. *ACS Appl. Mater. Interfaces* **2010**, *2*, 175.

(7) van Haare, J. A. E. H.; Havinga, E. E.; van Dongen, J. L. J.; Janssen, R. A. J.; Cornil, J.; Brédas, J. *Chem. Eur. J.* **1998**, *4*, 1509.

(8) Guo, J.; Ohkita, H.; Benten, H.; Ito, S. *J. Am. Chem. Soc.* **2009**, *131*, 16869.

(9) Xu, B. Q.; Li, X. L.; Xiao, X. Y.; Sakaguchi, H.; Tao, N. J. *Nano Lett.* **2005**, *5*, 1491.

(10) Sugimoto, T.; Habuchi, S.; Ogino, K.; Vacha, M. *J. Phys. Chem. B* **2009**, *113*, 12220.

(11) Repp, J.; Liljeroth, P.; Meyer, G. *Nature Phys.* **2010**, *6*, 975.

(12) Honmou, Y.; Hirata, S.; Komiyama, H.; Hiyoshi, J.; Kawauchi, S.; Iyoda, T.; Vacha, M. *Nat. Commun.* **2014**, *5*, 1.

(13) Grozema, F. C.; van Duijnen, P. T.; Berlin, Y. A.; Ratner, M. A.; Siebbeles, L. D. A. *J. Phys. Chem. B* **2002**, *106*, 7791.

(14) Aziz, E. F.; Vollmer, A.; Eisebitt, S.; Eberhardt, W.; Pingel, P.; Neher, D.; Koch, N. *Adv. Mater.* **2007**, *19*, 3257.

(15) Smith, C. E.; Odoh, S. O.; Ghosh, S.; Gagliardi, L.; Cramer, C. J.; Frisbie, C. D. *J. Am. Chem. Soc.* **2015**, *137*, 15732.

(16) Mena-Osteritz, E.; Meyer, A.; Langeveld-Voss, B. M. W.; Janssen, R. A. J.; Meijer, E. W.; Bäuerle, P. *Angew. Chem.* **2000**, *112*, 2791.

(17) Adachi, T.; Brazard, J.; Ono, R. J.; Hanson, B.; Traub, M. C.; Wu, Z.; Li, Z.; Bolinger, J. C.; Ganesan, V.; Bielawski, C. W.; Vanden Bout D. A.; Barbara P. F. *J. Phys. Chem. Lett.* **2011**, *2*, 1400.

(18) Ghosh, I.; Ghosh, T.; Bardagi, J. I.; König, B. *Science* **2014**, *346*, 725.

(19) Fujitsuka, M.; Kim, S. S.; Lu, C.; Tojo, S.; Majima, T. *J. Phys. Chem. B* **2015**, *119*, 7275.

(20) Fujitsuka, M.; Ohsaka, T.; Majima, T. *Phys. Chem. Chem. Phys.* **2015**, *17*, 31030.

(21) Zeng, L.; Liu, T.; He, C.; Shi, D.; Zhang, F.; Duan, C. *J. Am. Chem. Soc.* **2016**, *138*, 3958.

(22) Lu, C.; Fujitsuka, M.; Sugimoto, A.; Majima, T. *J. Phys. Chem. C* **2016**, *120*, 12734.

(23) Ishida, A.; Fukui, M.; Ogawa, H.; Tojo, S.; Majima, T.; Takamuku, S. *J. Phys. Chem.* **1995**, *99*, 10808.

(24) Ichinose, N.; Tanaka, T.; Kawanishi, S.; Majima, T. *Chem. Phys. Lett.* **2000**, *326*, 293.

(25) Ichinose, N.; Majima, T. *Chem. Phys. Lett.* **2000**, *322*, 15.

(26) Häupl, T.; Lomoth, R.; Hammarström, L. *J. Phys. Chem. A* **2003**, *107*, 435.

(27) Okhrimenko, A. N.; Gusev, A. V.; Rodgers, M. A. J. *J. Phys. Chem. A* **2005**, *109*, 7653.

(28) Cai, X.; Sakamoto, M.; Fujitsuka, M.; Majima, T. *Chem. Phys. Lett.* **2006**, *432*, 436.

(29) Pagès, S.; Lang, B.; Vauthey, E. *J. Phys. Chem. A* **2006**, *110*, 7547.

(30) Sánchez-Carrera, R. S.; Coropceanu, V.; Da Silva Filho, D. A.; Friedlein, R.; Osikowicz, W.; Murdey, R.; Suess, C.; Salaneck, W. R.; Brédas, J. *J. Phys. Chem. B* **2006**, *110*, 18904.

(31) Amarie, S.; Förster, U.; Gildenhoff, N.; Dreuw, A.; Wachtveitl, J. *Chem. Phys.* **2010**, *373*, 8.

(32) Samori, S.; Fujitsuka, M.; Majima, T. *J. Phys. Chem. A* **2008**, *112*, 11312.

(33) Tamao, K.; Kodama, S.; Nakajima, I.; Kumada, M.; Minato, A.; Suzuki, K. *Tetrahedron* **1982**, *38*, 3347.

(34) Fujitsuka, M.; Cho, D. W.; Tojo, S.; Inoue, A.; Shiragami, T.; Yasuda, M.; Majima, T. *J. Phys. Chem. A* **2007**, *111*, 10574.

(35) Frisch, M. J.; Trucks, G. W.; Schlegel, H. B.; Scuseria, G. E.; Robb, M. A.; Cheeseman, J. R.; Scalmani, G.; Barone, V.; Mennucci, B.; Petersson, G. A.; Nakatsuji, H.; Caricato, M.; Li, X.; Hratchian, H. P.; Izmaylov, A. F.; Bloino, J.; Zheng, G.; Sonnenberg, J. L.; Hada, M.; Ehara, M.;

Toyota, K.; Fukuda, R.; Hasegawa, J.; Ishida, M.; Nakajima, T.; Honda, Y.; Kitao, O.; Nakai, H.; Vreven, T.; Montgomery, J. A., Jr.; Peralta, J. E.; Ogliaro, F.; Bearpark, M.; Heyd, J. J.; Brothers, E.; Kudin, K. N.; Staroverov, V. N.; Kobayashi, R.; Normand, J.; Raghavachari, K.; Rendell, A.; Burant, J. C.; Iyengar, S. S.; Tomasi, J.; Cossi, M.; Rega, N.; Millam, N. J.; Klene, M.; Knox, J. E.; Cross, J. B.; Bakken, V.; Adamo, C.; Jaramillo, J.; Gomperts, R.; Stratmann, R. E.; Yazyev, O.; Austin, A. J.; Cammi, R.; Pomelli, C.; Ochterski, J. W.; Martin, R. L.; Morokuma, K.; Zakrzewski, V. G.; Voth, G. A.; Salvador, P.; Dannenberg, J. J.; Dapprich, S.; Daniels, A. D.; Farkas, Ö.; Foresman, J. B.; Ortiz, J. V.; Cioslowski, J.; Fox, D. J. *Gaussian 09*, Revision C.01; Gaussian, Inc.: Wallingford, CT, 2009.

(36) Sato, T.; Hori, K.; Fujitsuka, M.; Watanabe, A.; Ito, O.; Tanaka, K. *J. Chem. Soc., Faraday Trans.* **1998**, *94*, 2355.

(37) Fichou, D.; Horowitz, G.; Xu, B.; Garnier, F. *Synth. Met.* **1990**, *39*, 243.

(38) Barik, S.; Skene, W. G. *Polym. Chem.* **2011**, *2*, 1091.

(39) Garcia, P.; Pernaut, J. M.; Hapiot, P.; Wintgens, V.; Valat, P.; Garnier, F.; Delabouglise, D. *J. Phys. Chem.* **1993**, *97*, 513.

(40) Marcus, R. A. *Annu. Rev. Phys. Chem.* **1964**, *15*, 144.

(41) Marcus, R. A.; Sutin, N. *Biochim. Biophys. Acta* **1985**, *811*, 265.

(42) Marcus, R. A. *Angew. Chem. Int. Ed. Eng.* **1993**, *32*, 1111.

(43) Wei, Y.; Chan, C. C.; Tian, J.; Jang, G. W.; Hsueh, K. F. *Chem. Mater.* **1991**, *3*, 888.

(44) Fujitsuka, M.; Masuhara, A.; Kasai, H.; Oikawa, H.; Nakanishi, H.; Ito, O.; Yamashiro, T.; Aso, Y.; Otsubo, T. *J. Phys. Chem. B* **2001**, *105*, 9930.

(45) Oseki, Y.; Fujitsuka, M.; Cho, D. W.; Sugimoto, A.; Tojo, S.; Majima, T. *J. Phys. Chem. B* **2005**, *109*, 19257.

(46) Fujitsuka, M.; Nakatani, T.; Sakamoto, M.; Sugimoto, A.; Majima, T. *J. Phys. Chem. A* **2010**, *114*, 10789.

(47) Shoaee, S.; An, Z.; Zhang, X.; Barlow, S.; Marder, S. R.; Duffy, W.; Heeney, M.; McCulloch, I.; Durrant, J. R. *Chem. Commun.* **2009**, 5445.

(48) Hwang, I.; Moses, D.; Heeger, A. J. *J. Phys. Chem. C* **2008**, *112*, 4350.

(49) Guo, J.; Ohkita, H.; Benten, H.; Ito, S. *J. Am. Chem. Soc.* **2010**, *132*, 6154.

(50) Sirringhaus, H.; Brown, P. J.; Friend, R. H.; Nielsen, M. M.; Bechgaard, K.; Langeveld-Voss, B.; Spiering, A.; Janssen, R. A.; Meijer, E. W.; Herwig, P. *Nature* **1999**, *401*, 685.

(51) Brédas, J.; Beljonne, D.; Coropceanu, V.; Cornil, J. *Chem. Rev.* **2004**, *104*, 4971.

(52) Grozema, F. C.; Siebbeles, L. D.; Berlin, Y. A.; Ratner, M. A. *ChemPhysChem* **2002**, *3*, 536.

(53) Videlot-Ackermann, C.; Ackermann, J.; Brisset, H.; Kawamura, K.; Yoshimoto, N.; Raynal, P.; El Kassmi, A.; Fages, F. *J. Am. Chem. Soc.* **2005**, *127*, 16346.

General Conclusion

Throughout this dissertation, the ground- and excited-state properties of radical ions were systematically examined by intermolecular charge recombination and intramolecular electron transfer (ET) (or hole transfer (HT)) processes using nanosecond pulse radiolysis and femtosecond laser flash photolysis, respectively.

In Chapter 1, three bis(diarylamino)dihydro-indenoindenes (R-DI) were investigated by nanosecond pulse radiolysis to observe the absorption spectra of their corresponding radical cations ($R\text{-}DI^{\bullet+}$) and anions ($R\text{-}DI^{\bullet-}$). It was suggested that the positive charge is mainly localized on the triphenylamine (TPA) moiety of $R\text{-}DI^{\bullet+}$, whereas the negative charge is localized on the *trans*-stilbene moiety of $R\text{-}DI^{\bullet-}$. All R-DI showed emission with nanosecond lifetimes during the pulse radiolysis in benzene. The observed emission was considered to be derived from the direct singlet excited state (^{1}R-DI*) generation by the charge recombination between the ground-state $R\text{-}DI^{\bullet+}$ and $R\text{-}DI^{\bullet-}$.

In Chapter 2-1, several reduced dyad molecules were investigated by femtosecond laser flash photolysis to observe the intramolecular ET processes from excited perylenediimide radical anion ($PDI^{\bullet-}$*) for the first time. It was found that efficient intramolecular ET occurred in $PDI^{\bullet-}$*-pyromellitimide (PI) and $PDI^{\bullet-}$*-naphthalenediimide (NDI) because of the sufficient driving forces. In particular, $PDI^{\bullet-}$*-PDI and $PDI^{\bullet-}$*-$PDI^{\bullet-}$ exhibited quite different ET pathways. By applying the Marcus theory to the dyad systems of $NDI^{\bullet-}$* and $PDI^{\bullet-}$*, the ET rate constant (k_{ET}) difference could be reasonably explained.

In Chapter 2-2, the ET in densely charged aromatic diimides (ADIs) upon excitation was systematically investigated by femtosecond laser flash photolysis using a series of reduced dyads: $NDI^{\bullet-}$-*m*-$NDI^{\bullet-}$, $NDI^{\bullet-}$-*p*-$NDI^{\bullet-}$, $PDI^{\bullet-}$-*m*-$PDI^{\bullet-}$, and $NDI^{\bullet-}$-*m*-$PDI^{\bullet-}$ (*m* and *p* indicate the substitution positions). Different k_{ET} were observed for the generation of NDI and NDI^{2-} in $NDI^{\bullet-}$*-*m*-$NDI^{\bullet-}$ and $NDI^{\bullet-}$*-*p*-$NDI^{\bullet-}$. Interestingly, the duality of the excited radical anion, which could act as both an electron donor and acceptor, was clearly revealed upon excitation of

the $NDI^{\bullet-}$ and $PDI^{\bullet-}$ moieties in $NDI^{\bullet-}$-$PDI^{\bullet-}$, respectively. By applying the Marcus theory, the relationship between the k_{ET} and driving forces in $ADI^{\bullet-}$*-$ADI'^{\bullet-}$ could be reasonably explained.

In Chapter 3, the intramolecular HT from excited radical cation was investigated for the first time using a new series of mesitylene-linked oligothiophenes (*n*T, *n* is the number of thiophene units). The use of mesitylene as a spacer realized a minimized π-conjugation with *n*T and an increased stability of $nT^{\bullet+}$. An analysis of the transient absorption spectra of $4T^{\bullet+}$-M upon 670 nm excitation showed the existence of two species as the D_1 and D_0^{hot} states. Photo-accelerated intramolecular HT with the subsequent back HT processes were confirmed in $4T^{\bullet+}$*-M-2T and $4T^{\bullet+}$*-M-3T. This was the first capture of such successive HT by applying femtosecond laser flash photolysis to the charged *n*T assemblies.

To conclude, the results shown in Chapter 1 indicated the important functions of the ground-state radical ions in emission mechanism of R-DI as new candidates for organic light-emitting diodes (OLEDs); the results shown in Chapter 2 provided valuable insights into the unique characteristics of $PDI^{\bullet-}$* and $ADI^{\bullet-}$*-$ADI'^{\bullet-}$ as the effective initiators for photocarrier (polaron and bipolaron) generation in related n-type semiconductor materials; the results shown in Chapter 3 gave a perspective on the distinctive nature of $nT^{\bullet+}$* as not only the hole donors, but also the initiators for rapid photocarrier generation in related p-type organic semiconductors. Thus, this dissertation unambiguously revealed the novel aspects (e.g., charge transport behaviors) of both n-type and p-type organic materials relating to the crucial roles of ground- and excited-state radical anions and cations.

List of Publications

1. Intermolecular and Intramolecular Electron Transfer Processes from Excited Naphthalene Diimide Radical Anions
   Mamoru Fujitsuka, Sung Sik Kim, Chao Lu, Sachiko Tojo, and Tetsuro Majima.
   J. Phys. Chem. B **2015**, *119* (24), 7275-7282.

2. Emission from Charge Recombination during the Pulse Radiolysis of Bis(diarylamino)dihydro-indenoindene Derivatives
   Chao Lu, Mamoru Fujitsuka, Sachiko Tojo, Wei-Jyun Wang, Yi Wei, and Tetsuro Majima.
   J. Phys. Chem. C **2015**, *119* (31), 17818-17824.

3. Unprecedented Intramolecular Electron Transfer from Excited Perylenediimide Radical Anion
   Chao Lu, Mamoru Fujitsuka, Akira Sugimoto, and Tetsuro Majima.
   J. Phys. Chem. C **2016**, *120* (23), 12734-12741.

4. Photoaccelerated Hole Transfer in Oligothiophene Assemblies
   Chao Lu, Mamoru Fujitsuka, and Tetsuro Majima.
   J. Phys. Chem. C, DOI: 10.1021/acs.jpcc.6b07904.

5. Dual Character of Excited Radical Anions in Aromatic Diimide Bis(Radical Anion)s: Donor or Acceptor?
   Chao Lu, Mamoru Fujitsuka, Akira Sugimoto, and Tetsuro Majima.
   Submitted.

Supplementary List of Publications

6. Properties of Triplet-Excited [*n*]Cycloparaphenylenes (*n* = 8–12): Excitation Energies

Lower than Those of Linear Oligomers and Polymers

Mamoru Fujitsuka, Chao Lu, Takahiro Iwamoto, Eiichi Kayahara, Shigeru Yamago, and Tetsuro Majima.

J. Phys. Chem. A **2014**, *118* (25), 4527-4532.

7. Multistep Electron Transfer Systems Containing [2.2]- or [3.3]Paracyclophane

Mamoru Fujitsuka, Takaaki Miyazaki, Chao Lu, Teruo Shinmyozu, and Tetsuro Majima.

J. Phys. Chem. A **2016**, *120* (8), 1184-1189.

Acknowledgements

The author would like to express the deepest appreciation to Professor Tetsuro Majima for his thoughtful supervision and valuable suggestions throughout the doctoral course.

The author wishes to express his sincere gratitude to Associate Professor Mamoru Fujitsuka for his fruitful advices and detailed discussion. The author is deeply grateful to Assistant Professor Sachiko Tojo and Specially-Appointed Professor Akira Sugimoto for their kindly support on his experiments.

The author would like to appreciate the collaborators: Professor Sung Sik Kim in Chonbuk National University, Jeonju, Korea; Professor Yi Wei and his student Wei-Jyun Wang in Tamkang University, New Taipei City, Taiwan. The author also thanks the members of Research Laboratory for Quantum Beam Science and Comprehensive Analysis Center, Institute of Scientific and Industrial Research (ISIR), Osaka University, for running the related instruments.

The author expresses his sincere appreciation to Professor Yoshio Aso and Professor Toshiyuki Kida, and all the professors of Molecular Chemistry Course, Department of Applied Chemistry, Graduate School of Engineering, Osaka University for their productive comments and suggestions on this dissertation.

The author sincerely thanks Associate Professor Kiyohiko Kawai, Assistant Professor Takashi Tachikawa (currently, Associate Professor in Kobe University, Kobe, Japan), Assistant Professor Yasuko Osakada, Specially-Appointed Professor Mikiji Miyata, Specially-Appointed Assistant Professor Jungkweon Choi (currently, Research Fellow in Institute for Basic Science, Daejeon, Korea), and Specially-Appointed Assistant Professor Sooyeon Kim for their helpful suggestions on his research. The author thanks Ms. Sanae Tominaga and other administration staff for their kindly helps on document preparation.

The author hopes to thank the members of Professor Majima's research group, including Dr. Shicong Cui, Dr. Zhaoke Zheng, Dr. Zaizhu Lou, Dr. Mingshan Zhu, Dr. Shaoqing Song, Dr. Peng Zhang, Dr. Shih-Hsun Lin, Dr. Zhichao Sun, Mr. Atsushi Tanaka, Mr. Rui Sun, Mr. Weikang Wang, Mr. Ossama A. Elbanna, Ms. Xiaoyan Cai, Mr. Xiaowei Shi, Mr. Peerathat Pinpithak, Mr. Daming Ruan, Mr. Takeshi Koshimo, Mr. Tatsuya Ohsaka, Mr. Shunsuke Ano,

Mr. Kenshi Nakao, Mr. Kota Nomura, Ms. Ayaka Kuroda, Mr. Yuma Ichinose, Mr. Yoji Yamamoto, Mr. Yang Zhou, Ms. Jie Xu, Ms. Yue Wang, Mr. Bo Zhuang, and Ms. Lei Xu.

The author acknowledges the scholarship program from the China Scholarship Council (CSC) and the financial support from the Japanese Ministry of Education, Culture, Sports, Science, and Technology (MEXT). The author also appreciates the teachers and classmates in the Preparatory School for Chinese Students to Japan (PSCSJ), Changchun, China.

Finally, the author is truly grateful to his family members for their continuing encouragement and support during the doctoral course, which enabled him to complete this dissertation.

Chao Lu

2017